

# A Comparative Study of Experimental Joint Identification Techniques for Bolted Connections

Eine Vergleichsstudie von experimentellen Identifikationsmethoden für geschraubte Verbindungen

Scientific work for obtaining the academic degree  
Master of Science (M.Sc.)

at the TUM School of Engineering and Design of the Technical University of Munich

**Supervisor** Prof. dr.ir. Daniel J. Rixen  
Chair of Applied Mechanics

**Advisor** Francesco Trainotti, M. Sc.  
Chair of Applied Mechanics

**Submitted by** Sandra Kühbacher, B. Sc.

**Submitted on** May 19, 2022 in Garching



## Abstract

Within this thesis, an experimental joint identification using the linear approach frequency based substructuring is implemented. It comprises decoupling the joint with inverse substructuring and parameterizing its stiffness by a constant. The damping is neglected since it is lower than the noise floor of the sensors and cannot be identified. The approach is assessed by comparing the subsequently coupled result to the original measurements. The test structure was originally developed to study non-linear joint identification methods and is not well suited for the application of substructuring. Using this particular test structure shows the limitations of inverse substructuring. It is therefore not possible to confirm the correctness of the isolation and parameterization of the joint. In addition, substructuring is compared to a non-linear joint ID technique using the Hilbert transform. The comparison shows how large the error can be that is caused by the linearization of the problem. Thereby, it is of interest how much the test system is influenced by non-linearities. To detect existing non-linearities, the Zeroed Early-Time Fast Fourier Transform method proposed by Allen and Mayes [1] can be used in combination with backward extrapolation. A basic implementation of this method is implemented in this work.

## Zusammenfassung

Im Rahmen dieser Arbeit wird eine experimentelle Analyse von Gelenkverbindungen mit dem linearen Ansatz *frequency based substructuring* durchgeführt. Die Analyse umfasst die Entkopplung des Gelenks mit *inverse substructuring* und die Parametrisierung der Gelenksteifigkeit durch eine Konstante. Die Dämpfung wird vernachlässigt, da sie unter dem Grundrauschen der Sensoren liegt und nicht identifiziert werden kann. Der Ansatz wird bewertet, indem das anschließend gekoppelte Ergebnis mit den originalen Messungen verglichen wird. Die Teststruktur wurde ursprünglich entwickelt, um nichtlineare Methoden zur Identifizierung von Gelenken zu untersuchen, und ist für die Anwendung von *substructuring* nicht gut geeignet. Die Verwendung der Teststruktur zeigt die Grenzen der *inverse substructuring* auf, so dass es nicht möglich ist, die Richtigkeit der Isolation und Parametrisierung des Gelenks zu bestätigen. Darüber hinaus werden die Ergebnisse von *substructuring* mit den Ergebnissen einer nichtlinearen Identifikation von Gelenken mithilfe der Hilbert-Transformation verglichen. Der Vergleich zeigt, wie groß der Fehler ist, der bei der Linearisierung des Problems gemacht werden kann. Dabei ist es von Interesse, wie stark das Testsystem durch Nichtlinearitäten beeinflusst wird. Um vorhandene Nichtlinearitäten zu erkennen, kann die von Allen and Mayes [1] vorgeschlagene *Zeroed Early-Time Fast Fourier Transform* Methode in Kombination mit einer Rückwärtsextrapolation verwendet werden. Es wird eine grundlegende Implementierung dieser Methode in der vorliegenden Arbeit umgesetzt.



# Contents

<b>1</b>	<b>Introduction</b>	<b>3</b>
<b>2</b>	<b>Theoretical Background</b>	<b>5</b>
2.1	Hilbert Transform Algorithm . . . . .	5
2.2	Frequency Based Dynamic Substructuring . . . . .	7
2.2.1	Interface Conditions . . . . .	8
2.2.2	Coupling in the Frequency Domain . . . . .	9
2.2.3	Decoupling in the Frequency Domain . . . . .	11
2.2.4	Virtual Point Transformation . . . . .	13
2.3	Zeroed Early-Time Fast Fourier Transform . . . . .	14
2.3.1	Backwards Extrapolation for Non-Linearity Detection . . . . .	15
<b>3</b>	<b>Methodology and Implementation of Joint Identification Strategies</b>	<b>17</b>
3.1	Non-Linear Joint Identification with Hilbert Transform . . . . .	17
3.2	Linear Joint Identification with Frequency Based Substructuring . . . . .	18
3.2.1	Interface Modeling . . . . .	18
3.2.2	Joint Isolation and Parameterization with Inverse Substructuring . . . . .	19
3.2.3	Reconstruction with the Identified Joint . . . . .	20
3.3	Non-Linearity Elimination with Zeroing and Back-Extrapolation . . . . .	20
3.3.1	Modal Identification for Single DoF Systems . . . . .	21
3.4	Design of Experiments . . . . .	22
3.4.1	Structural Design . . . . .	23
3.4.2	Measurement Campaign . . . . .	25
<b>4</b>	<b>Application and Results</b>	<b>29</b>
4.1	Calculation of Frequency and Damping Curves . . . . .	29
4.2	Investigation of Frequency Based Substructuring . . . . .	34
4.2.1	Quality of the Measurements for Frequency Based Substructuring . . . . .	35
4.2.2	Isolation and Parameterization of the Joint . . . . .	39
4.2.3	Verification with Big Sensors . . . . .	44
4.3	Investigation of the Coupling Results . . . . .	45
4.4	Comparison of Non-Linear and Linear Joint Identification . . . . .	53
4.4.1	Review of the Inverse Substructuring Assumptions . . . . .	58
4.5	Application of Zeroing and Back-Extrapolation . . . . .	60
4.5.1	Sensitivity and Limitations . . . . .	64
<b>5</b>	<b>Conclusion and Outlook</b>	<b>67</b>
	<b>Bibliography</b>	<b>69</b>



## Abbreviations

BE	Backwards-extrapolation
BEND	Backwards extrapolation for non-linearity detection
DOE	Design of experiments
DoF(s)	Degree(s) of Freedom
DS	Dynamic substructuring
FFT	Fast Fourier transform
FBS	Frequency based substructuring
FRF(s)	Frequency response function(s)
HT	Hilbert Transform
ID	Identification
IDM(s)	Interface displacement mode(s)
LM-FBS	Lagrange multiplier - frequency based substructuring
VP	Virtual point
VPT	Virtual point transformation
ZEFFT(s)	Zeroed Early-Time Fast Fourier Transform(s)





# Chapter 1

## Introduction

Real mechanical structures consist of multiple parts assembled by jointed connections. These joints add stiffness as well as damping to the system and may increase the presence of non-linearities in the dynamical behavior of the system [2]. Existing analytical methods to predict the dynamics of the joint and therefore its contribution to the overall system dynamics are not accurate enough. Hence, various experimental methods have been developed for this purpose [16]. In general, the joint identification (ID) methods can be split into methods that build on the linearized model of the test structure and methods using the non-linear model itself. However, there is a lack of examining both, linear and non-linear joint ID methods, to evaluate, e.g., the error that is caused by the linearization.

In this thesis, the linear joint ID method dynamic substructuring (DS) is compared against a modal-based non-linear ID technique based on Hilbert transform (HT).

DS is a collection of powerful approaches to analyze and parameterize dynamic systems component-wise with great advantages. DS allows to evaluate large and complex structures on a substructure-level and characterize the dynamic properties of joints connecting multiple components [9, 18]. Within this thesis, the joint's dynamics are approximated using a constant value for the stiffness. The damping of the joint is neglected since the noise floor is higher than the damping.

A goal of this work is to evaluate the reliability and robustness of substructuring ID for bolted connections including the joint isolation and parameterization. In addition, the sensitivity to varying contact parameters is assessed. The test structure (section 3.4) used in this thesis was originally developed to study non-linear joint ID methods. Over the course of the experiments it turned out that the test structure is not well suited for the application of DS. Using the structure, the particular challenge is to find out to what extent DS can be applied and where its limits are. It is analyzed how far the linearization for substructuring influences the joint ID results by also using the non-linear ID technique HT.

When comparing linear and non-linear ID techniques, it is interesting to know how much the system and certain frequencies are affected by non-linearities. In order to detect and assess the non-linearity in the test system, the method Zeroed Early-Time Fast Fourier Transform (ZEFFT) combined with a backwards-extrapolation (BE) proposed by Allen and Mayes [1] is used. This technique allows to recreate the system without non-linearities so that only the linear portion of the dynamics of the system remain. However, due to problems in the application of the method, the analysis of the non-linearities over the entire system cannot be conducted in this work. A basic implementation of the methodology is nonetheless shown in this thesis.

The following section (chapter 2) introduces the theory of substructuring in the frequency domain, as well as the HT and ZEFFT with BE. In chapter 3 the implemented approaches for the linear and non-linear joint ID as well as the BE of zeroed-early time fast Fourier transforms

are described. This section also contains a detailed description of the design of experiments (DOE). Chapter 4 includes the evaluation and comparison of the implemented approaches using experimental data. Chapter 5 will give a proposal on how to continue research on the basis of the findings obtained during this thesis.

## Chapter 2

### Theoretical Background

#### 2.1 Hilbert Transform Algorithm

The HT algorithm is a widely used and reliable method to identify non-linear systems proposed by Feldman [5]. With the combination of the HT and curve fitting, mode-based amplitude dependent frequency and damping curves can be calculated that describe the effect of the joint non-linearity on the dynamics of the assembled system. However, its use is limited to mono-modal (one degree of freedom) systems and modal interactions cannot be identified [8]. The approach is described in the following according to the suggestion by Sracic, Allen, and Sumali [14].

Let us consider the free response of a weakly non-linear system (assuming negligible modal interactions and, e.g., smooth non-linearities that vary slowly in time) with  $N$  eigenmodes:

$$y(t) = \sum_{r=1}^N A_r(t) \cos(\omega_{d,r}t + \varphi_{0,r}) \quad (2.1)$$

where  $A_r(t)$  is the time varying amplitude of the  $r^{th}$  eigenmode,  $\omega_{d,r}$  the  $r^{th}$  damped natural frequency, and  $\varphi_{0,r}$  the  $r^{th}$  phase variable. Since the HT is limited to mono-modal systems, the following explanation refers to the response of a single mode  $y_r(t)$ . This requires that the assumption of uncoupled modes is valid for the considered system. To gain a one degree of freedom (DoF) system it is necessary to band pass filter the system (in case of a multiple DoF system) and limit the ID to one filtered mode. In order to keep the subscripts to a minimum,  $v(t) = y_r(t)$  is used for the following explanation of the HT.

As a first step, the HT (shifting the signal by  $90^\circ$ ) is applied to the filtered (one DoF) time discrete signal  $v(t)$ . The sum of the original signal and its HT  $\tilde{v}(t)$  compose the analytical signal  $V(t)$  written in polar coordinates:

$$V(t) = v(t) + i\tilde{v}(t). \quad (2.2)$$

The amplitude or decay envelope  $A(t)$  can be directly gained from the absolute value of  $V(t)$ . Using the time dependent natural frequency  $\omega_n(t)$  and critical damping coefficient  $\zeta(t)$  of the system, the amplitude of the single mode signal can be also approximated by:

$$A_r(t) = |V(t)| = A_0 e^{-\zeta(t)\omega_n(t)} \quad (2.3)$$

where  $A_0$  is the amplitude at time zero. The instantaneous phase is obtained from the signal as follows:

$$\varphi(t) = \tan^{-1}(\tilde{v}(t)/v(t)). \quad (2.4)$$

In order to find the natural frequency  $\omega_n(t)$ , a common approach is to use a low-pass filter and then differentiate the phase, e.g., in [5]. This approach, however, is very sensitive to noise. Sumali and Kellogg [15] therefore suggest another method using the time points  $t = t_0, t_1, \dots, t_N$  of the measured response (with  $N$  being the number of data points) and curve fitting the phase signal  $\varphi(t)$  with a polynomial of degree  $p$  (Equation 2.5).

It is to mention that the time signal has to be truncated at the beginning and end before curve fitting because of the end effects of the HT (so  $N$  is the number of data points of the truncated signal) [12].

$$\begin{bmatrix} \varphi(t_0) \\ \varphi(t_1) \\ \vdots \\ \varphi(t_{N-1}) \end{bmatrix} = \begin{bmatrix} t_0^p & \cdots & t_0 & 1 \\ t_1^p & \cdots & t_1 & 1 \\ \vdots & \cdots & \vdots & 1 \\ t_{N-1}^p & \cdots & t_{N-1} & 1 \end{bmatrix} \begin{bmatrix} b_p \\ \vdots \\ b_1 \\ b_0 \end{bmatrix}. \quad (2.5)$$

The polynomial coefficients  $b_0, b_1, \dots, b_p$  can be obtained by a least squares solution of Equation 2.5. The time dependent damped oscillation frequency  $\omega_d$  can then be estimated as the time-derivative of the previously calculated phase signal:

$$\omega_d(t) = \frac{d\varphi(t)}{dt} = \begin{bmatrix} pt_0^{p-1} & \cdots & 1 & 0 \\ pt_1^{p-1} & \cdots & 1 & 0 \\ \vdots & \cdots & \vdots & \vdots \\ pt_{N-1}^{p-1} & \cdots & 1 & 0 \end{bmatrix} \begin{bmatrix} b_p \\ \vdots \\ b_1 \\ b_0 \end{bmatrix}. \quad (2.6)$$

After curve fitting the phase of the signal, the decay envelope is estimated from the amplitude information. Since the response is non-linear, the logarithmic decay envelope is time varying and can also be approximated by a polynomial with the least squares solution of the equation (m order polynomial, here order 3 for simplicity):

$$\begin{bmatrix} \ln|V(t_0)| \\ \ln|V(t_1)| \\ \vdots \\ \ln|V(t_{N-1})| \end{bmatrix} = \begin{bmatrix} t_0^3 & t_0^2 & t_0 & 1 \\ t_1^3 & t_1^2 & t_1 & 1 \\ \vdots & \vdots & \vdots & \vdots \\ t_{N-1}^3 & t_{N-1}^2 & t_{N-1} & 1 \end{bmatrix} \begin{bmatrix} c_3 \\ c_2 \\ c_1 \\ \ln(A_0) \end{bmatrix}. \quad (2.7)$$

Which gives the non-linear decaying envelope:

$$A(t) = A_0 e^{-c_1 t - c_2 t^2 - c_3 t^3}. \quad (2.8)$$

This implies that the following relationship holds:

$$\zeta(t)\omega_n(t) \equiv -C(t) = c_1 + c_2 t + c_3 t^2. \quad (2.9)$$

Using the relationship  $(\omega_d(t))^2 = (\omega_n(t))^2 (1 - (\zeta(t))^2)$ , the time-varying natural frequency  $\omega_n(t)$  can be computed as follows:

$$\omega_n(t) = \sqrt{(\omega_d(t))^2 + (C(t))^2}. \quad (2.10)$$

Finally, the time-varying damping ratio  $\zeta(t)$  results in:

$$\zeta(t) = \frac{-C(t)}{\omega_n(t)}. \quad (2.11)$$

## 2.2 Frequency Based Dynamic Substructuring

The substructuring approach comprises coupling and decoupling of dynamic systems. Coupling describes the process of assembling multiple substructures by adding physical boundary conditions to their common interfaces. Decoupling is the reversed process: Isolating the single substructures by removing the influence of neighboring subsystems. Either way, it is assumed that the dynamic interactions between single components can be represented by a limited set of interface DoFs.

Although it is possible to apply the substructuring ID in an arbitrary domain, this thesis focuses on DS in the frequency domain. An advantage of substructuring in the frequency domain is that it directly uses measured frequency response functions (FRFs) for multiple inputs and outputs. Therefore, the preferred modeling domain for experimental applications is the frequency domain [9]. Unless explicitly stated, the following introduction to frequency based substructuring (FBS) is based on the much more detailed explanation by Van Der Seijs [18].

Equation 2.12 shows the linearized equation of motion of a system with  $n$  substructures in the frequency domain.

$$\mathbf{Z}(\omega)\mathbf{u}(\omega) = \mathbf{f}(\omega) + \mathbf{g}(\omega) \quad (2.12)$$

$$\text{with } \mathbf{Z}(\omega) = \begin{bmatrix} \mathbf{Z}^1(\omega) & & \mathbf{0} \\ & \ddots & \\ \mathbf{0} & & \mathbf{Z}^n(\omega) \end{bmatrix}$$

$$\text{and } \mathbf{u}(\omega) = \begin{bmatrix} \mathbf{u}^1(\omega) \\ \vdots \\ \mathbf{u}^n(\omega) \end{bmatrix}, \quad \mathbf{f}(\omega) = \begin{bmatrix} \mathbf{f}^1(\omega) \\ \vdots \\ \mathbf{f}^n(\omega) \end{bmatrix}, \quad \mathbf{g}(\omega) = \begin{bmatrix} \mathbf{g}^1(\omega) \\ \vdots \\ \mathbf{g}^n(\omega) \end{bmatrix}.$$

$\mathbf{Z}(\omega)$  represents the block-diagonal dynamic stiffness matrix. It contains complex frequency dependent functions that describe the force required to induce a unit harmonic displacement on a particular DoF when all other DoFs are constrained.  $\mathbf{u}(\omega)$  is a vector with all  $n$  DoFs including  $n_2$  DoFs at the interface,  $\mathbf{f}(\omega)$  is the set of externally applied forces and  $\mathbf{g}(\omega)$  the unknown interface forces.

For the following explanation of the coupling process, the interacting substructures A and B in Figure 2.1 are considered.  $(\star)_1$  and  $(\star)_3$  mark internal (far away from the interface) whereas  $(\star)_2$  marks interface DoFs. For a simplified representation, the explicit frequency dependence will be omitted from now on.

For this structure, the vector of displacements, forces and reaction forces can be written as:

$$\mathbf{u} = \begin{bmatrix} \mathbf{u}_1^A \\ \mathbf{u}_2^A \\ \mathbf{u}_2^B \\ \mathbf{u}_3^B \end{bmatrix}, \quad \mathbf{f} = \begin{bmatrix} \mathbf{f}_1^A \\ \mathbf{f}_2^A \\ \mathbf{f}_2^B \\ \mathbf{f}_3^B \end{bmatrix}, \quad \mathbf{g} = \begin{bmatrix} \mathbf{0} \\ \mathbf{g}_2^A \\ \mathbf{g}_2^B \\ \mathbf{0} \end{bmatrix}. \quad (2.13)$$

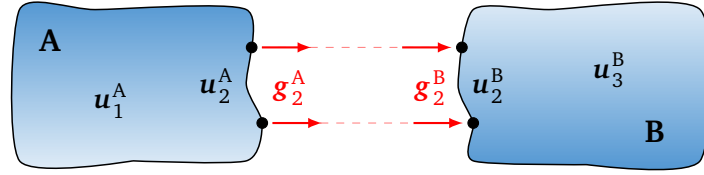


Figure 2.1: Substructures A and B to be assembled

### 2.2.1 Interface Conditions

Substructures are firmly attached to their neighboring structures, which leads to the following two conditions at the interface DoFs that must always be satisfied: compatibility of displacements (compatibility condition) and equilibrium of forces (equilibrium condition).

The **compatibility condition** states that matching interface DoFs need to be equal (value and sign) at both substructures:

$$\mathbf{u}_2^A = \mathbf{u}_2^B. \quad (2.14)$$

Note that  $(\star)^A$  marks physical parameters of the part A and  $(\star)^B$  of part B. Regarding all physical DoFs  $n$  and using a signed Boolean matrix  $\mathbf{B}$  that specifies the pairs of collocated interface DoFs, Equation 2.14 can be written as:

$$\mathbf{B}\mathbf{u} = \mathbf{0}, \quad \mathbf{B}^{n_2 \times n} = \begin{bmatrix} \mathbf{0} & -\mathbf{I} & \mathbf{I} & \mathbf{0} \end{bmatrix}. \quad (2.15)$$

A substitution of the physical coordinates  $\mathbf{u}$  by a global set of generalized coordinates  $\mathbf{q}$  (Equation 2.16) ensures that the compatibility of displacements at the interface is automatically satisfied.

$$\mathbf{u} = \mathbf{L}\mathbf{q} \implies \begin{cases} \mathbf{u}_1^A = \mathbf{q}_1 \\ \mathbf{u}_2^A = \mathbf{q}_2 \\ \mathbf{u}_2^B = \mathbf{q}_2 \\ \mathbf{u}_3^B = \mathbf{q}_3 \end{cases} \quad \text{with} \quad \mathbf{L}^{n \times m} = \begin{bmatrix} \mathbf{I} & \mathbf{0} & \mathbf{0} \\ \mathbf{0} & \mathbf{I} & \mathbf{0} \\ \mathbf{0} & \mathbf{I} & \mathbf{0} \\ \mathbf{0} & \mathbf{0} & \mathbf{I} \end{bmatrix}. \quad (2.16)$$

The mapping of  $n$  physical DoFs  $\mathbf{u}$  of all subsystems to a generalized global set  $\mathbf{q}$  with  $m = n - n_2$  DoFs is realized with the Boolean localization matrix  $\mathbf{L}$  ( $n \times m$ ).

Notable is the relation between the signed Boolean matrix  $\mathbf{B}$  and the localization matrix  $\mathbf{L}$ . Since  $\mathbf{q}$  is the unique set of global DoFs of the assembled system, the compatibility of the physical coordinates  $\mathbf{u}$  in Equation 2.16 is implicitly satisfied for all possible displacements. This means that  $\mathbf{B}$  and  $\mathbf{L}$  are each other's null spaces and one Boolean matrix can be obtained from the other using Equation 2.17.

$$\mathbf{B}\mathbf{u} = \mathbf{B}\mathbf{L}\mathbf{q} = \mathbf{0} \implies \begin{cases} \mathbf{L} = \text{null}(\mathbf{B}) \\ \mathbf{B}^T = \text{null}(\mathbf{L}^T) \end{cases}. \quad (2.17)$$

The second interface condition calls for the **equilibrium of forces** at matching interface DoFs based on Newton's third law *actio et reactio*.

$$\mathbf{g}_2^A = -\mathbf{g}_2^B. \quad (2.18)$$

Back-projecting the vector of reaction forces  $\mathbf{g}$  to the Boolean localization space  $\mathbf{L}$ , the interface forces are directly combined:

$$\mathbf{L}^T \mathbf{g} = \mathbf{0} \implies \begin{cases} \mathbf{g}_1^A = \mathbf{0} \\ \mathbf{g}_2^A + \mathbf{g}_2^B = \mathbf{0} \\ \mathbf{g}_3^B = \mathbf{0} \end{cases}. \quad (2.19)$$

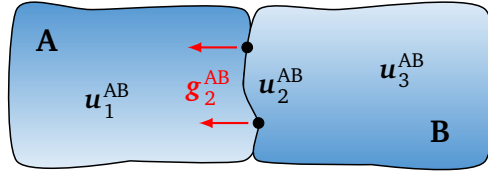


Figure 2.2: Assembled structure AB

The interface condition is established in the second line of Equation 2.19 whereas the other two lines do not affect the interface and are irrelevant for the assembled equations.

Since  $g_2^A$  and  $g_2^B$  only differ in sign, they can be replaced by one set of DoFs using the signed Boolean matrix  $B$  (Equation 2.20). This set of DoFs is called Lagrange multipliers  $\lambda$  and represents the intensity of the interface forces.

$$g = -B^T \lambda \implies \begin{cases} g_1^A = 0 \\ g_2^A = \lambda \\ g_2^B = -\lambda \\ g_3^B = 0 \end{cases} . \quad (2.20)$$

With the implementation of the Lagrange multipliers, the equilibrium at the interface is automatically satisfied for all interface forces. This can be verified by rewriting Equation 2.19 using the mathematical relationship between  $L$  and  $B$  of Equation 2.17.

$$L^T g = -L^T B^T \lambda = 0 \quad \forall g. \quad (2.21)$$

### 2.2.2 Coupling in the Frequency Domain

Combining the interface conditions for the assembled system with the equation of motion in Equation 2.12, the frequency-based formulation of the substructuring problem (equations of motions) becomes:

$$\begin{aligned} Zu &= f + g \\ Bu &= 0 \\ L^T g &= 0. \end{aligned} \quad (2.22)$$

Coupling or decoupling the substructures using the equations above is very expensive. Hence additional information regarding the interface or a reduction of the number of unknowns is required. This can be realized with the primal or dual approach. For the primal approach, the compatibility condition is satisfied a priori and the equations of motion can be solved for a unique set of interface displacements. In contrast, for the dual approach the equilibrium conditions are satisfied before solving the equations for a new set of interface forces. The following section presents the coupling and decoupling approach for the primal as well as the dual formulation (again, according to the explanation in [18]).

#### Primal Assembly

Primal assembly is the coupling of subsystems using impedance matrices starting with a unique set of generalized coordinates  $q$ . According to Equation 2.16 the physical DoFs  $u$

are mapped to  $\mathbf{q}$  by defining an appropriate localization Boolean matrix  $\mathbf{L}$ . As a consequence, the compatibility condition is already satisfied and the equations of motion of the primal substructuring problem lead to:

$$\begin{aligned} \mathbf{Z}^{AB} \mathbf{L} \mathbf{q} &= \mathbf{f} + \mathbf{g} \\ \mathbf{L}^T \mathbf{g} &= \mathbf{0} \end{aligned} \quad (2.23)$$

with

$$\mathbf{Z}^{AB} = \begin{bmatrix} \mathbf{Z}^A & \mathbf{0} \\ \mathbf{0} & \mathbf{Z}^B \end{bmatrix}, \quad \mathbf{Z}^A = \begin{bmatrix} \mathbf{Z}_{11}^A & \mathbf{Z}_{12}^A \\ \mathbf{Z}_{21}^A & \mathbf{Z}_{22}^A \end{bmatrix}, \quad \mathbf{Z}^B = \begin{bmatrix} \mathbf{Z}_{22}^B & \mathbf{Z}_{23}^B \\ \mathbf{Z}_{32}^B & \mathbf{Z}_{33}^B \end{bmatrix}.$$

In order to solve the system, the interface forces are eliminated by multiplying the first row with  $\mathbf{L}^T$ . The remaining equations of motion of the assembled system for the generalized interface displacements  $\mathbf{q}$  and associated generalized forces  $\mathbf{p}$  are:

$$\tilde{\mathbf{Z}}^{AB} \mathbf{q} = \mathbf{p}, \quad \tilde{\mathbf{Z}}^{AB} = \mathbf{L}^T \mathbf{Z}^{AB} \mathbf{L} \quad \text{and} \quad \mathbf{p} = \mathbf{L}^T \mathbf{f} \quad (2.24)$$

where  $\tilde{\mathbf{Z}}^{AB}$  is the primally assembled impedance for the generalized DoFs. Note that the size of the matrix is reduced according to the number of generalized DoFs that are considered. To elucidate, the primally assembled impedance of the system shown in Figure 2.2 leads to:

$$\tilde{\mathbf{Z}}^{AB} = \mathbf{L}^T \mathbf{Z}^{AB} \mathbf{L} \implies \begin{bmatrix} \mathbf{Z}_{11}^A & \mathbf{Z}_{12}^A & \mathbf{0} \\ \mathbf{Z}_{21}^A & \mathbf{Z}_{22}^A + \mathbf{Z}_{22}^B & \mathbf{Z}_{23}^B \\ \mathbf{0} & \mathbf{Z}_{32}^B & \mathbf{Z}_{33}^B \end{bmatrix} = \mathbf{L}^T \begin{bmatrix} \mathbf{Z}_{11}^A & \mathbf{Z}_{12}^A & \mathbf{0} & \mathbf{0} \\ \mathbf{Z}_{21}^A & \mathbf{Z}_{22}^A & \mathbf{0} & \mathbf{0} \\ \mathbf{0} & \mathbf{0} & \mathbf{Z}_{22}^B & \mathbf{Z}_{23}^B \\ \mathbf{0} & \mathbf{0} & \mathbf{Z}_{32}^B & \mathbf{Z}_{33}^B \end{bmatrix} \mathbf{L} \quad (2.25)$$

with the localization matrix

$$\mathbf{L} = \begin{bmatrix} \mathbf{I} & \mathbf{0} & \mathbf{0} \\ \mathbf{0} & \mathbf{I} & \mathbf{0} \\ \mathbf{0} & \mathbf{I} & \mathbf{0} \\ \mathbf{0} & \mathbf{0} & \mathbf{I} \end{bmatrix}. \quad (2.26)$$

### Dual Assembly

Starting from the general equation of motion of the substructuring problem (Equation 2.12), the dual approach chooses Lagrange multipliers  $\boldsymbol{\lambda}$  as a set of coupling forces according to the relation in Equation 2.20. The equilibrium of forces is thus satisfied a priori instead of the compatibility condition in the primal approach. The dual assembly also uses admittance matrices instead of impedances. The equation of motion of the substructuring problem using admittances and Lagrange multipliers is:

$$\mathbf{u} = \mathbf{Y}^{AB} (\mathbf{f} - \mathbf{B}^T \boldsymbol{\lambda}) \quad (2.27)$$

with

$$\mathbf{Y}^{AB} = \begin{bmatrix} \mathbf{Y}^A & \mathbf{0} \\ \mathbf{0} & \mathbf{Y}^B \end{bmatrix}, \quad \mathbf{Y}^A = \begin{bmatrix} \mathbf{Y}_{11}^A & \mathbf{Y}_{12}^A \\ \mathbf{Y}_{21}^A & \mathbf{Y}_{22}^A \end{bmatrix}, \quad \mathbf{Y}^B = \begin{bmatrix} \mathbf{Y}_{22}^B & \mathbf{Y}_{23}^B \\ \mathbf{Y}_{32}^B & \mathbf{Y}_{33}^B \end{bmatrix}.$$

In addition, the dual approach enforces the compatibility of displacements by adding Equation 2.15 to the problem instead of a unique set of generalized coordinates. The problem formulation for the dual approach becomes:

$$\mathbf{u} = \mathbf{Y}^{AB} (\mathbf{f} - \mathbf{B}^T \boldsymbol{\lambda}) \quad (2.28a)$$

$$\mathbf{B} \mathbf{u} = \mathbf{0}. \quad (2.28b)$$



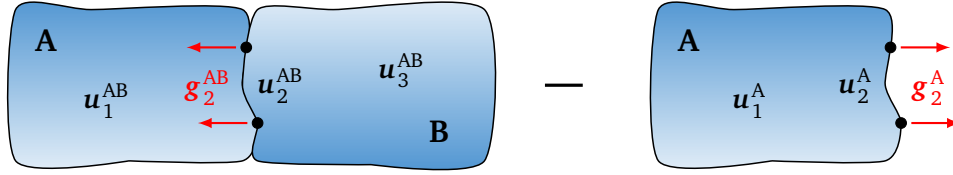


**Figure 2.3:** Decoupling of substructure A from the assembly AB to gain B

The system now has as many equations as unknowns ( $n$  DoFs and  $n_2$  interface DoFs result in  $n + n_2$  equations).

Substituting Equation 2.28a into the compatibility constraint in Equation 2.28b and solving it for  $\lambda$  (forces to keep the substructures assembled) results in:

$$\lambda = (\mathbf{B}\mathbf{Y}^{\text{AB}}\mathbf{B}^{\text{T}})^{-1} \mathbf{B}\mathbf{Y}^{\text{AB}}\mathbf{f}. \quad (2.29)$$

Note that  $\Delta\mathbf{u} = \mathbf{B}\mathbf{Y}^{\text{AB}}\mathbf{f}$  is the displacement gap that is formed between the still uncoupled subsystems caused by the applied excitation forces  $\mathbf{f}$ . In order to attach the subsystems to each other, the interface forces  $\lambda$ , defined by the Lagrange multipliers, need to be applied.

Substituting  $\lambda$  from Equation 2.29 back into the Equation 2.28a gives the coupled response  $\mathbf{u}$ :

$$\mathbf{u} = \mathbf{Y}^{\text{AB}}\mathbf{f} - \mathbf{Y}^{\text{AB}}\mathbf{B}^{\text{T}}(\mathbf{B}\mathbf{Y}^{\text{AB}}\mathbf{B}^{\text{T}})^{-1} \mathbf{B}\mathbf{Y}^{\text{AB}}\mathbf{f}. \quad (2.30)$$

This formulation is referred to as Lagrange multipliers - FBS (LM-FBS). The dually assembled FRF matrix  $\tilde{\mathbf{Y}}^{\text{AB}}$  is gained by collecting the admittance terms:

$$\tilde{\mathbf{Y}}^{\text{AB}} = [\mathbf{I} - \mathbf{Y}^{\text{AB}}\mathbf{B}^{\text{T}}(\mathbf{B}\mathbf{Y}^{\text{AB}}\mathbf{B}^{\text{T}})^{-1} \mathbf{B}] \mathbf{Y}^{\text{AB}}. \quad (2.31)$$

### 2.2.3 Decoupling in the Frequency Domain

The previous section presented the coupling of substructures, which can be interpreted as the addition of two substructures:  $AB = A + B$ . The reverse operation is the decoupling, or the subtraction of a substructure from the assembly:  $AB - A = B$ . It consists of removing the dynamic influence of a substructure from the assembly in order to retrieve the remaining subsystem.

As well as coupling, decoupling can be performed applying the primal or dual formulation. In the following, only the primal disassembly is explained. Dual decoupling will not be used in this thesis. The example of Figure 2.2 is considered again, whereas Figure 2.3 illustrates its disassembling procedure.

Considering only interface DoFs  $(*)_2$  for the decoupling approaches and neglecting internal information, the vector of displacements, forces and reaction forces can be written as:

$$\mathbf{u} = \begin{bmatrix} \mathbf{u}_1^{\text{AB}} \\ \mathbf{u}_2^{\text{AB}} \\ \mathbf{u}_3^{\text{AB}} \\ \mathbf{u}_1^{\text{A}} \\ \mathbf{u}_2^{\text{A}} \end{bmatrix}, \quad \mathbf{f} = \begin{bmatrix} \mathbf{0} \\ \mathbf{f}_2^{\text{AB}} \\ \mathbf{f}_3^{\text{AB}} \\ \mathbf{0} \\ \mathbf{0} \end{bmatrix}, \quad \mathbf{g} = \begin{bmatrix} \mathbf{0} \\ \mathbf{g}_2^{\text{AB}} \\ \mathbf{0} \\ \mathbf{0} \\ -\mathbf{g}_2^{\text{A}} \end{bmatrix}. \quad (2.32)$$

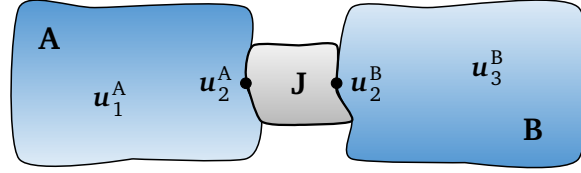


Figure 2.4: Assembled structure AJB

### Primal Disassembly

The decoupling operation in the primal domain can be formulated as a coupling between the dynamic stiffness  $Z^{AB}$  of the assembled system and the negative dynamic stiffness of substructure A  $Z^A$ . Hence, the primal decoupling is performed by subtracting the substructure's (here A) impedance from the assembly with respect to its mapping in the global system matrix and in the Boolean localization matrix  $L$  as in Equation 2.24:

$$\tilde{Z}^B = L^T Z^{AB|A} L \implies \begin{bmatrix} \cdot & \cdot & \cdot & \cdot \\ \cdot & Z_{22}^B & Z_{23}^B & \cdot \\ \cdot & Z_{32}^B & Z_{33}^B & \cdot \\ \cdot & \cdot & \cdot & \cdot \end{bmatrix} = L^T \begin{bmatrix} \cdot & \cdot & \cdot & \cdot & \cdot \\ \cdot & Z_{22}^{AB} & Z_{23}^{AB} & \cdot & \mathbf{0} \\ \cdot & Z_{32}^{AB} & Z_{33}^{AB} & \cdot & \mathbf{0} \\ \cdot & \cdot & \cdot & \cdot & \cdot \\ \cdot & \mathbf{0} & \mathbf{0} & \cdot & -Z_{22}^A \end{bmatrix} L \quad (2.33)$$

with

$$L = \begin{bmatrix} \cdot & \cdot & \cdot & \cdot \\ \cdot & I & \mathbf{0} & \cdot \\ \cdot & \mathbf{0} & I & \cdot \\ \cdot & \cdot & \cdot & \cdot \\ \cdot & I & \mathbf{0} & \cdot \end{bmatrix}.$$

The dots represent neglected terms containing information about internal DoFs.

### Inverse Substructuring

For the decoupling procedure, a primal approach called inverse (or in-situ) substructuring was proposed by Meggitt and Moorhouse [11]. The basic concept of this approach is shown in this subsection.

The great advantage of inverse substructuring is that the characterization of substructures only requires measurements of the assembled structure. However, inverse substructuring is limited by the assumptions of a negligible joint mass and no cross coupling between interface DoFs [7]. Hence, it must be evaluated to what extent these prerequisites apply to the considered test system. The description of inverse substructuring follows the one given in [7].

Let us consider an assembled system AJB with the substructures A and B connected by the joint J as depicted in Figure 2.4. Starting point is a matrix with measured FRFs in which the dynamic info is coupled among all terms of the matrix. The impedance representation is gained by inverting the matrix. There, the topology of the information is distinguishable. For the inversion process, only interface measurements are used. The assembled impedance matrix of the system is:

$$Z^{AJB} = \begin{bmatrix} Z_{11}^{AJB} & Z_{12}^{AJB} \\ Z_{21}^{AJB} & Z_{22}^{AJB} \end{bmatrix} = \begin{bmatrix} Z_{11}^A + Z_{11}^J & Z_{12}^J \\ Z_{21}^J & Z_{22}^B + Z_{22}^J \end{bmatrix}. \quad (2.34)$$

Thereby, the off-diagonal terms of the dynamic stiffness in Equation 2.34 represent the properties of the joint J itself:

$$\mathbf{Z}_{21}^{\text{AJB}} = \mathbf{Z}_{21}^{\text{J}}, \quad \mathbf{Z}_{12}^{\text{AJB}} = \mathbf{Z}_{12}^{\text{J}}. \quad (2.35)$$

Assuming a negligible mass of the joint and no cross coupling between interface DoFs (for an examination of the two assumptions refer to [7]), the following assumption can be made:

$$\mathbf{Z}_{11}^{\text{J}} \approx -\mathbf{Z}_{12}^{\text{J}} \approx -\mathbf{Z}_{21}^{\text{J}} \approx \mathbf{Z}_{22}^{\text{J}}. \quad (2.36)$$

In addition, with no cross coupling between interface DoFs,  $\mathbf{Z}_{12}^{\text{J}}$  and  $\mathbf{Z}_{21}^{\text{J}}$  are diagonal matrices and the dynamic stiffness matrix of the joint J yields:

$$\mathbf{Z}^{\text{J}} = \begin{bmatrix} \mathbf{Z}_{11}^{\text{J}} & \mathbf{Z}_{12}^{\text{J}} \\ \mathbf{Z}_{21}^{\text{J}} & \mathbf{Z}_{22}^{\text{J}} \end{bmatrix} \approx \begin{bmatrix} -\text{diag}(\mathbf{Z}_{12}^{\text{AJB}}) & \text{diag}(\mathbf{Z}_{12}^{\text{AJB}}) \\ \text{diag}(\mathbf{Z}_{12}^{\text{AJB}}) & -\text{diag}(\mathbf{Z}_{12}^{\text{AJB}}) \end{bmatrix}. \quad (2.37)$$

In conclusion, the inverse substructuring approach consist of measuring the FRF matrix  $\mathbf{Y}^{\text{AJB}}$  of the assembled system and inverting it to the dynamic stiffness  $\mathbf{Z}^{\text{AJB}}$ . Provided that the assumptions of a negligible joint mass and no DoF cross coupling at the interface hold, the joint properties can be extracted by using the off-diagonal blocks  $\mathbf{Z}_{12}^{\text{AJB}}$  and  $\mathbf{Z}_{21}^{\text{AJB}}$  (Equation 2.35).

#### 2.2.4 Virtual Point Transformation

Since the interface DoFs measured on both sides of an interface are usually non-collocated (not at matching locations), the compatibility as well as the equilibrium condition is not satisfied at the common interface. To obtain collocated interface DoFs, the Virtual Point Transformation (VPT) proposed in [13] projects all translational input and output signals onto a subspace of three translations and three rotations, the so-called Interface Displacement Modes (IDMs) of the virtual point (VP). For this transformation to be valid, the interface is assumed as rigid. The transformation process is illustrated in Figure 2.5 and briefly summarized in the following. For a more detailed description refer to [13].

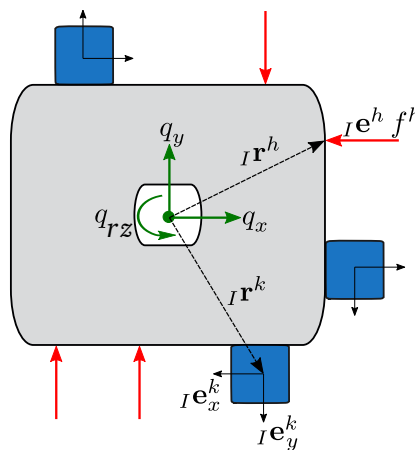


Figure 2.5: Virtual point transformation

The measured FRF matrix  $\mathbf{Y}_{uf}^{\text{AJB}}$  with accelerations (or velocities/displacements)  $\mathbf{u}$  and forces  $\mathbf{f}$  is reduced to a matrix  $\mathbf{Y}_{qm}^{\text{AJB}}$  with three generalized rigid displacements and three rotations  $\mathbf{q} = [q_x, q_y, q_z, q_{rx}, q_{ry}, q_{rz}]^T$  as well as three generalized forces and three moments

$\mathbf{m} = [m_x, m_y, m_z, m_{rx}, m_{ry}, m_{rz}]^T$ . Depending on the structure, at least one VP is defined per interface.

The reduction is expressed via the subspaces  $\mathbf{R}_u$  and  $\mathbf{R}_f$ :

$$\mathbf{u} = \mathbf{R}_u \mathbf{q} \quad \mathbf{m} = \mathbf{R}_f^T \mathbf{f} \quad (2.38)$$

where  $\mathbf{R}_u$  comprises the information of each sensor about distance and orientation  ${}_I \mathbf{r}^k$  of the sensor axis  ${}_I \mathbf{e}^k$  with respect to the VP. The subscript  $(\star)^k$  describes the triaxial sensor  $k$  and  ${}_I(\star)$  the absolute frame on which sensor  $k$  is projected.  $\mathbf{R}_f$  holds the information of each impact position with respect to the VP including the direction  ${}_I \mathbf{e}^h$  of impact  $f^h$  at the distance  ${}_I \mathbf{r}^h$  to the VP.

In order to transform the measurements onto the IDMs, a least squares solution is computed using the pseudoinverse  $\mathbf{T}_u$  of  $\mathbf{R}_u$  and  $\mathbf{T}_f$  of  $\mathbf{R}_f$ :

$$\mathbf{q} = \underbrace{(\mathbf{R}_u^T \mathbf{R}_u)^{-1} \mathbf{R}_u^T}_{\mathbf{T}_u} \mathbf{u} \quad \mathbf{f} = \underbrace{(\mathbf{R}_f^T \mathbf{R}_f)^{-1}}_{\mathbf{T}_f^T} \mathbf{m} \quad (2.39)$$

The measured FRF matrix  $\mathbf{Y}_{uf}^{\text{AJB}}$  can now be transformed onto a FRF matrix  $\mathbf{Y}_{qm}^{\text{AJB}}$  containing the rigid body motions around the VP:

$$\mathbf{Y}_{qm}^{\text{AJB}} = \mathbf{T}_u \mathbf{Y}_{uf}^{\text{AJB}} \mathbf{T}_f^T.$$

A convenient side-effect of the VPT is that random as well as systematic measurement errors are filtered out when reducing measured responses and forces with the least squares solution. In addition, rotational DoFs can be reconstructed only using translational measurement equipment.

### 2.3 Zeroed Early-Time Fast Fourier Transform

ZEFFT is an effective method to detect the non-linearity in a system from their free decaying time responses presented by Allen and Mayes [1]. The method can be applied for systems where the non-linearities are only present for a large amplitude response. Since the amplitude of a free decaying time response diminishes quickly, also the non-linearities disappear early in time. Hence, for low amplitudes/late time points, these systems can be approximated as linear so that the free response of the approximately linear system with  $N$  eigenmodes can also be written as:

$$y(t) = \sum_{r=1}^N R_r e^{\lambda_r t} + R_r^* e^{\lambda_r^* t} \quad (2.40)$$

with the complex residue  $R_r$ , eigenvalue  $\lambda_r$ , and  $(\star)^*$  marking the complex conjugate. Since the assumption is made that the non-linearity decays quickly the system only has low damped modes. Therefore, the modal parameters consist of complex conjugate pairs with

$$\lambda_r = -\zeta_r \omega_r + i \omega_r \sqrt{1 - \zeta_r^2}$$

where  $\zeta_r$  is the damping ratio and  $\omega_r$  the natural frequency of the  $r^{\text{th}}$  mode. Its fast Fourier transform (FFT) is:

$$Y(\omega) = \sum_{r=1}^N \left( \frac{R_r}{i\omega - \lambda_r} + \frac{R_r^*}{i\omega - \lambda_r^*} \right). \quad (2.41)$$

Zeroing the time signal  $y(t)$  up to a certain time  $t_z$ :

$$y_z(t) = \begin{cases} 0, & t < t_z \\ y(t), & t \geq t_z \end{cases}$$

leads to the Fourier transform of the zeroed signal:

$$Y_z(\omega) = \sum_{r=1}^N \left( \frac{R_r e^{\lambda_r t_z}}{i\omega - \lambda_r} + \frac{R_r^* e^{\lambda_r^* t_z}}{i\omega - \lambda_r^*} \right) e^{i\omega t_z}. \quad (2.42)$$

The residue of the zeroed signal originates from its initial conditions: at  $t_z$  the residue of the zeroed signal is  $R_r e^{\lambda_r t_z} + R_r^* e^{\lambda_r^* t_z}$ . The parameter  $\lambda_r$  is constant over time. Thus, the Fourier transform of the zeroed signal is the same as in Equation 2.41 apart from the residues that reflect the initial conditions at  $t_z$  or  $t_0$  for the respective time signal. After eliminating the term  $e^{i\omega t_z}$  by multiplying the frequency response with  $e^{-i\omega t_z}$ , the shape of response  $Y_z(\omega)$  is similar to  $Y(\omega)$ , but the residues differ.

To sum up, for the non-linearity detection, it is to select a set of time points  $t_z$  up to which the non-linear time signal  $y(t)$  is zeroed. After generating a set of Fourier transforms  $Y_z$  (one for each zeroing time in  $t_z$ ), called ZEFFTs, one can detect the non-linearity by visually observing the ZEFFTs. For example, characteristics as a distortion around natural frequencies indicate non-linearity. A method to detect non-linearities in a more general way is described in the following section. Note that leakage, which may influence the Fourier transform, is minimized by choosing zeroing times near points where the time response is zero.

### 2.3.1 Backwards Extrapolation for Non-Linearity Detection

Since it is usually not easy to visually discern non-linear behavior from linear behavior in a FRF, Allen and Mayes [1] presented the backwards extrapolation for non-linearity detection (BEND). It shows to which degree a non-linear response deviates from linear behavior. The idea is to approximate the zeroed linear time signal (zeroed up to  $t_z$ ) and extrapolate that signal backwards in time assuming linear behavior. Hence, it is possible to compare the back-extrapolated linear signal to the original non-linear signal.

For the BEND approach, the nearly linear response of a zeroed signal is fit to the form in Equation 2.40 in order to obtain the modal parameters  $\omega$  (vector of eigenfrequencies),  $\zeta$  (damping ratio), and  $\mathbf{R}$  (residue). Each vector contains the respective parameters for all modes.

In order to extrapolate the fitted curve from  $t_2$  back in time to  $t_1$  ( $t_2 > t_1$ ), the residue  $(R_r)_1$  for all modes at  $t_1$  is required and can be calculated using the residue  $(R_r)_2$  at  $t_2$ :

$$(R_r)_1 = (R_r)_2 e^{\lambda_r(t_1 - t_2)} \quad \text{for } r = 1 \dots N. \quad (2.43)$$

Since the response is assumed to be linear, the modal parameters  $\omega$  and  $\zeta$  and therefore  $\lambda$  are constant. Hence, all time points  $t$  and all parameters to reconstruct the linear approximation of the response in the time domain are known. It can be evaluated how much the signal is affected by non-linearities by comparing the back-extrapolated results to the original signal.



## Chapter 3

# Methodology and Implementation of Joint Identification Strategies

As mentioned before, the focus of this thesis is on joint ID with substructuring in the frequency domain. In order to estimate the dynamics of the joints, inverse substructuring is applied to the measured data. Subsequently, the extracted frequency dependent stiffness of the joint is parameterized by a constant. Coupling the parameterized stiffness with separated measurements (parts A and B mechanically unscrewed) allows validate the joint ID by comparing it, inter alia, to the original measurements.

When working in the frequency domain, the measurements are linearized. Thereby, the non-linearities of the system are included in the linearized model. An initial goal of this thesis was to filter out the non-linearities by zeroing and back-extrapolating the data before applying FBS. Thus, the FBS results of the actual linear system can be compared to the results of the original data that include the non-linearities. Due to difficulties in the modal ID, the FBS joint ID based on the zeroed data could not be implemented during this work. However, the foundational implementation for its application is laid. A detailed proposal for a further implementation and usage is given in chapter 5.

Finally, the non-linear joint ID according to HT is applied and its results are evaluated and compared to the one arising from the FBS ID.

This chapter comprises a detailed description of the bolted joint ID methods implemented within this work. First, the implementation of the HT algorithm is described in section 3.1. Subsequently, the FBS process including decoupling, parameterization and coupling is discussed in section 3.2. Finally, the implemented ZEFFT algorithm combined with BE is presented in section 3.3 before introducing design of experiments in section 3.4.

### 3.1 Non-Linear Joint Identification with Hilbert Transform

The following listing summarizes the steps that are applied for the non-linear joint ID with HT before discussing some steps of the approach in more detail.

1. Starting point is the acceleration time response  $y_{acc}(t)$  for one output and one input.
2. Noise filtering and double integration leads to the displacement signal  $y_{dis}(t)$
3. Band pass filtering to gain the mono-modal signal  $y(t)$ .
4. Applying the HT algorithm to  $y(t)$  according to section 2.1 to obtain the amplitude dependent frequency and damping curves.

The basis for the algorithm is a time response  $y_{\text{acc}}(t)$  of an output caused by one input. In order to obtain displacement data, a combination of noise filtering and integration is implemented: For the noise filtering, a Butterworth high-pass filter of order six is designed using the Matlab function `butter()`. First, this filter design is applied to the acceleration data  $y_{\text{acc}}(t)$  with the filter function `filtfilt()`. Subsequently, the velocity data is gained using the integration function `cumtrapz()`. The filter and integration functions are applied once more to obtain the displacement data  $y_{\text{dis}}(t)$ . After the last integration, filtering the data again with the Butterworth filter has proven beneficial in order to remove noise originating from the final integration.

Since HT is limited to single modes, the integrated time data needs to be band pass filtered. Therefore, the band pass filter introduced in [6] is applied to the displacement signal and results in the mono-modal signal  $y(t)$ . The desired mode is selected by giving a small frequency range as input that includes the mode's eigenfrequency.

Finally, the HT algorithm is applied according to the description in section 2.1. A proper choice of filtering range and fitting parameters is shortly addressed in section 4.1. The HT algorithm results in amplitude dependent frequency (backbone) and damping curves of the selected mode. The curves depict the non-linearities of the system and can be used to evaluate how large the error is made by linearizing the measurements during FBS. The algorithm for the non-linear joint ID with HT is implemented in Matlab.

## 3.2 Linear Joint Identification with Frequency Based Substructuring

Inverse Substructuring is used in order to identify the dynamics of the joint. In this section, it is assumed that the measurements consist only of interface DoFs.

Starting point is the measured FRF matrix  $\mathbf{Y}_{uf}^{\text{AJB}}(\omega)$ . With the response  $\mathbf{u}(\omega)$  of all impacts  $\mathbf{f}(\omega)$  the following relationship applies:

$$\mathbf{u}(\omega) = \mathbf{Y}_{uf}^{\text{AJB}}(\omega)\mathbf{f}(\omega). \quad (3.1)$$

Again, the explicit frequency dependence of FRF matrices  $\mathbf{Y}$  and dynamic stiffness matrices  $\mathbf{Z}$  will be omitted. The entire substructuring process is implemented within the pyFBS toolbox [3] (Version 0.2.4).

A first evaluation of the quality of the measurements can be obtained with the driving point passivity. It states that an applied force always results in a displacement in the same direction as the force. For acceleration FRFs, passivity can be assessed by checking if the phase of a driving point is between  $0^\circ$  and  $180^\circ$ . A driving point is characterized by input and output located at the same position and pointing in the same direction.

The data processing for FBS starts with the application of a filter in order to reduce noise and allow an easier ID of the joint properties. The used filter is an in-house development by Trainotti et al. [17].

### 3.2.1 Interface Modeling

After filtering the data, the VPT is applied according to the description in subsection 2.2.4. This results in a  $6 \times 6$  DoFs description of the joint with three translational and three rotational DoFs. In the following, the term DoFs refers to transformed IDMs of the VPs.

Applying the VPT allows to further quantify the quality of the measurements. The consistency



check troubleshoots the test setup and assesses whether the sensor/impact positions and orientations/directions are adhered precisely enough (related to the specifications in  $\mathbf{R}_u$  and  $\mathbf{R}_f$ ). A distinction is made between the overall<sup>1</sup> and specific<sup>2</sup> sensor consistency. In addition, the quality of the transformed data can be assessed with the reciprocity. After the VPT the impacts and DoFs are collocated, meaning that for a good reciprocity  $\mathbf{Y}_{qm}^{AJB}$  is symmetric.

### 3.2.2 Joint Isolation and Parameterization with Inverse Substructuring

The used sensors are acceleration sensors (section 3.4). Hence, the FRF matrix needs to be integrated twice in order to get admittance (also called receptance) data for the joint isolation. This integration is applied in the frequency domain after the VPT. Integrating twice in the frequency domain consists of simply multiplying each entrance in the FRF with  $-1/(2\pi\omega_i)^2$ , where  $\omega_i$  is the associated frequency of the entrance.

The obtained admittance matrix  $\mathbf{Y}_{qm}^{AJB}$  is inverted in order to get the dynamic stiffness matrix  $\mathbf{Z}_{qm}^{AJB}$ . Thus, the joint dynamics  $\mathbf{Z}_{12}^J$  in the off-diagonal terms can be isolated. Assuming no cross coupling, only the diagonal terms of  $\mathbf{Z}_{12}^J$  contain frequency dependent curves depicting the dynamics of the joint. When the condition of no joint mass applies, these curves approach a constant line. Note that this only applies to joints without frequency dependent stiffness or damping as, e.g., a bolted connection. It does not apply to joints of, e.g., viscoelastic materials as rubber. The goal is to approximate the stiffness curves with six frequency independent parameters, three rotations and three translations. Assuming a mass-less joint without viscous damping, the approximation can be realized with the physical parameters stiffness  $\mathbf{K}$  and structural damping  $\mathbf{D}$  as follows:

$$-\mathbf{Z}_{12}^J(\omega) \approx \mathbf{K}^J + j\mathbf{D}^J. \quad (3.2)$$

Thereby the real parts of  $-\mathbf{Z}_{12}^J(\omega)$  correspond to the stiffness  $\mathbf{K}$  and the imaginary parts to the damping  $\mathbf{D}$ .

For the parameterization, the curve fitting function `scipy.optimize.curve_fit()` of `scipy` is used. It fits a given function to given data using least squares. In this case, the input function to fit is a constant, where the input data is the real part of  $-\mathbf{Z}_{12}^J(\omega)$  for the stiffness  $\mathbf{K}$  and the imaginary part of  $-\mathbf{Z}_{12}^J(\omega)$  for the damping  $\mathbf{D}$ . To ensure a (reasonable) result, an initial guess and lower/upper bounds on the parameter to fit are given as an input. The initial guess and bounds are based on a manual evaluation of the plotted real/imaginary  $-\mathbf{Z}_{12}^J(\omega)$ .

For the test structure in this thesis, the damping of the joint is very low compared to the stiffness. This leads to the fact that the noise level is higher than the damping and it is not possible to identify the damping. Hence, the joint dynamics are approximated using the identified stiffness values and neglecting damping. The entire parameterization of the joint  $\mathbf{Z}_{qm}^J(\omega)$  results in:

$$\mathbf{Z}_{qm}^J(\omega) \approx \mathbf{Z}_{qm}^K = \begin{bmatrix} \mathbf{K} & -\mathbf{K} \\ -\mathbf{K} & \mathbf{K} \end{bmatrix} \quad \text{with} \quad \mathbf{K} = \begin{bmatrix} k_x & 0 & 0 & 0 & 0 & 0 \\ 0 & k_y & 0 & 0 & 0 & 0 \\ 0 & 0 & k_z & 0 & 0 & 0 \\ 0 & 0 & 0 & k_{rx} & 0 & 0 \\ 0 & 0 & 0 & 0 & k_{ry} & 0 \\ 0 & 0 & 0 & 0 & 0 & k_{rz} \end{bmatrix}. \quad (3.3)$$

<sup>1</sup>depending on the frequency

<sup>2</sup>accuracy of individual impact/channel positions

### 3.2.3 Reconstruction with the Identified Joint

In order to validate the substructuring process including the joint ID, (mechanically) disassembled measurements are coupled with the parameterized joint and compared to the original, assembled measurements.

Therefore, measured admittances  $Y_{uf}^A$  for part A and  $Y_{uf}^B$  for part B are projected onto the generalized DoFs of the VPs. For the coupling dual assembly (LM-FBS) is used and validated using primal assembly. When applying dual assembly, the admittance matrix  $Y_{qm}^K$  of the parameterized joint is required. However, the joint is parameterized as mass-less and, thus, is no standalone structure. This results in  $Z^K$  being a singular matrix that cannot be inverted. Therefore, the dynamic flexibility matrix  $\Gamma$  is introduced:

$$\Gamma = \begin{bmatrix} \frac{1}{k_x} & 0 & 0 & 0 & 0 & 0 \\ 0 & \frac{1}{k_y} & 0 & 0 & 0 & 0 \\ 0 & 0 & \frac{1}{k_z} & 0 & 0 & 0 \\ 0 & 0 & 0 & \frac{1}{k_{rx}} & 0 & 0 \\ 0 & 0 & 0 & 0 & \frac{1}{k_{ry}} & 0 \\ 0 & 0 & 0 & 0 & 0 & \frac{1}{k_{rz}} \end{bmatrix}. \quad (3.4)$$

The dual coupling of A and B involving  $\Gamma$  leads to:

$$Y_{qm}^{AKB} = Y_{qm}^{AB} - Y_{qm}^{AB} \mathbf{B}^T \left( \mathbf{B} Y_{qm}^{AB} \mathbf{B}^T + \Gamma \right)^{-1} \mathbf{B} Y_{qm}^{AB}. \quad (3.5)$$

A more detailed derivation and validation of the procedure can be found in [10].

Alternatively, a primal coupling formulation can be used. The primal coupling is conducted with:

$$\mathbf{Z}_{qm}^{AKB} = \begin{bmatrix} \mathbf{Z}_{qm}^A & 0 \\ 0 & \mathbf{Z}_{qm}^B \end{bmatrix} + \begin{bmatrix} \mathbf{K} & -\mathbf{K} \\ -\mathbf{K} & \mathbf{K} \end{bmatrix}. \quad (3.6)$$

In order to gain the coupled FRFs  $Y_{qm}^{AKB}$  the resulting  $\mathbf{Z}_{qm}^{AKB}$  must be inverted.

## 3.3 Non-Linearity Elimination with Zeroing and Back-Extrapolation

Substructuring is based on the linearized model of the real non-linear problem. Since this thesis also evaluates the non-linear approach HT, it is of interest how much the system is affected by non-linearities. As described in section 2.3, Allen and Mayes [1] proposed ZEFFT combined with BE in order to recreate the system without non-linearities.

During this work it has become apparent that the BE is very sensitive to the correctness of the identified parameters  $\omega_r$ ,  $\zeta_r$ , and  $R_r$  for the modes. However, the measured dynamics revealed non-passive characteristics and, in general, for non-passive system it is difficult to determine the modal parameters. Hence, identifying the modal parameters for all inputs/outputs accurately enough to use them in the BE cannot be guaranteed.

Nevertheless, within this thesis, the foundation for the combination of ZEFFT and FBS is laid by implementing and testing the BE for one depicted input and one output of the system. This is limited to the BE for a single mode. The process is implemented in Matlab and described in the following.

Starting point is the time signal  $y(t)$  measured for the time interval  $T$ . First, the same band pass filter as used previously (section 3.1) is applied to the signal in order to filter out

one mode. This results in the mono-modal signal  $y_F(t)$ . After zeroing the filtered signal up to time  $t_z$  the signal  $y_{FZ}(t)$  remains (Figure 3.1 left). It is to determine the modal parameters  $\omega_0$  (eigenfrequency),  $\zeta_0$  (damping ratio), and  $R_z$  (residue at  $t_z$ ) for the selected mode in order to apply the BE. The modal ID is described in subsection 3.3.1

Note that  $t_z$  must be chosen thoughtfully by comparing the FFTs of the filtered and zeroed signal (ZEFFTs). The correct determination of  $t_z$  and its influence is discussed in section 4.5.

Finally, the band pass filtered and back-extrapolated time signal  $y_{BE}(t)$  can be calculated using the BE in Equation 2.43 as follows:

$$y_{BE}(t) = R_0 e^{\lambda t} = R_z e^{\lambda(t_0 - t_z)} e^{\lambda t} \quad \text{with} \quad \lambda = -\zeta_0 \omega_0 + i \omega_0 \sqrt{1 - \zeta_0^2} \quad (3.7)$$

To sum up, the approach to filter out present non-linearities consists of the steps listed in the following.

1. Band pass filtering  $y(t)$  to gain a mono-modal signal  $y_F(t)$ .
2. Zeroing  $y_F(t)$  at  $t_z$  leads to  $y_{FZ}(t)$ .
3. Applying modal ID to obtain  $\omega_0$ ,  $\zeta_0$  and  $R_z$  of  $y_{FZ}(t)$ .
4. BE with Equation 3.7 to gain  $y_{BE}(t)$ .

Another idea is to first zero the signal before applying the band pass filter. This procedure is discarded since the filter as well as the modal ID are sensitive to strong irregularities in the ZEFFT which occur when the zeroing times are chosen too high (subsection 4.5.1). In addition, the filter is designed for time signals that start at time zero and not only from  $t_z$ . The abrupt jump at  $t_z$  falsifies the result.

### 3.3.1 Modal Identification for Single DoF Systems

For the modal ID (determining modal parameters) a combination of ID in the frequency and time domain is used by identifying the eigenfrequency  $\omega_0$  in the frequency and damping ratio  $\zeta_0$  together with the residue  $R_z$  in the time domain.

An in-house modal ID in the frequency domain is used to determine the eigenfrequency  $\omega_0$ . The tool is limited to a single mode ID and returns an estimation of  $\omega_0$  and  $\zeta_0$ . It calculates the damped eigenfrequency  $\omega_d$  with a spline interpolation of the given FFT and the damping ratio  $\zeta_0$  using the half-power-method. The natural eigenfrequency is computed from  $\omega_0 = \omega_d \sqrt{1 - 2\zeta_0^2}$ . While the estimation of  $\omega_0$  is good enough for the application in the BE, the identified  $\zeta$  turned out to be too inaccurate. Therefore, an alternative approach to identify  $\zeta_0$  together with the residue  $R_z$  in the time domain is implemented and evaluated.

The FFT used for the modal ID of  $\omega_0$  in the frequency domain is the FFT of the entire time signal including the zeroed part at the beginning. For the implemented modal ID in the time domain, however, the signal is shifted from  $t_z$  to zero ( $\tilde{y}_{FZ}(t)$ ). In other words, the signal is assumed to start at  $t_z$  (signal starting from  $t_z$  shifted to  $t_0 = 0$  s) as depicted in Figure 3.1 with an exemplary decaying time signal.

Considering only the upper envelope  $u(t)$  of the remaining signal  $\tilde{y}_{FZ}(t)$  it is to find  $\zeta_0$  and  $R_z$  such that the following applies:

$$u(t) \stackrel{!}{=} R_z e^{-\omega_0 \zeta_0 t}. \quad (3.8)$$

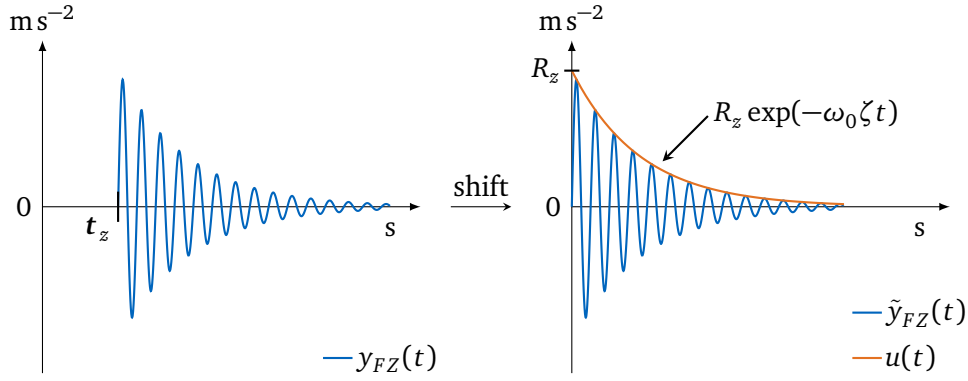


**Figure 3.1:** Shifting zeroed time signal and curve fitting

The upper envelope  $u(t)$  of the signal is detected by the Matlab function `envelope()`. It returns data points approximating the upper and lower envelopes of the input sequence. In this case, the chosen method for the envelope detection is peak picking ('peak'). The algorithm generates a spline over local maxima separated by at least  $N$  points.  $N$  is given as an input and set to the length of  $\tilde{y}_{FZ}(t)$  divided by 100 ( $N = \text{length}(\tilde{y}_{FZ}(t))/100$ ). The choice of  $N$  should be checked for the individual application and adjusted if necessary.

It is now the goal to fit  $\zeta_0$  and  $R_z$  such that Equation 3.8 holds. This is realized with the Matlab minimization function `fminsearch()`. Therefore, the function to minimize depending on  $\zeta_0$  and  $R_z$  is defined:

$$f_{\min}(\zeta_0, R_z, t_i) = R_z e^{-\omega_0 \zeta_0 t_i} - u(t_i) \quad \forall t_i \in T. \quad (3.9)$$

Beside this approach, an alternative method is implemented that calculates  $\zeta_0$  using the logarithmic decrement. After depicting the positive peaks of the signal (equivalent to forming the upper envelope), the logarithmic decrement of every peak with respect to the first peak is estimated.  $\zeta_0$  is calculated from the mean of the detected logarithmic decrements. This, however, is very sensitive to the time duration of the measurement. More precisely, when the time signal decays very early with respect to the measuring time  $T$ , a large part of the signal is zero (only noise remains). However, all the values at which the signal is already flattened are included in the mean value calculation and falsify the result. Thus, the procedure is unsuitable for the general use case. In order to apply the method nevertheless, it is possible to specify an individual time window for each signal.  $\zeta_0$  is then calculated for the signal within the time window.

### 3.4 Design of Experiments

The test structure used to evaluate and compare the implemented approaches consists of two straight beams A and B (each 340 mm × 28 mm × 11 mm) screwed together with a M10 bolt (one screw, one nut, two flat washers) as shown in Figure 3.2. The coordinate origin is located at the back corner of B in the shown assembly. The x-axis is red, the y-axis green, and z-axis blue, where the y-axis points outward. The contact area between the beams goes over 100 mm along the beams (100 mm × 28 mm). To imitate free-free boundary conditions, the assembly is hung with fishing lines.

As impact method, hammer testing is chosen because it is simple to perform without adding extra mass or stiffness to the system (as it is the case for, e.g., shaker testing). Additionally, a hammer impact excites multiple modes in a wide frequency range depending

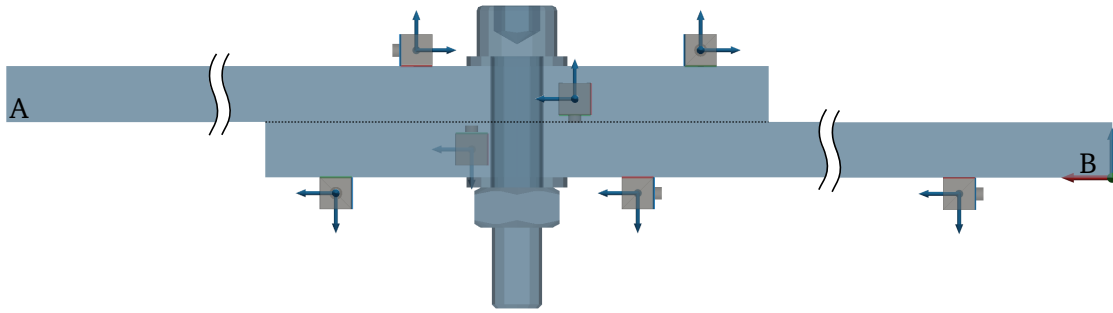


**Figure 3.2:** Assembled test structure with sensors (gray) and channels (blue)

on the used hammer tip [4]. This allows to directly evaluate the beam's behavior for the entire frequency range of interest (1 Hz – 2000 Hz). The used hammer has a sensitivity of  $2.25 \text{ mVN}^{-1}$  and a plastic tip.

The measurements are performed on PAK data acquisition system at room temperature with a sampling rate of 16 384 Hz and a frequency resolution of 0.25 Hz.

### 3.4.1 Structural Design

For FBS and HT, a different design of experiments has been used and is described in the following.

#### Measurements for FBS

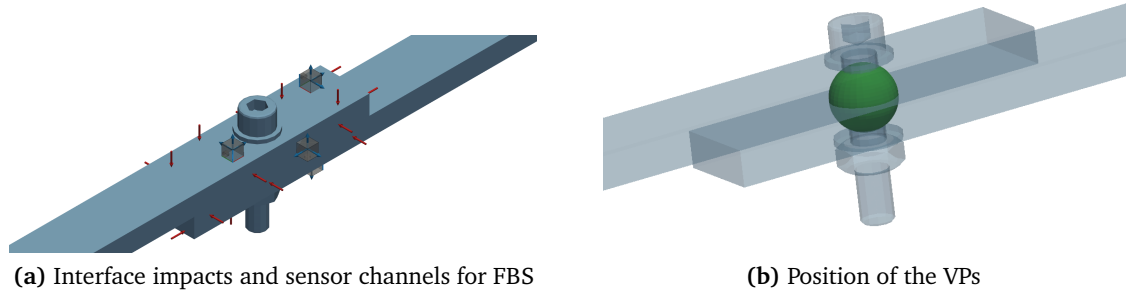
During one test run for FBS of the assembled system, eleven impact positions near the interface of the upper cross A and eleven positions on the lower cross B are excited with hammer impacts of 100 N. Responses are measured with three triaxial accelerometers (sensitivity around  $10 \text{ mVg}^{-1}$ ) near the interface on each beam.

Figure 3.3a shows the impacts (red) and the sensors (gray) each containing three channels (blue) at the interface. The sensors at the interface are also shown in Figure 3.2 with an additional sensor placed on the end (outer side of the assembly) of beam B. The extra sensor measures three internal impacts at the end of beam A. Those internal measurements are applied for additional evaluations but will not be regarded within this report.

Although the surface for impact positions in the x-direction (along the beam) is small, it is possible to apply hammer impacts in all three directions at the interface. Thus, translations in all three directions can be observed with the triaxial sensors. Transformed onto the IDMs, it is possible to control all 3 translational and 3 rotational DOFs of the VP. The locations of the VPs of A and B (one VP per part) are shown in 3.3b. They are at the same position and exactly in the middle of the interfaces.

To sum up, a linear test run of the assembled system results in a  $21 \times 25$  FRF matrix  $\mathbf{Y}_{uf}^{AJB}(\omega)$  containing the transfer function of 22 interface and three internal impacts detected by 18 interface and three internal sensor channels. During the entire report, the  $18 \times 22$  FRF matrix with only interface DOFs is considered. Note that each FRF is estimated from at least four averages with an H1-estimator. The DOFs on the upper beam will be given the subscript  $(*)_1$  and the ones on the lower beam the subscript  $(*)_2$ .

In order to apply coupling with the identified stiffness, measurements of each beam individually are required. Since the weight of the screw has a significant share in the total



**Figure 3.3:** Design of experiment for FB

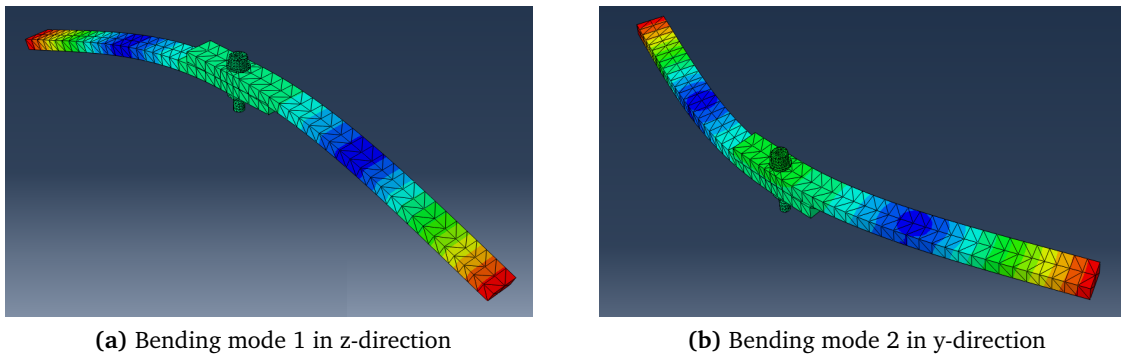


**Figure 3.4:** Modal analysis with Abaqus CAE: mode 1 and mode 2

weight of the assembled structure, the influence of its weight must be considered during the coupling process. Therefore, both beams are measured once with and once without the bolt (screw, nut, and flat washers). Thus, for the evaluation all possible combinations in the coupling process can be tested. In the following, the superscript  $(*)^*$  is used for a beam with the bolt, e.g.,  $A^*$ . The term *separated* is used for the mechanically disassembled (unscrewed) state of the beams and *disassembled/decoupled* states the result of FBS decoupling.

For the verification of the result with the used sensors, additional measurements with other sensors are performed. Those sensors have a higher sensitivity (around  $100 \text{ mV g}^{-1}$ ) but add more mass to the system since they are heavier (and bigger). Tests with these sensors are titled 'big sensors'.

### Measurements for HT

For the application of the HT algorithm, only the measurements of a single input and output are required. Since the approach is limited to single modes, it is to ensure that the desired mode is excited when impacting at the selected impact position. At the same time, the mode must be observable at the chosen channel position. To ensure the excitation/observability, a modal analysis is conducted with Abaqus CAE in advance. The focus in this thesis is on the first two bending modes shown in Figure 3.4. They are of interest, since the bending of both modes activates the joint. The first bending mode will be called 'mode 1' and the second 'mode 2'.

Mode 1 at approximately 156 Hz bends in z-direction and mode 2 at approximately 380 Hz bends in y-direction. Note that the eigenfrequencies determined by Abaqus CAE do not exactly match the experimentally identified eigenfrequencies but give a first idea of their approximate values. According to the mode shapes, one impact is applied in (minus) z- and one

in  $y$ -direction. The chosen sensor position corresponds to one of the sensors on the bottom of B that is also used for the tests for FBS. The two impacts and two sensor channels can be seen in Figure 3.5. Note that the remaining sensors that are used for FBS testing are still attached to the assembly during HT testing to obtain the same environmental conditions. Since the results of the HT may depend on the level of the force, impacts with three different force levels are applied: 10 N, 100 N, and 500 N.

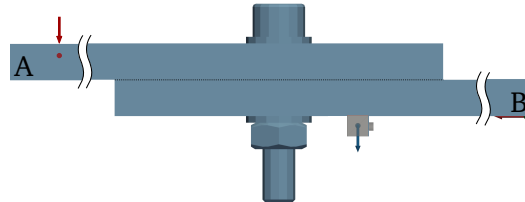


**Figure 3.5:** Impacts and sensor channels for HT

### 3.4.2 Measurement Campaign

During a test campaign, the preload applied to the bolt is successively increased to evaluate the influence of the torque level on the assembly's dynamics and the joint. The torque levels applied are 5 N m, 10 N m, 20 N m, and 50 N m. In order to obtain a variety of test results for a comprehensive evaluation, several test campaigns are performed and presented in Figure 3.6.

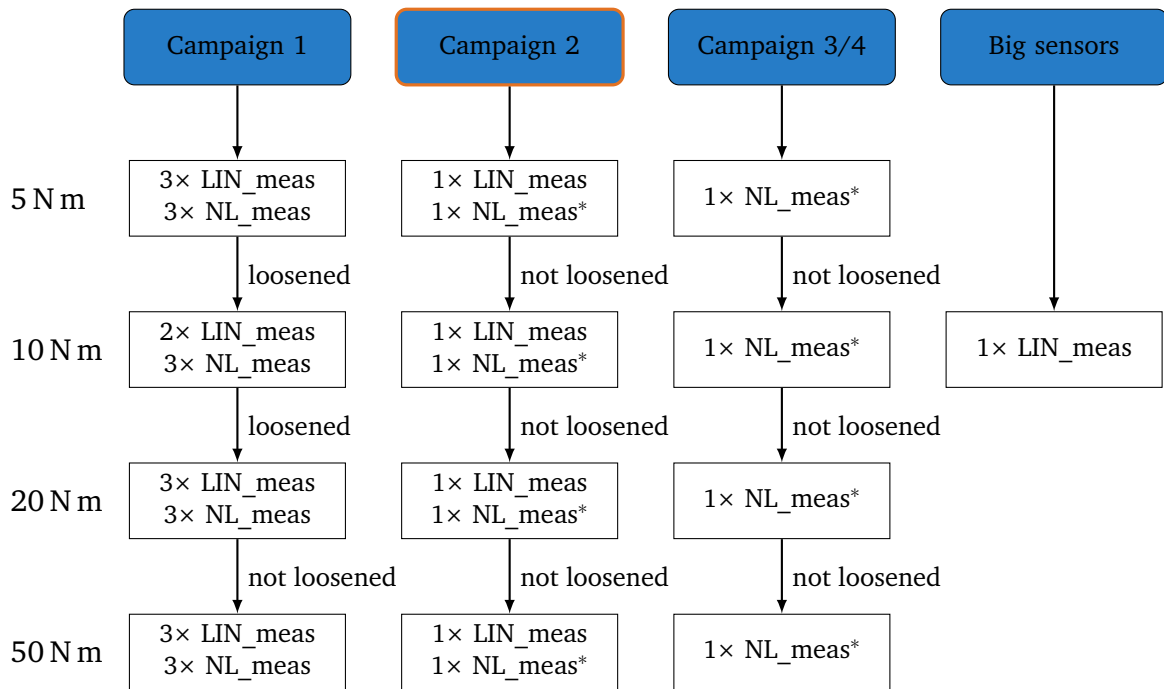
Campaign 1, e.g., starts with three measurement runs for FBS (LIN\_meas) at a torque level of 5 N m. Thereby, one run exists of the 25 hammer impacts measured by 21 channels, as described above. After the three runs for FBS, another three runs for HT are performed. One run for HT comprises two impacts measured by two sensor channels. Subsequently, the bolt is loosened and tightened again with 10 N m. The further procedure is equivalent. For Campaign 1 at 10 N m, only two measurement runs for FBS are available, since one run is lost due to technical problems. The designation 'not loosened' marks transitions from torque level to torque level, where the screw has not been loosened before tightening ('loosened' vice versa).

The evaluation focuses on campaign 2. During this campaign, for each torque level one test run for FBS and one run for HT (only with 100 N) is conducted. Special care is taken to ensure that the interface is not changed/loosened when moving to the next torque level. Campaign 1 is used to investigate the general repeatability of the joint parameterization and the influence of the force level on HT. Campaign 3 and 4 include only tests for HT to investigate the influence of the torque level on HT without performing FBS tests in between. 'Big sensors' is the campaign with the big sensor set conducted at a torque level of 10 N m.

The separated measurement campaigns are summarized in Figure 3.7. The campaign with the bolt attached to A (A\*B) is repeated three times and the campaign with the bolt attached to B (AB\*) is conducted once.

To refer to individual test runs the following abbreviation is introduced: *campaign - torque level - linear/non-linear*. E.g., 'C2-5 N m-LIN' designates the measurement campaign 2 at a torque level of 5 N m for FBS (LIN\_meas). For campaign 1, LIN1/LIN2/LIN3 is used to refer to the first/second/third run of the corresponding torque level.

Figure 3.8 shows a picture of the test structure with the attached sensors and hanging from the ceiling with fishing lines.

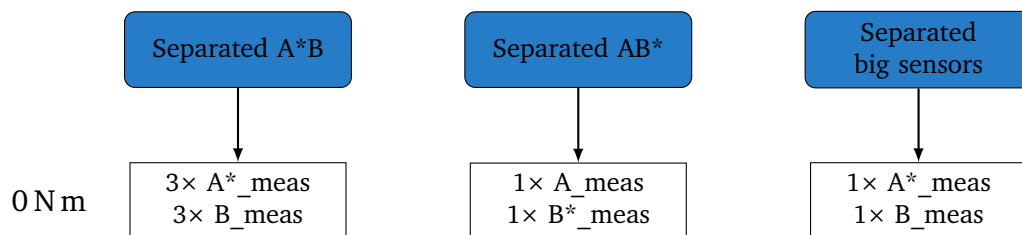


**LIN\_meas:** 25 impacts, 21 channels  
Force ≈ 100 N

**NL\_meas:** 2 impacts, 2 channels  
Force ≈ 10 N, 100 N, 500 N

**NL\_meas\*:** 2 impacts, 2 channels  
Force ≈ 100 N

Figure 3.6: Assembled measurement campaign for FBS and HT



**A/A\*\_meas:** 14 impacts, 9 channels  
Force ≈ 100 N

**B/B\*\_meas:** 11 impacts, 12 channels  
Force ≈ 10 N, 100 N, 500 N

Figure 3.7: Separated measurement campaign for FBS



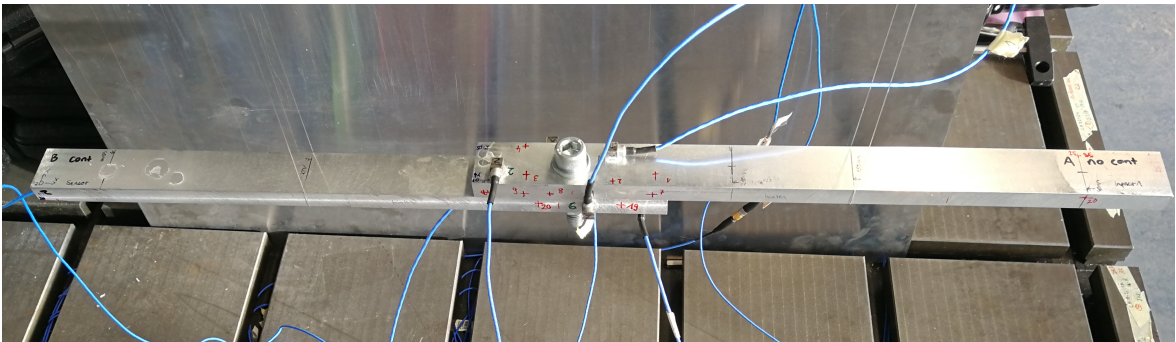


Figure 3.8: Suspension of the test structure with attached sensors



# Chapter 4

## Application and Results

This chapter contains a detailed presentation and evaluation of the joint ID results obtained through tests performed on the beam-like system. First, the non-linear Joint ID with HT is discussed by showing the results of the individual steps. Subsequently, the entire FBS process including parameterization and coupling is analyzed in detail before the results of FBS coupling and HT are compared. Finally, the approach and potential of ZEFFTs together with BE are presented.

### 4.1 Calculation of Frequency and Damping Curves

The joint ID with HT results in the amplitude dependent frequency (backbone) and damping curves of the joint. For the demonstration of the process one of the three non-linear test runs of 'C1-5 Nm-NL' with an impact force of 100 N in  $z$ -direction is used before comparing all tests for HT against each other.

Figure 4.1 shows the original acceleration over time signal and its corresponding integrated and noise filtered displacement signal.

Following the integration, the regarded mode (here: mode 1) is extracted using the band pass filter as shown in Figure 4.2.

Subsequently, the HT of the band pass filtered time signal is formed to receive the analytical signal (Equation 2.2). Before curve fitting the amplitude and phase of the analytical signal with a polynomial, it is necessary to determine the time interval for the curve fitting. The start time is chosen as early as possible. However, attention must be paid to exclude possible irregularities due to the previous processing. The ending time of the interval is chosen at the time when the signal has decayed (lower than the noise level). The exact time interval is determined for each signal individually and may need several readjustments. The signal cut according to the chosen time interval can be seen in Figure 4.3.

It is now necessary to curve fit the amplitude and phase of the cut analytical signal using a polynomial. In this thesis, a polynomial of order nine is chosen. Figure 4.4 depicts the polynomial fit compared to the Hilbert amplitude and phase. It must be mentioned that the amplitude is formed from the average of four different response functions to be consistent with the linear approach where one FRF is formed by the average of four by an H1-estimator. The same applies to the phase. Finally, calculating the amplitude dependent frequency with Equation 2.10 and damping with Equation 2.11 results in Figure 4.5.

Figure 4.6 shows the influence of different impact forces on the backbone and damping curve. An increased impact force entails an increase in amplitude. The curves do not perfectly

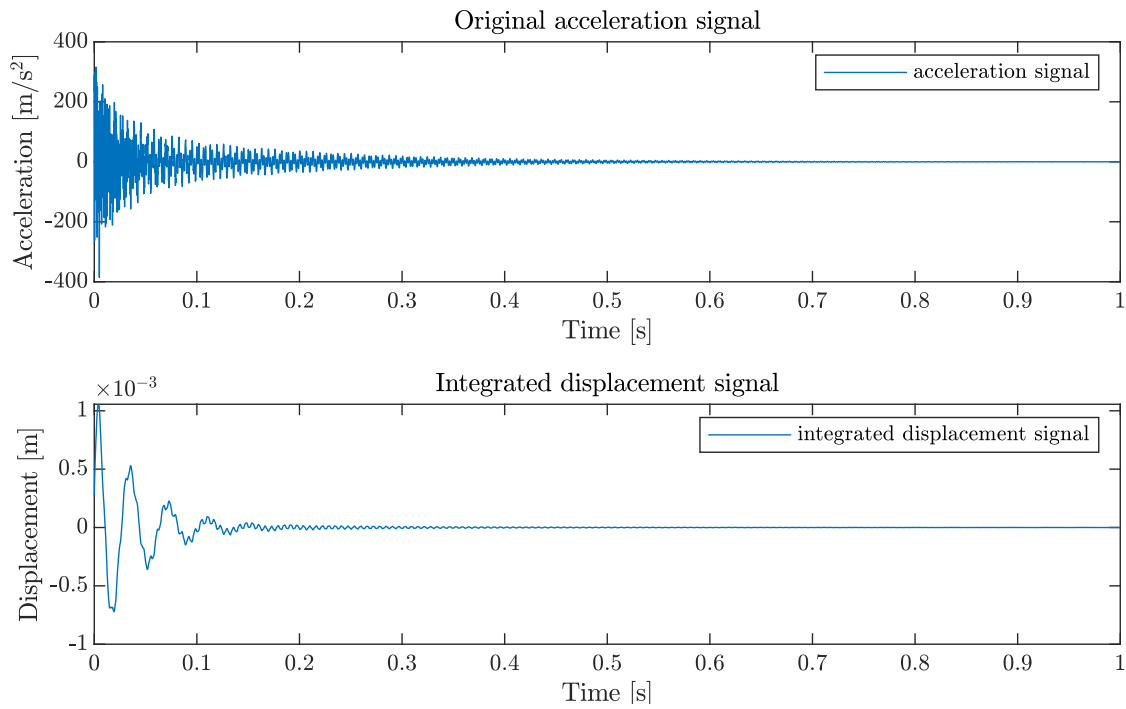


**Figure 4.1:** Integration of acceleration to displacement signal

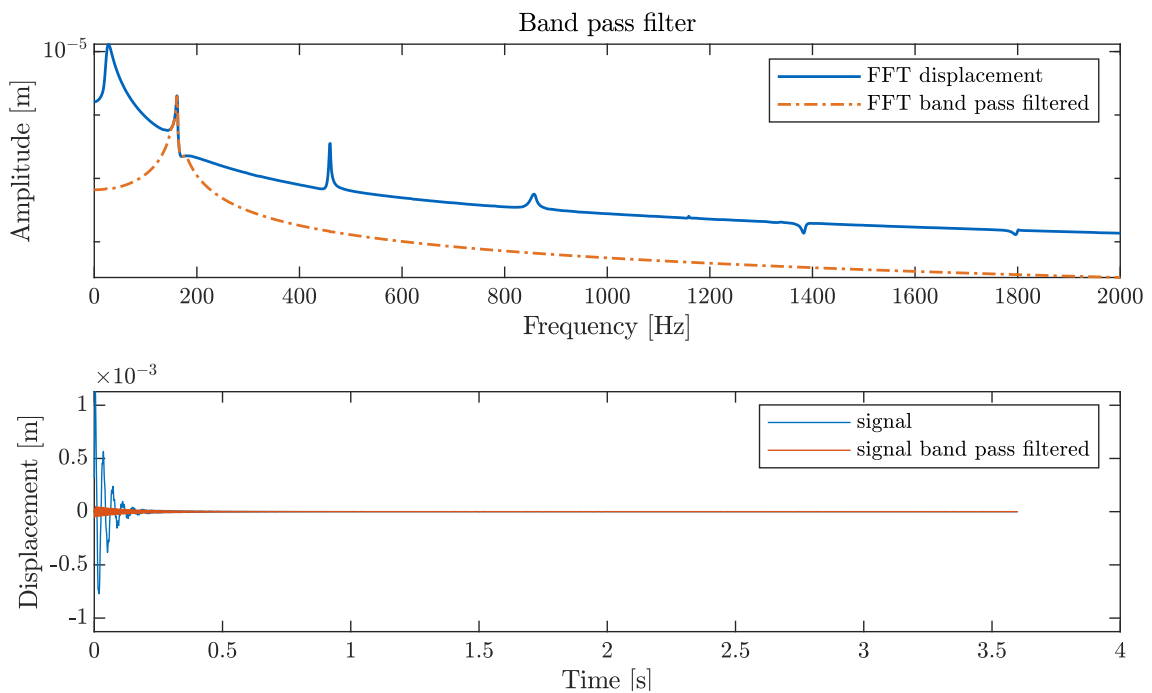


**Figure 4.2:** Band pass filtering of the displacement signal

superimpose and it seems like different forces activate the joint in different manner. Thus, different forces provoke variations of the observed non-linear behavior.

The repeatability of the modal ID using HT is discussed with the help of Figure 4.7. It contains the results of the non-linear tests in campaign 2, 3 and 4 with an impact force of 100 N. The torque level on the other hand was incrementally increased for every campaign. Between the campaigns the bolt is loosened in order to start again with a torque level of

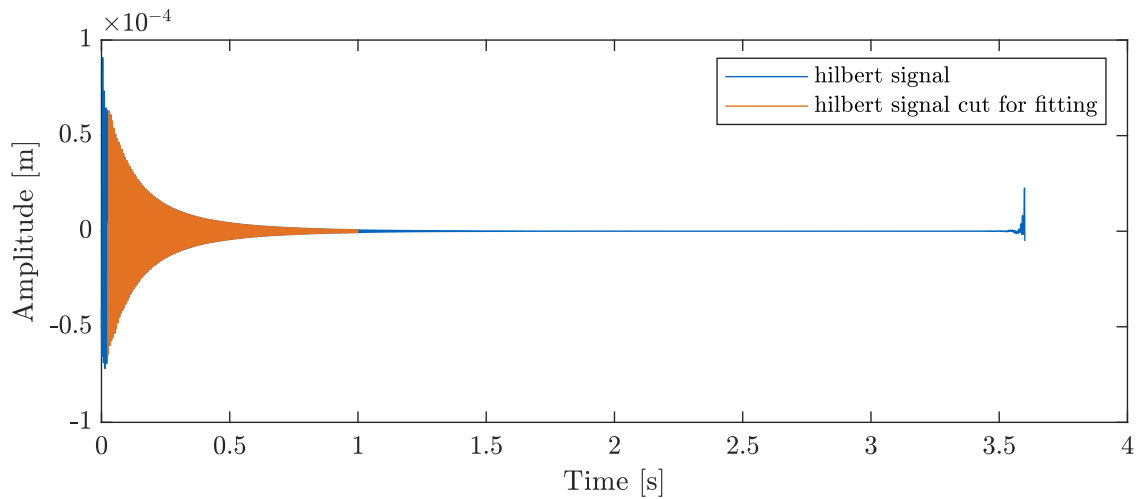


**Figure 4.3:** Time interval for the polynomial fit

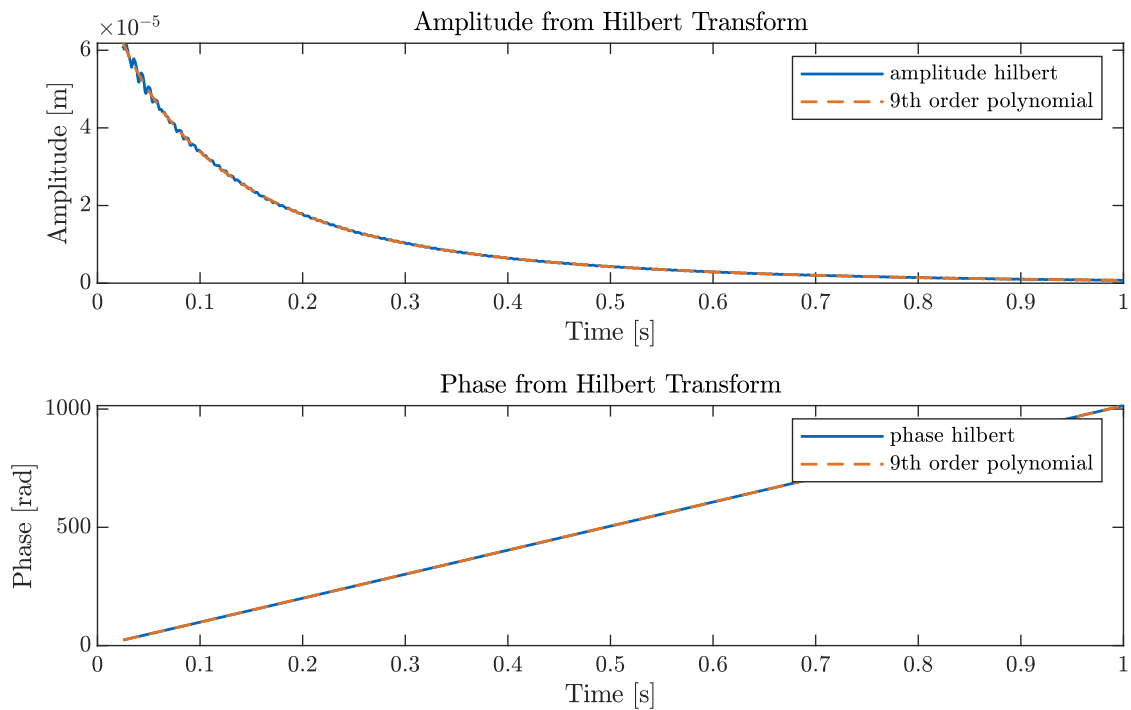


**Figure 4.4:** Polynomial fit of the analytical Hilbert signal

5 N m and go up to 50 N m.

The trend of the results is consistent: from 5 N m up to 20 N m one can observe a consistent increase of the stiffness. From 20 N m to 50 N m however, the stiffness remains on the same level. The damping stays in the same range for all torque levels except for one outlier at 5 N m. This outlier is assumed to be coincidence and triggered by irregularities in the measurements. It seems that, although a large uncertainty, the damping with a torque level of 5 N m is generally bigger than the damping for the remaining torque level, which are similar. This is consistent to the frequency variation.

Another obvious observation is that the repeatability is lower for low torque levels and increases with higher torque levels, as expected.

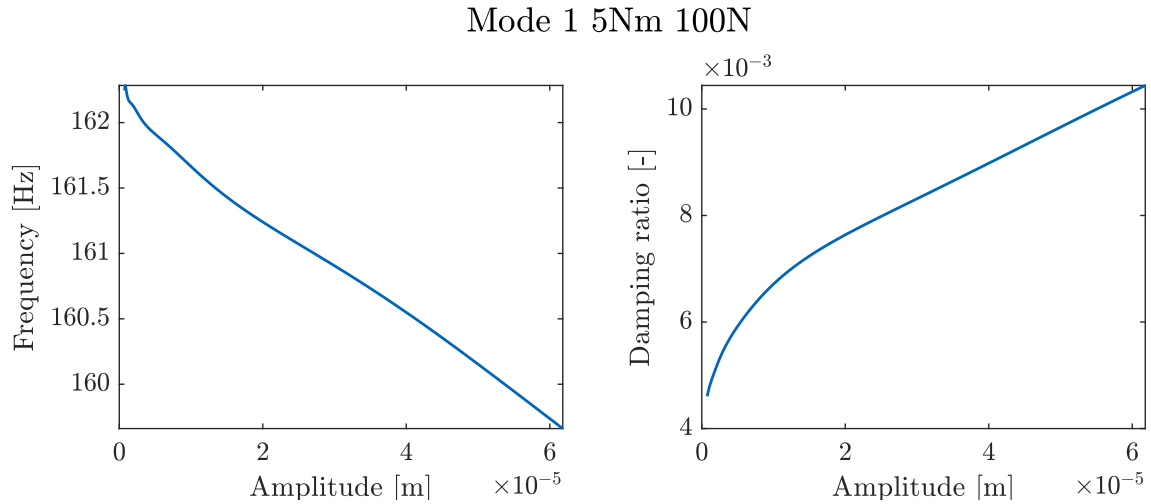


**Figure 4.5:** Backbone and damping curve

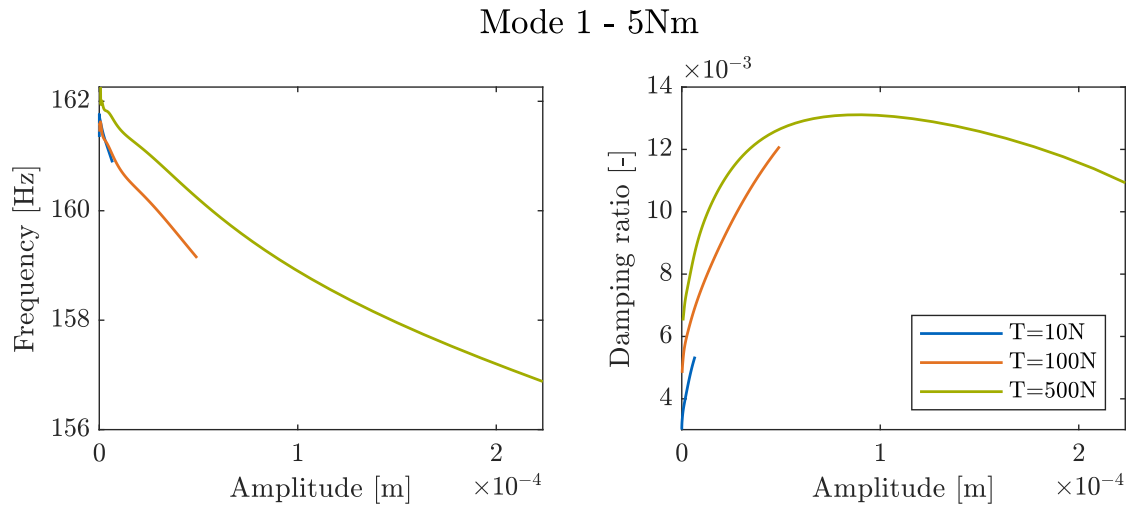


**Figure 4.6:** Frequency and damping curve for different impact forces

Finally, the influence of the torque level is discussed in more detail by only considering campaign 2. Thereby, the results for mode 1 as well as mode two are regarded.

Again, the backbone curves in Figure 4.8 show an increase in the frequency from 5 Nm to 20 Nm. The backbone curves for 20 Nm and 50 Nm are on the same level and the frequency peaks of the corresponding FRFs overlap.

A trend can also be seen in the gradient of the backbone curves: the slope of the blue (5 Nm) curve is the highest and flattens with increasing torque level. A large slope of the backbone curve suggests high non-linearities. The flatter the curve, the less non-linearities are present in the system.

The frequency dependent curves of the HT show the same effects as for mode 1 (Figure 4.9): Increased frequency and less non-linearities for an increasing torque level except for 50 Nm. The damping is high for 5 Nm and on the same level from 10 Nm to 50 Nm.

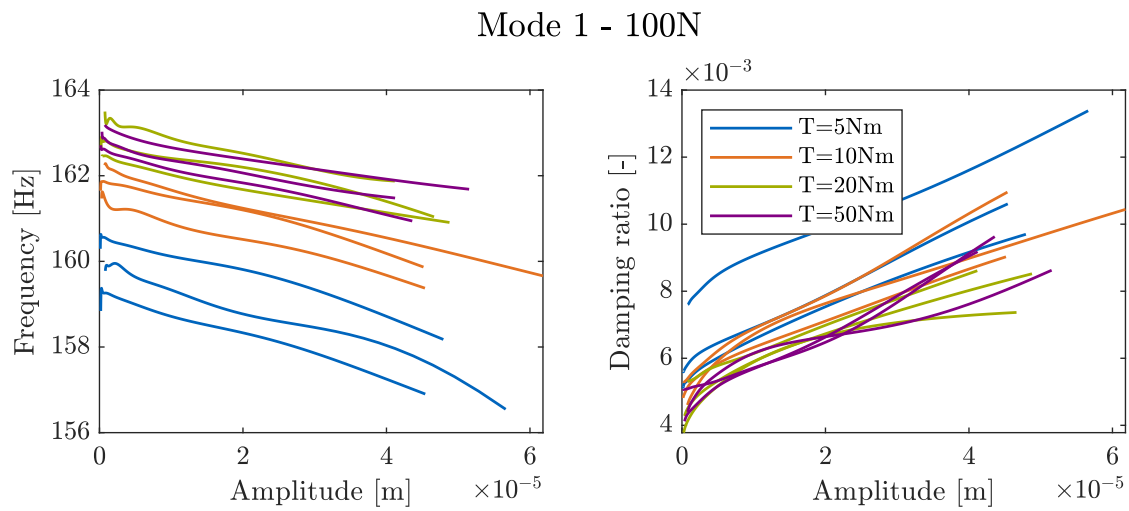


**Figure 4.7:** Frequency and damping curves for the entire campaign 1

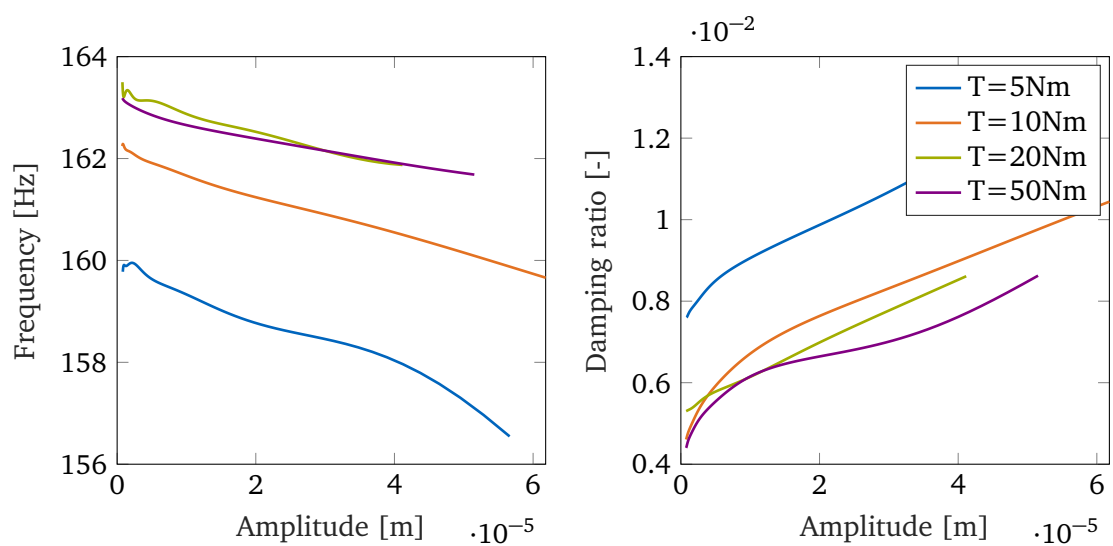


**Figure 4.8:** Backbone and damping curves for mode 1 for different torque levels

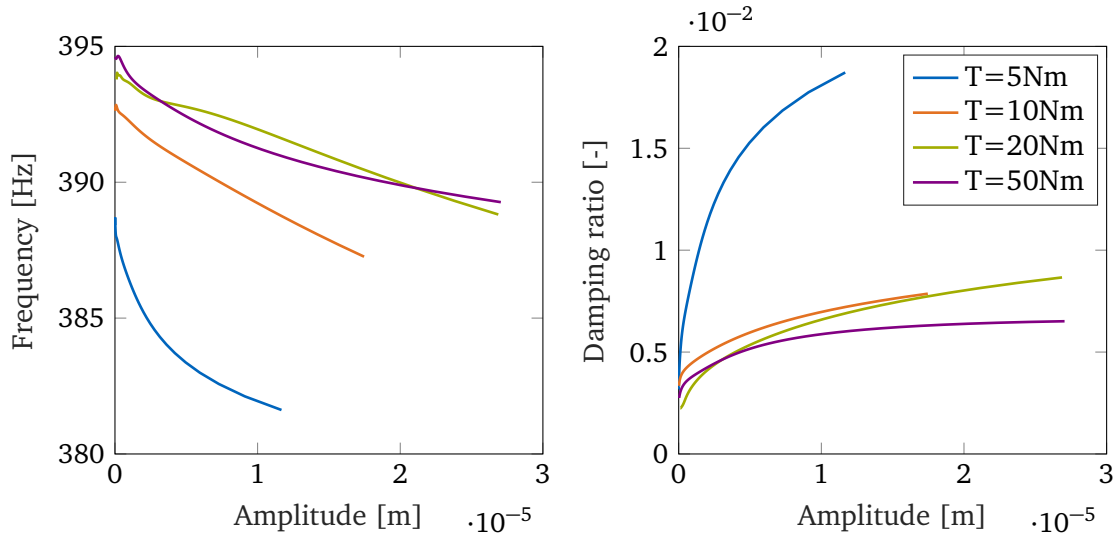


Figure 4.9: Backbone and damping curves for mode 2 for different torque levels

## 4.2 Investigation of Frequency Based Substructuring

The FBS joint ID consists of decoupling the assembled measurements and coupling the identified joint with the separately measured parts. The motivation in using FBS lies in the fact that it is a very simple approach and easy to implement. The used test structure (section 3.4), however, was originally developed to study non-linear joint ID methods and is not well suited for the application of FBS. The difficulty in using FBS for this structure is that the flexibility of the joint is much lower than flexibility of the two parts, as the analysis will show. This leads to the fact that the joint's dynamics are covered by the dynamics of the two beams. Furthermore, the inherently large and flexible interface. This contradicts the prerequisite of a rigid interface for the VPT. In addition, the focus in the evaluation is on the analysis of the first two bending modes. The bending of these modes, however, affects the joint (Figure 3.4) and the requirement of a rigid interface is missed even more. Extracting the joint's stiffness becomes very difficult. Hence, in addition to the evaluation of the FBS results, it is investigated to what extent FBS can be applied to the used test structure and where its limits are (subsection 4.4.1).

Inverse substructuring is used since it allows to isolate the joint's dynamics very easily and thus, further simplifies joint ID. However, it is limited to systems with a mass-less joint and no cross coupling. Nevertheless, the advantage of the simple joint isolation outweighs and for the following evaluation the requirements of a mass-less joint and no cross coupling are assumed to be valid. The extent to which the conditions are fulfilled and how they affect the results will be discussed in subsection 4.4.1.

The evaluation of FBS is structured as follows: first, the quality of the measurements is discussed before evaluating the joint isolation (integration and inversion) and parameterization. Subsequently, the coupling process is analyzed and a first evaluation of the applicability of FBS is made before the joint ID with FBS is assessed using the results of HT. Finally, the assumptions made for inverse substructuring are reviewed.

Starting point are the measured FRFs  $Y_{uf}^{AJB}$ . Unless otherwise stated, the evaluation is presented using the results of test run 'C2-50 N m-LIN'. Thereby, it was ensured that the results of

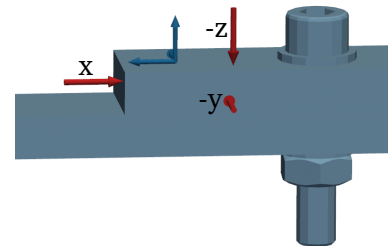


this test run comply with the remaining tests. If this is not the case, other test runs are considered and differences discussed. Note that for the evaluation only interface impacts/channels are regarded.

First, a filter is applied in order to eliminate noise. The difference between the joint parameterizations with filtered and an unfiltered FRFs can be seen in Figure 4.17 and Figure 4.18.

#### 4.2.1 Quality of the Measurements for Frequency Based Substructuring

Passivity, consistency, and reciprocity allow to validate the quality of measured data. The passivity is shown for three driving points (one in each direction) in the original acceleration data  $Y_{uf}^{AJB}$ . Thereby, the input and output of each driving point are not at the exact same position but the impact is as close as possible to the corresponding output. The impacts (red) and channels (blue) are depicted in the graphic to the right, whereas the output channels correspond to the same sensor.



The phase of all three driving points is shown in Figure 4.10.

Note that for directions  $x$  and  $z$  the negative phase is depicted, since impact and channel directions are opposite. In case of a good passivity, the phase is between  $0^\circ$  and  $180^\circ$  for acceleration FRFs. This is not the case for all three directions and indicates that something went wrong during the measurements. However, it is noticeable that the phase is mainly between  $0^\circ$  and  $-180^\circ$ . One explanation for this is that some irregularities occur at the beginning of a measurement and cause a shift of the phase. Afterwards, the passivity is consistent but with a shifted phase between  $0^\circ$  and  $-180^\circ$  instead of  $0^\circ$  and  $180^\circ$ .

A bad passivity impedes the modal analysis and adversely affects the damping. Therefore, it is not possible to conduct a reliable modal analysis within this thesis. The negative impact on the damping did not affect the proceeding, since it is neglected due to noise.

Consistency allows to validate the measurement setup and VPT. Figure 4.11 shows the specific impact consistencies of all measurements on the assembly AJB (for all torque levels) using a box plot<sup>1</sup>. A separate presentation of the specific impact consistencies per torque level is omitted, as there is no significant difference. Meaning that the torque level has no further influence on the impact consistency.

For both parts, the following applies: impacts 1-4 are in  $\pm z$ -direction (Figure 4.12a), 5-9 in  $\pm y$ -direction (Figure 4.12b) and 10 and 11 in  $\pm x$ -direction (Figure 4.12c) on the respective part. It is noticeable that the impacts in  $\pm y$ -direction have a generally worse consistency than the remaining impacts.

The overall impact consistency depending on the frequency is pictured in Figure 4.13. The sections in the lower part of the graph show the zoomed in consistency around the eigenfrequencies of the two bending modes (mode 1 and 2). Individual outliers with worse consistency can be identified, e.g., Test 'C1-5 N m-LIN3' for part A as well as 'C1-5 N m-LIN1' and 'C1-20 N m-LIN2' for part B. However, on the whole, the consistency is sufficient, especially at the frequencies of mode 1 and mode 2.

<sup>1</sup>**Box lower border:** lower quartile (25% of the data points fall below the lower quartile value); **Median:** the median marks the mid-point of the data (line that divides the box into two parts). Half the data points are greater, and half are less than the median; **Box upper border:** upper quartile (75% of the data points fall below the upper quartile value); **circle 'o':** outliers

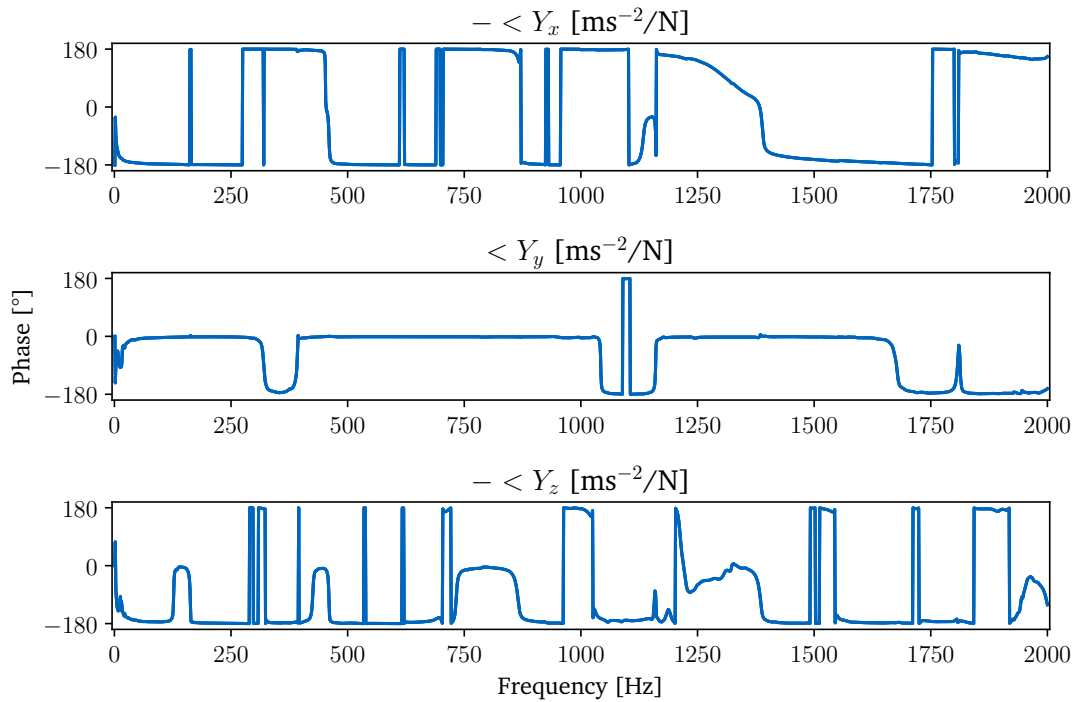


**Figure 4.10:** Phase of driving points in x-, y-, and z-direction

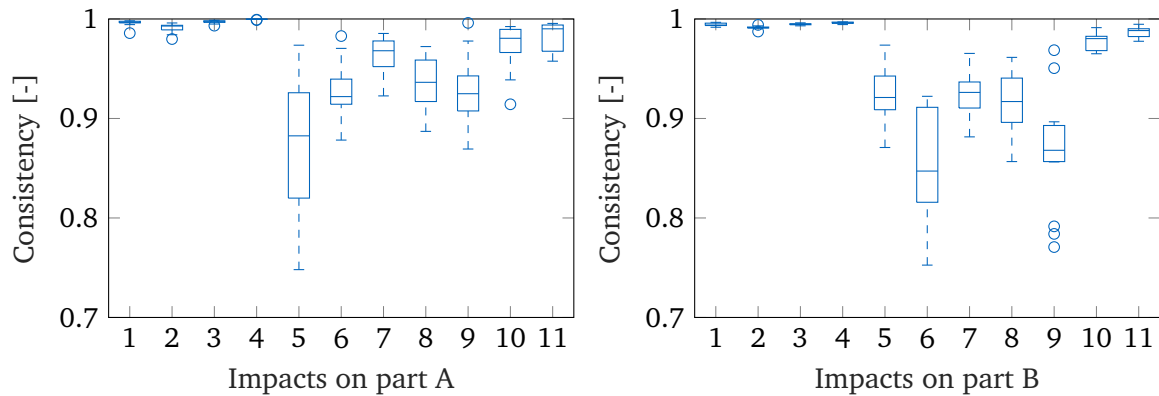


**Figure 4.11:** Specific impact consistency of all linear measurements on AJB for impacts on part A and B

The specific channel consistencies of all channels are depicted in Figure 4.14. Again, a separate presentation for each torque level is omitted. However, it is to mention that the outliers with lower consistencies (for all channels) originate from tests with a torque level of 5 N m. For the remaining torque levels, no significant difference or trend regarding the channel consistencies exists. The overall channel consistencies depicted in Figure 4.15 are very good and close to one for all frequencies.

The consistency check is also carried out for the measurements of the separated (mechanically disassembled) parts A and B. The results are slightly better than those of the assembled measurements: the specific impact consistencies are within the bounds from 0.85 to 1 and the specific channel consistencies between 0.95 and 1. The overall consistencies for impacts as well as for channels are close to one for all frequencies. A more detailed presentation is omitted.

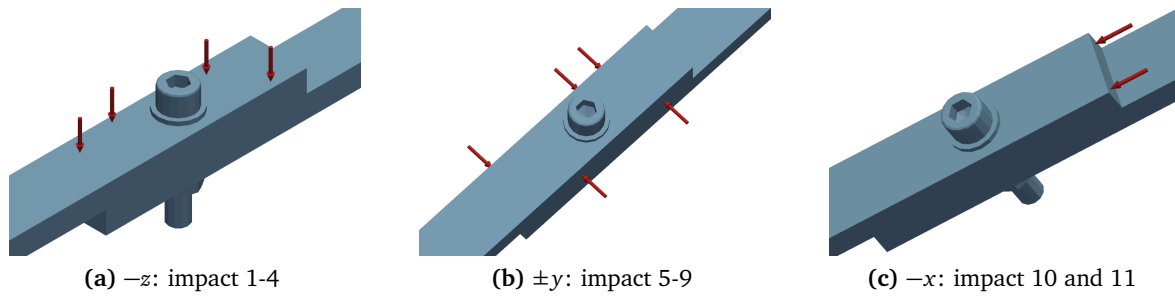
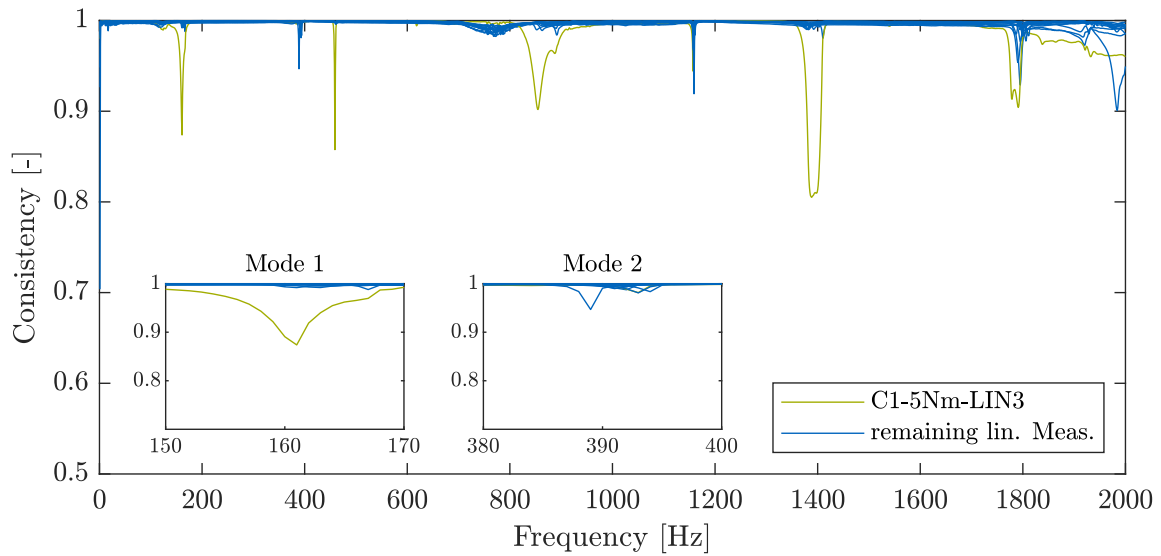
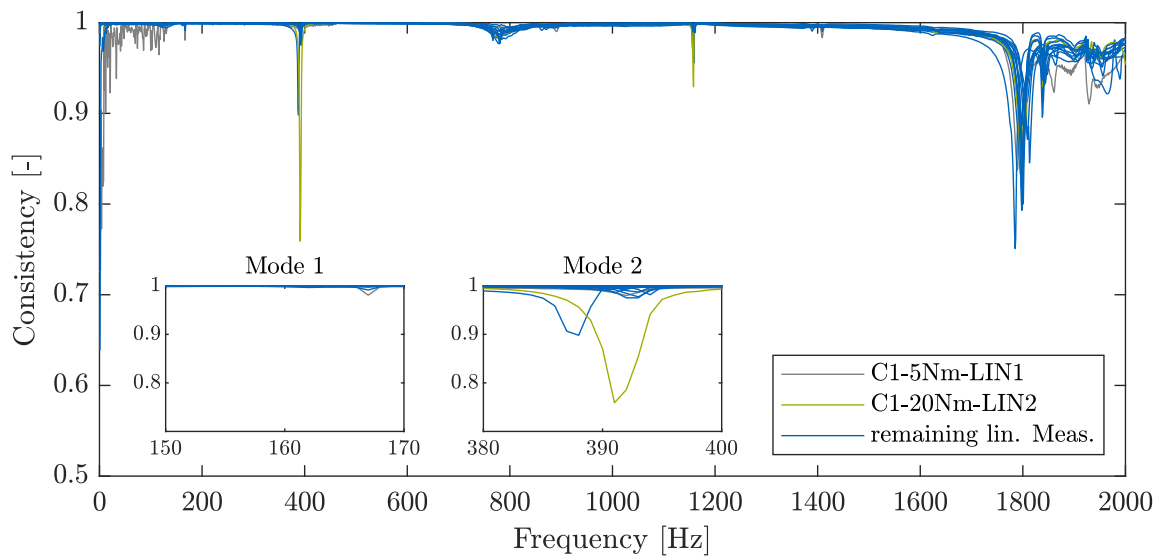


Figure 4.12: Impact 1-11 on part A



(a) Overall impact consistency part A



(b) Overall impact consistency part B

Figure 4.13: Overall impact consistency of all linear measurements on AJB for impacts on part A and B including enlarged sections at the frequency of mode 1 and 2

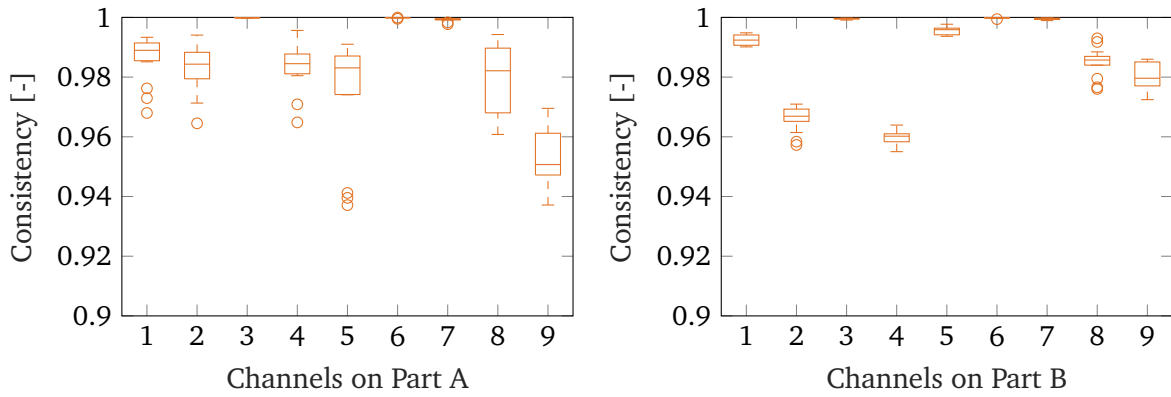
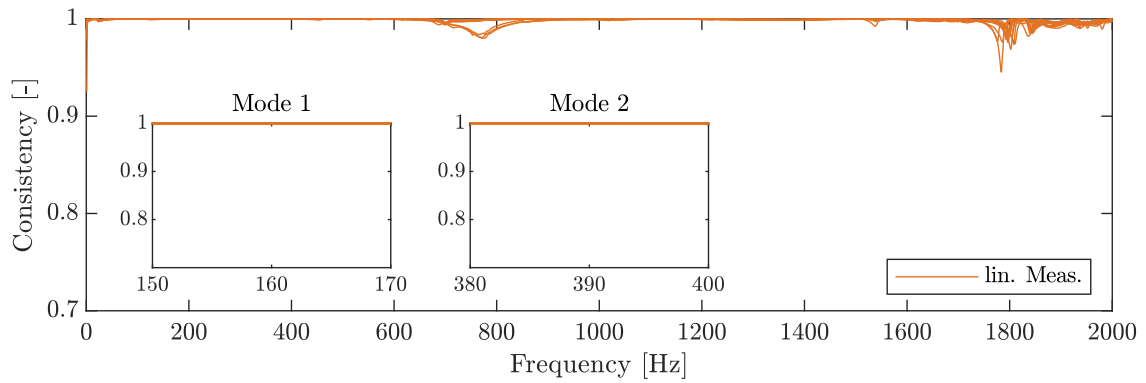
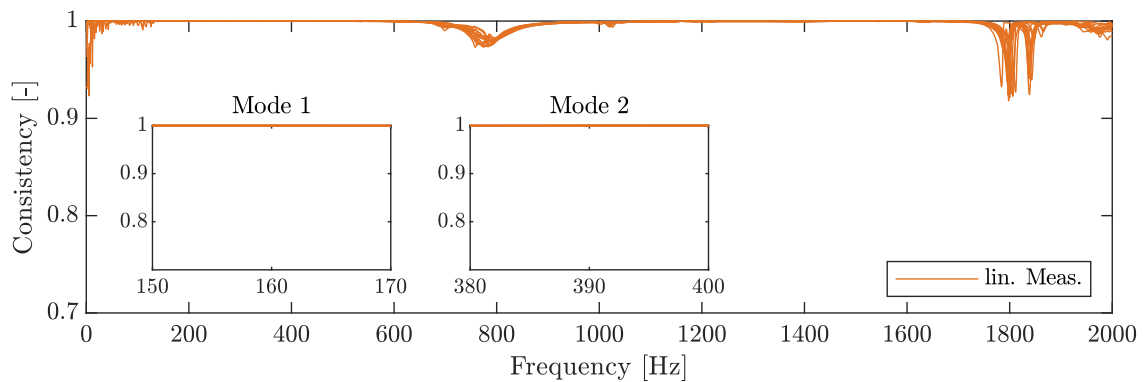


**Figure 4.14:** Specific channel consistency of all linear measurements on AJB for channels part A and B



**(a)** Overall channel consistency part A



**(b)** Overall channel consistency part B

**Figure 4.15:** Overall channel consistency of all linear measurements on AJB for channels on part A and B including enlarged sections at the frequency of mode 1 and 2

To get an impression of the measurements' reciprocity, Figure 4.16 shows opposing FRFs of  $Y_{qm}^{AJB}$ . The figure on the right depicts the shape of  $Y_{qm}^{AJB}$  and marks the shown FRFs. For reasons of clarity this figure will appear throughout the evaluation and mark the currently shown entries of the considered matrix. The gray squares mark the diagonal for orientation purposes.

As can be seen in Figure 4.16, the reciprocity varies depending on the depicted input and output. For  $Y_{qm}^{AJB}(1,4)/Y_{qm}^{AJB}(4,1)$ , e.g., the modes and the respective amplitudes match quite good, whereas for  $Y_{qm}^{AJB}(2,3)/Y_{qm}^{AJB}(3,2)$  and  $Y_{qm}^{AJB}(2,4)/Y_{qm}^{AJB}(4,2)$  the amplitudes differ for modes in the higher frequency range. Altogether, the reciprocity is sufficient, especially for the bending modes of interest (mode 1 and mode 2). Reciprocity is considered again in the parameterization of the stiffness in subsection 4.2.2. There, the influence of possibly poor reciprocity is reduced for at least the joint parameterization.

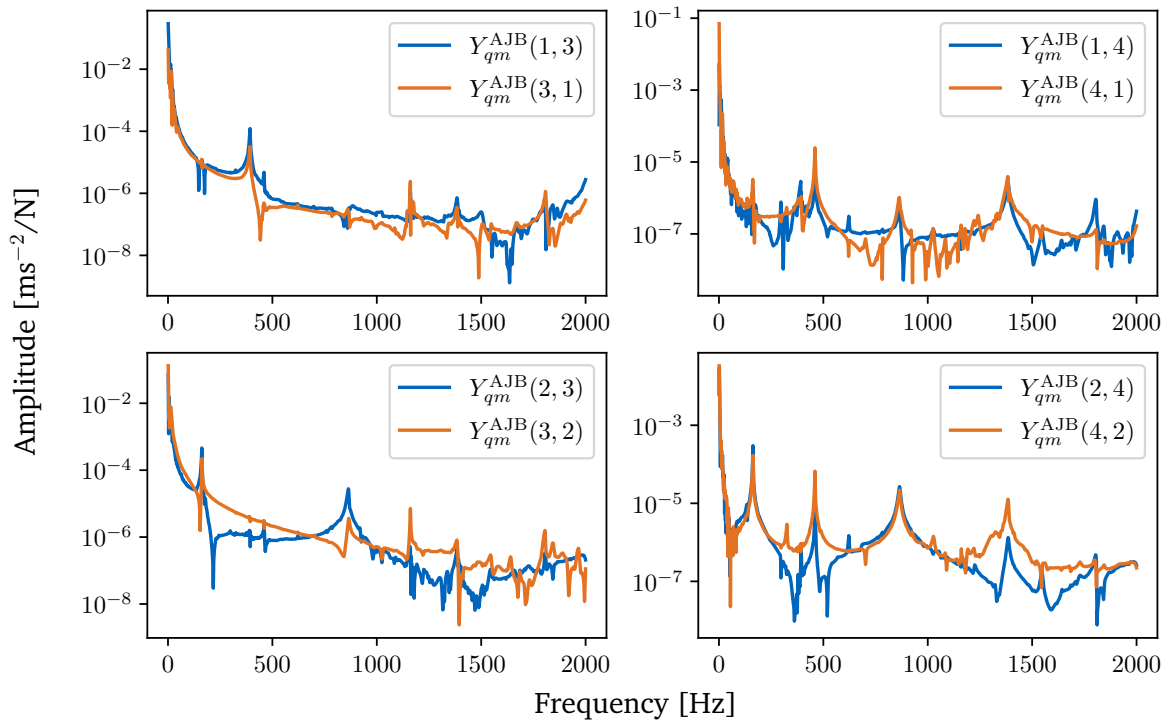
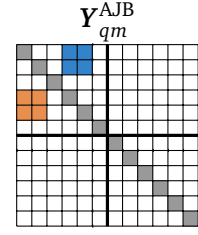
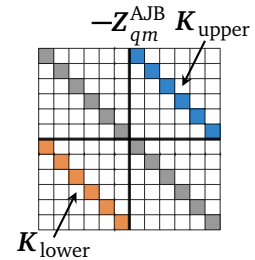


Figure 4.16: Opposing FRFs of  $Y_{qm}^{AJB}$  to evaluate reciprocity

#### 4.2.2 Isolation and Parameterization of the Joint

After applying the VPT and the quality check of the measurements, the data is integrated twice in order to receive the receptance matrix. Next, the receptance matrix is inverted in order to receive the dynamic stiffness matrix and isolate the joint.

As can be seen in the illustration to the right, the diagonal elements of the  $6 \times 6$  off-diagonal sections in the negative dynamic stiffness matrix  $-Z_{qm}^{AJB}$  contain the joint's stiffness. This corresponds to the description in subsection 3.2.2. The result of the parameterization of the upper right section will be called  $K_{upper}$  and the one of the lower left section



$K_{\text{lower}}$ . The parameterization process is the same for  $K_{\text{upper}}$  and  $K_{\text{lower}}$ : for each dynamic stiffness curve to parameterize, a frequency range is selected in which the curve approaches a constant line. The green curves in Figure 4.17 outline the range selected for each stiffness curve. Thereby, the quality of the curve segments differs. Whereas the curves of  $k_x$ ,  $k_y$ ,  $k_{rx}$ , and  $k_{rz}$  show explicit sections with nearly constant behavior, no clear segment can be identified for the curves of  $k_z$  and  $k_{ry}$ . This means that the stiffnesses  $k_z$  and  $k_{ry}$  cannot be well observed with the chosen measurement setup.

Figure 4.18 shows the parameterization of unfiltered data. Comparing the identified values for the stiffness, it is noticeable that they mostly match for the good observable values. For the less observable values, however, there are deviations.

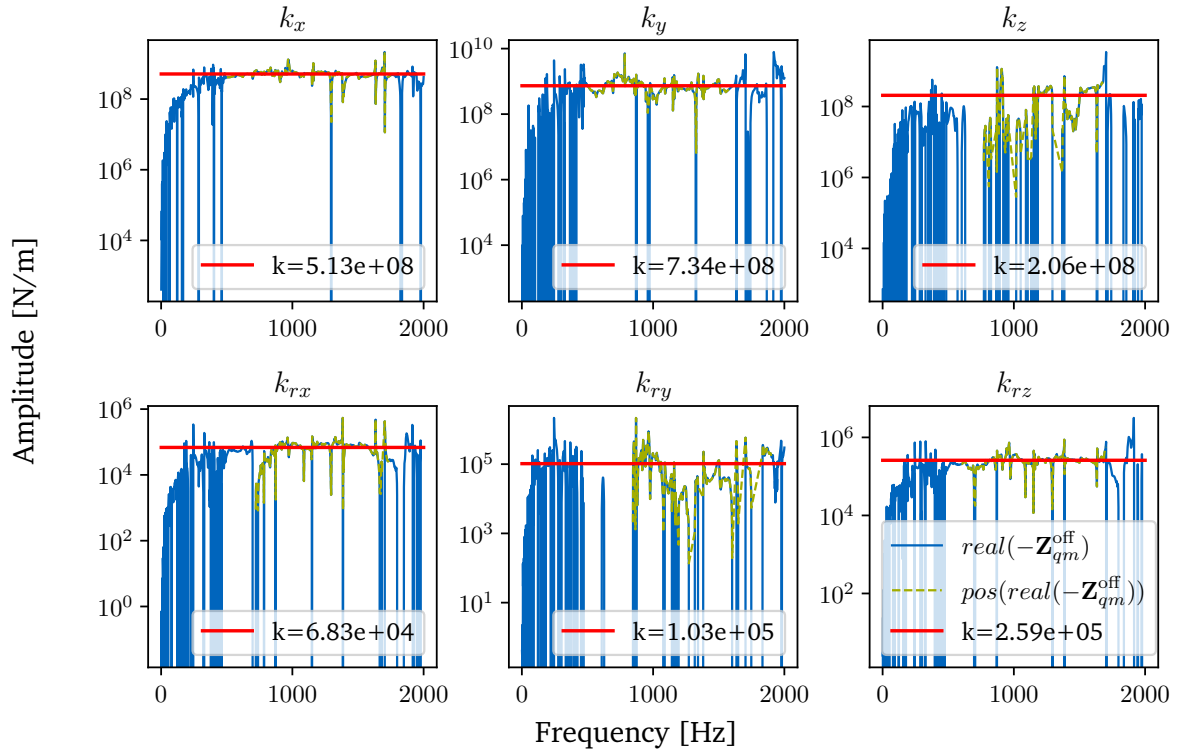


Figure 4.17: Parameterization of the joint with filtered data

In order to reduce the negative effect of a bad observability and nevertheless achieve a good approximation of the stiffness, two measures are taken: First, only positive values of the regarded dynamic stiffness curve are considered for the curve fitting of  $k$ . This prevents outliers with negative amplitudes from distorting the result by shifting the identified stiffness parameter to lower values. The green curve in Figure 4.17 depicts the (positive) data used for the curve fitting.

In addition, the calculation of the stiffness is improved by using the average of  $K_{\text{upper}}$  and  $K_{\text{lower}}$  for the parameterized stiffness  $K$ :

$$k_i = (k_{\text{upper},i} + k_{\text{lower},i})/2 \quad i = [x, y, z, rx, ry, rz] \quad (4.1)$$

$K_{\text{upper}}$  and  $K_{\text{lower}}$  are compared in Figure 4.19. It can be seen that the difference of upper and lower values is small. This suggests that the reciprocity of the regarded measurements is good or at least good enough to ensure a reliable joint parameterization. Using the mean value stabilizes the parameterization result and reduces the negative influence of a bad reciprocity.

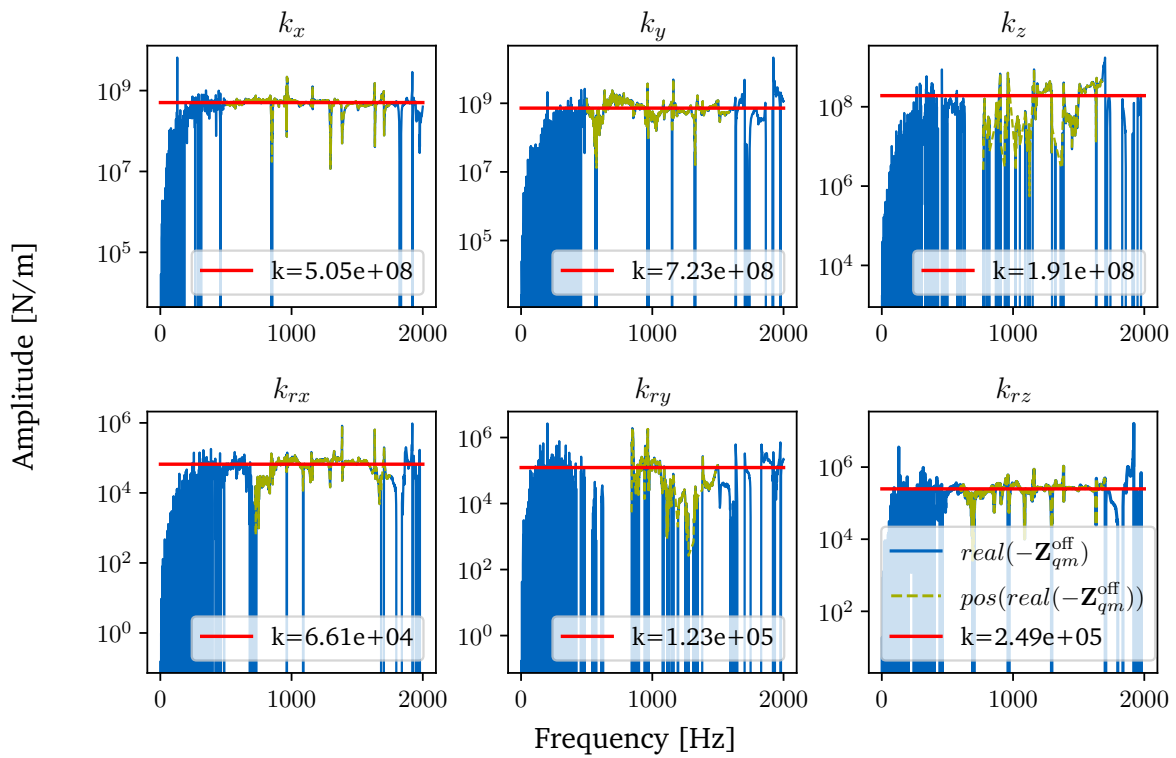


Figure 4.18: Parameterization of the joint with unfiltered data

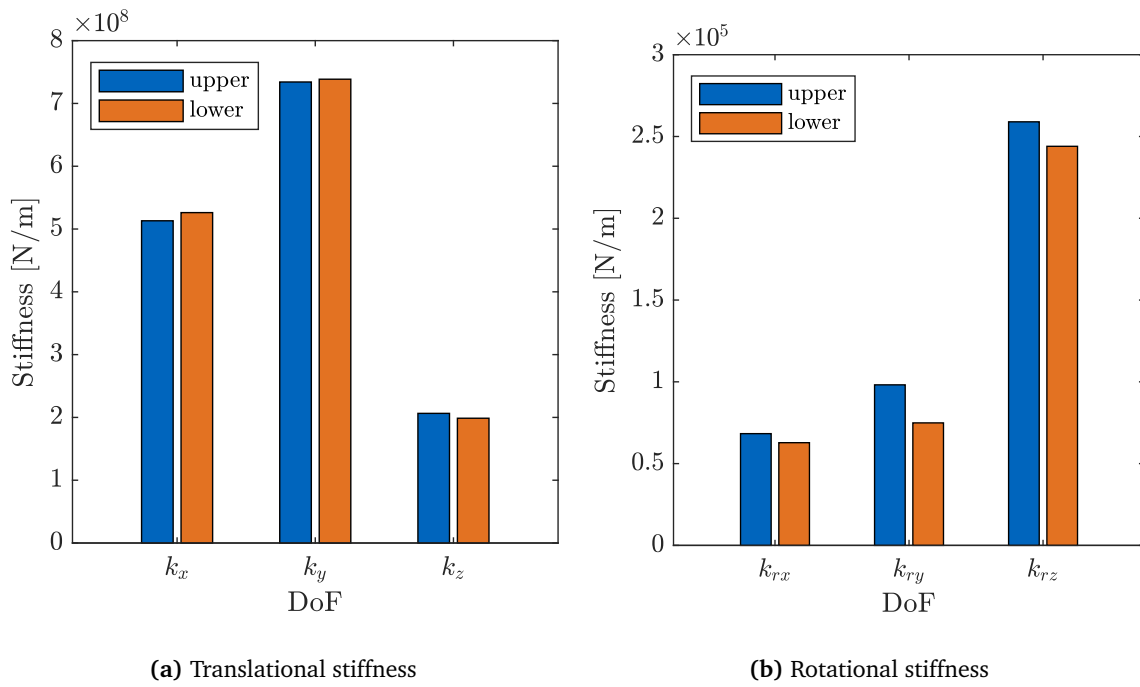


Figure 4.19: Comparison of  $K_{upper}$  and  $K_{lower}$

### Repeatability and Sensitivity

For the evaluation of the linear joint ID, it is also necessary to assess the repeatability and sensitivity of the joint parameterization regarding different contact parameters. Repeatability evaluates the extent to which results of measurements within the same DOE coincide. The sensitivity of the ID regarding different contact parameters describes how much the results change when changing, e.g., the torque level.

Figure 4.20 shows the ranges of the identified stiffness values depending on the torque level. It includes all linear measurements: four measurement runs and therefore four different identified stiffnesses per torque level, except for 10Nm with three repetitions. The ranges, where the identified values lie, are relatively small except for  $k_{r,y}$ . Meaning that the repeatability of the parameterization of all values except  $k_{r,y}$  is good. The fact that the ranges of the identified stiffness values for  $k_{r,y}$  are large is probably caused by its bad observability as discussed previously. However, it is surprising that the ranges for the identified  $k_z$  are small, since the value is also poorly observable. It must be noted, however, that this range probably depends on the choice of frequency range for the fitting and might be higher for different frequency ranges.

Considering the differences between the torque levels, for  $k_x$ ,  $k_y$ ,  $k_{r,x}$ , and  $k_{r,z}$  a consistent increase of stiffness occurs when increasing the torque level. For  $k_z$  and  $k_{r,y}$ , however, the error made in the parameterization due to bad observability seems to be bigger than the difference in stiffness for changing torque levels. As a consequence, no tendency depending on the torque level can be detected for these two values.

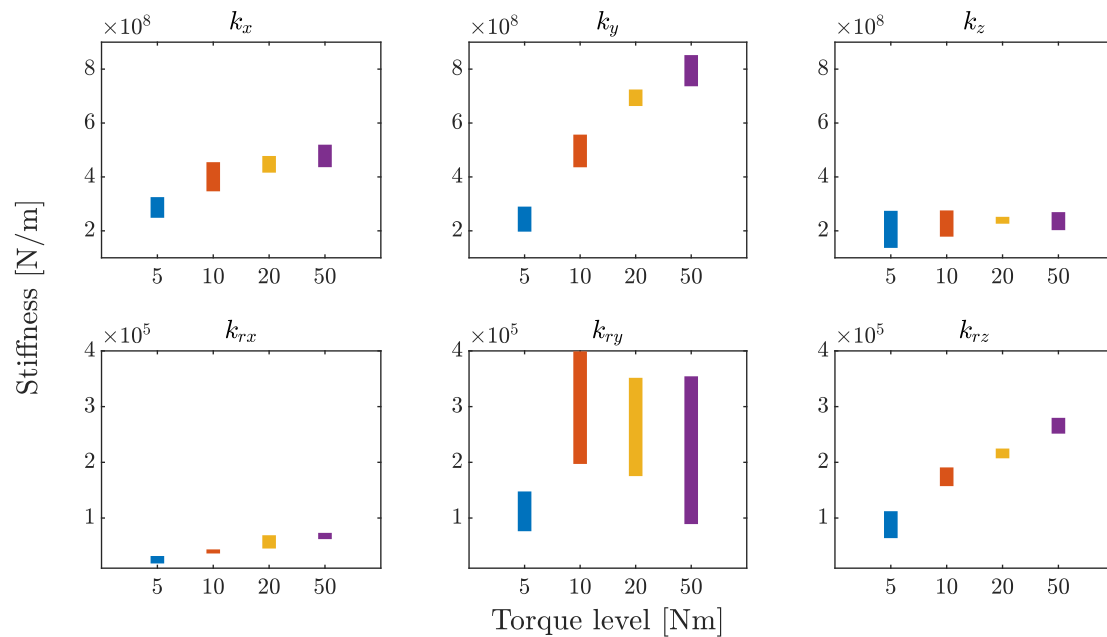


**Figure 4.20:** Range of stiffness values depending on the torque levels of all linear measurements

To give a better impression, the parameterized values are shown separately in Figure 4.21. The values marked along a solid line belong to one test run. The figure clearly shows that the translational stiffness values are much higher than the rotational values (logarithmic y-axis). This corresponds to the generally expected behavior.



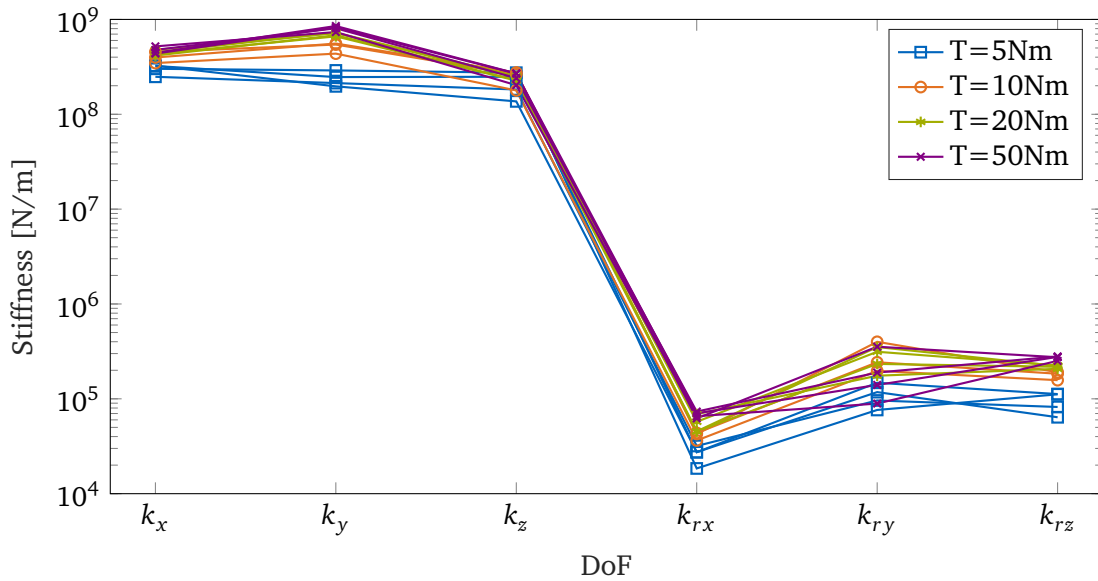


Figure 4.21: Parameterized  $K$  for all torque levels of all linear measurements

Maximum Parameterization Error

To estimate the error that can be made in the parameterization, Figure 4.22 pictures the ranges of  $K_{upper}$  and  $K_{lower}$  (and not of the average  $K$  as in Figure 4.20). This should give an idea about the maximum possible error that can be made during the parameterization. E.g., it is of interest if the possible error is larger than the sensitivity to different torque levels. Here, the same statement can be made as with the average of  $K_{upper}$  and  $K_{lower}$ . Meaning that for  $k_x, k_y, k_{rx}, k_{rz}$ , and slightly  $k_z$  a higher value is identified when increasing the torque level. However, it is noticeable, that the ranges for 5 N m and 10 N m overlap except for  $k_{rx}$ . For  $k_{ry}$  no tendency can be observed.

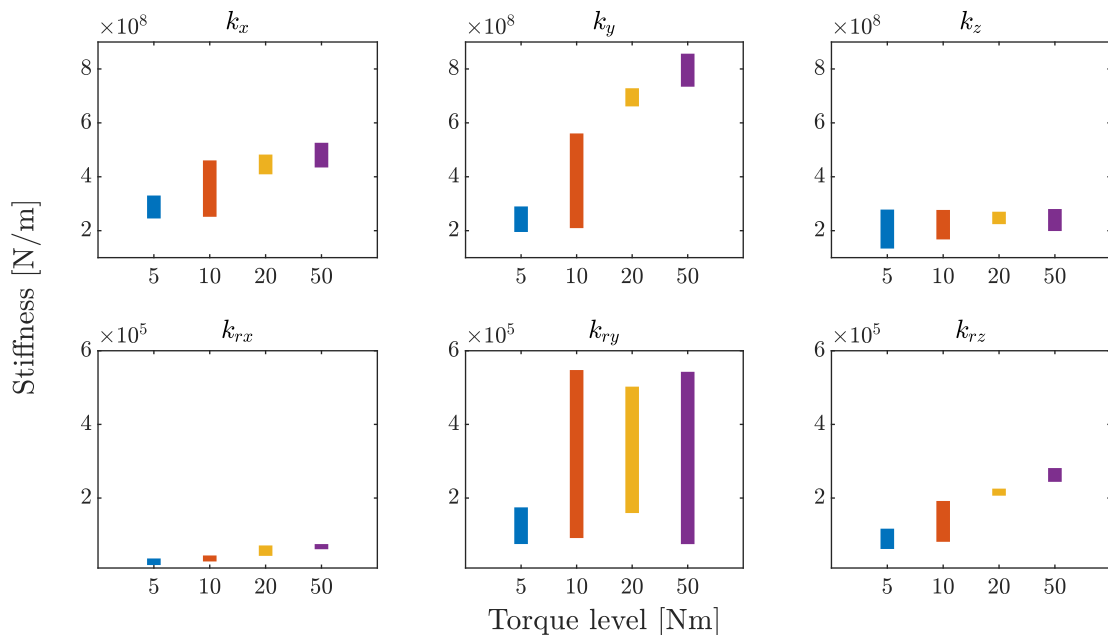


Figure 4.22: Maximum error done by the parameterization depending on the torque levels of all linear measurements

To sum up, the joint parameterization shows a good repeatability except for the ID of  $k_{ry}$ . Regarding the sensitivity to different torque levels, a clear tendency can be observed for  $k_x$ ,  $k_y$ ,  $k_{rx}$ ,  $k_{rz}$ , and slightly for  $k_z$ , but not for  $k_{ry}$ . The effect of the repeatability and sensitivity on the quality of the coupled result is discussed in section 4.3 and section 4.4.

### 4.2.3 Verification with Big Sensors

To ensure that the sensors do not falsify the result due to defective properties, the joint analysis is verified by another set of sensors (big sensors) for the torque level 10 Nm. The big sensors are less affected by noise and filtering at the beginning of FBS is not required. Thus, if the results would be similar, we could exclude that the filter causes an erroneous joint ID. The parameterization of the data measured with big sensors is pictured in Figure 4.23 and shows similar effects as the measurements with small sensors: for  $k_x$ ,  $k_y$ , and  $k_{rz}$  clear stiffness lines can be identified. The quality of these constant lines is slightly better than with small sensors even without using a filter for noise reduction. Where quality depicts how well the values approximate a straight line without outliers or noise. However, for this case, not only the observability of  $k_z$  and  $k_{ry}$  is bad but also of  $k_{rx}$ . This affects the identified value for  $k_{rx}$  as shown in Figure 4.23. The estimated value is lower than the values identified with small sensors for all torque levels. In addition, the value for  $k_z$  is higher than the values estimated from measurements with small sensors.

The identified values for  $k_x$ ,  $k_y$ ,  $k_{ry}$ , and  $k_{rz}$ , in contrast, are in the range between the stiffness values for 5 Nm and 20 Nm identified when using the small sensors. This also corresponds to the range in which the stiffness values lie with 10 Nm for small sensors. Overall, it can be said that the identified stiffness values of small and large sensors coincide and the application of the small sensors entails no fundamental errors. The small sensors are used, since they are lighter and add less mass to the system.

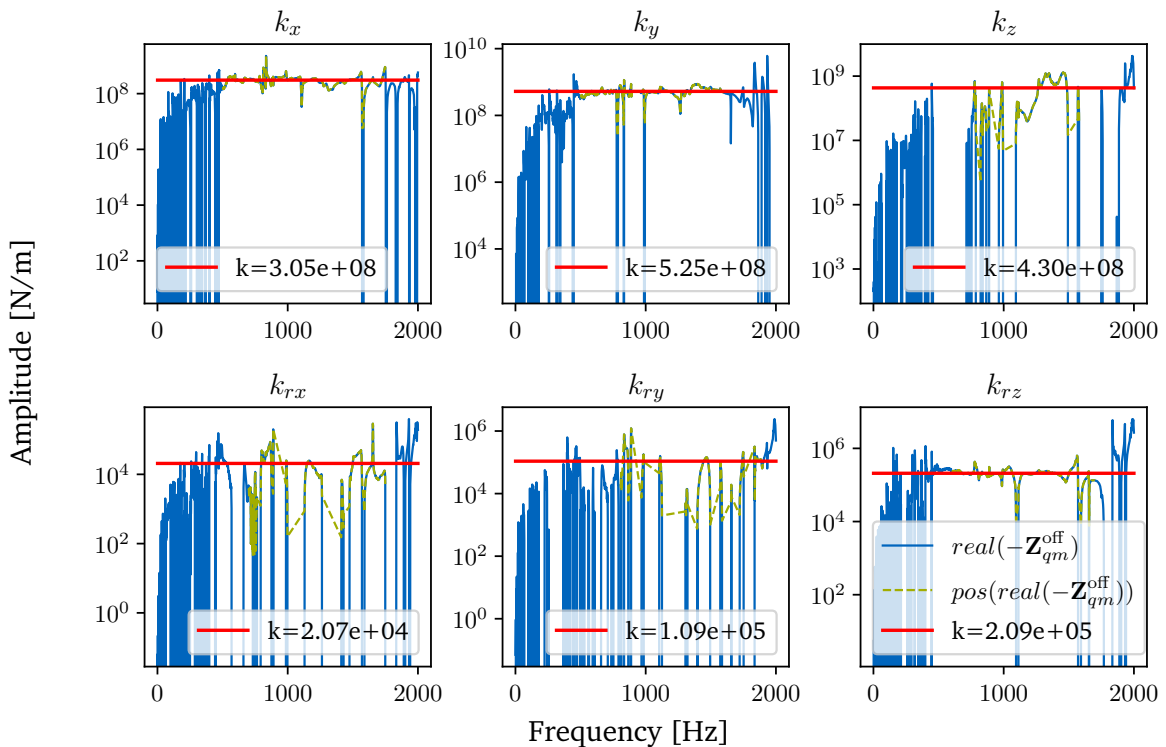


Figure 4.23: Parameterization of the joint for measurements with big sensors

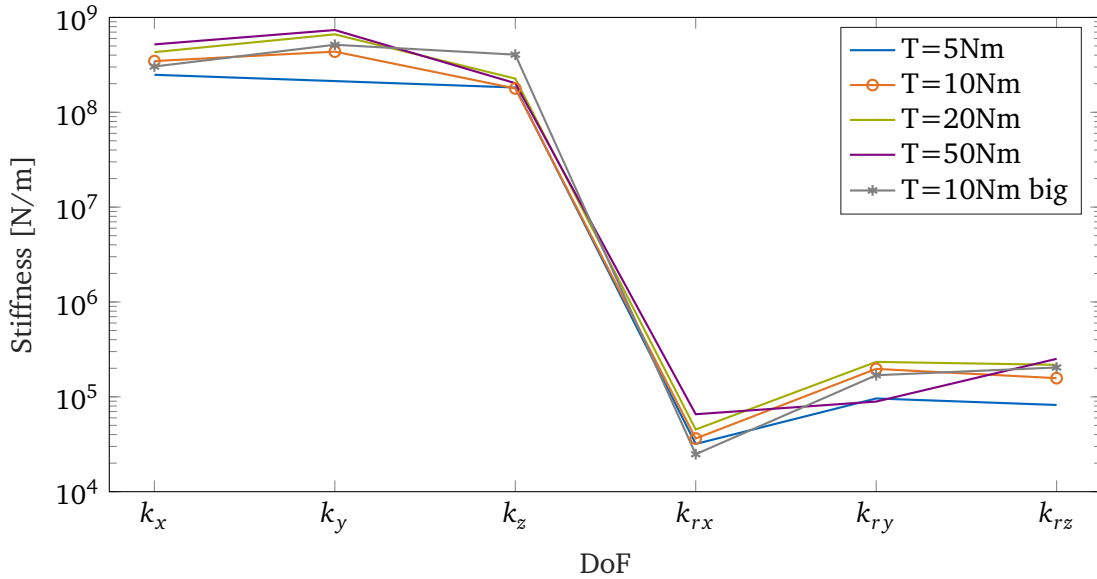
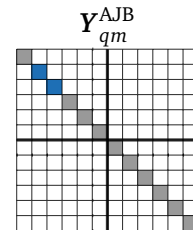


Figure 4.24: Parameterized stiffness with small vs. big sensors

### 4.3 Investigation of the Coupling Results

Before discussing, inter alia, the influence of the identified joint on the coupling process, it is to validate the implementation of the coupling algorithm. The dual coupling (LM-FBS) algorithm is applied and verified using an additional implementation of primal coupling. The focus of the evaluation is on the first two bending modes mode 1 and mode 2. Therefore, the receptance entries  $Y_{qm}^{AJB}(2,2)$  for mode 1 in  $z$ -direction and  $Y_{qm}^{AJB}(1,1)$  for mode 2 in  $y$ -direction are depicted during the following evaluation. The two modes will be shown more detailed in a zoomed section in each of the following plots. The respective upper plot shows the  $z$ -direction with mode 1 and the lower plot the  $y$ -direction with mode 2.

Figure 4.25 shows that the implemented primal and dual coupling approaches lead to the same result. Hence, it can be assumed that the implemented codes are correct. From now on, only dual coupling is used. Note the following notation:  $Y_{qm}^{org}$  states the original assembled measurements transformed onto the IDMs that are the basis for the joint ID.  $Y_{qm}^{A*KB}$  is the coupled receptance of part A\* (A plus bolt), parameterized stiffness  $K$ , and part B.



In addition to the comparison of the primal and dual implementation, Figure 4.25 gives a first impression of the FBS results. Overall, the coupling results match the reference measurements pretty good. However, it is noticeable that the coupled results for the modes deviate slightly from the original measurements. Meaning that the eigenfrequencies (peaks) of mode 1 and mode 2 in  $Y_{qm}^{A*KB}$  do not match the frequencies of mode 1 and 2 in  $Y_{qm}^{org}$ . This can have different origins: one cause may lie in modeling errors of the VPT because of the assumption of a rigid interface. In addition, measuring the parts separately can cause errors. E.g., the dynamic influence of attaching the bolt to one of the parts. Further, when measuring the separate parts, each beam behaves very linear and the non-linearities originating from the interface of the assembled system are missing. Next to that, another cause can be a wrong or too inaccurate parameterization of the stiffness. It may also be that the application of inverse

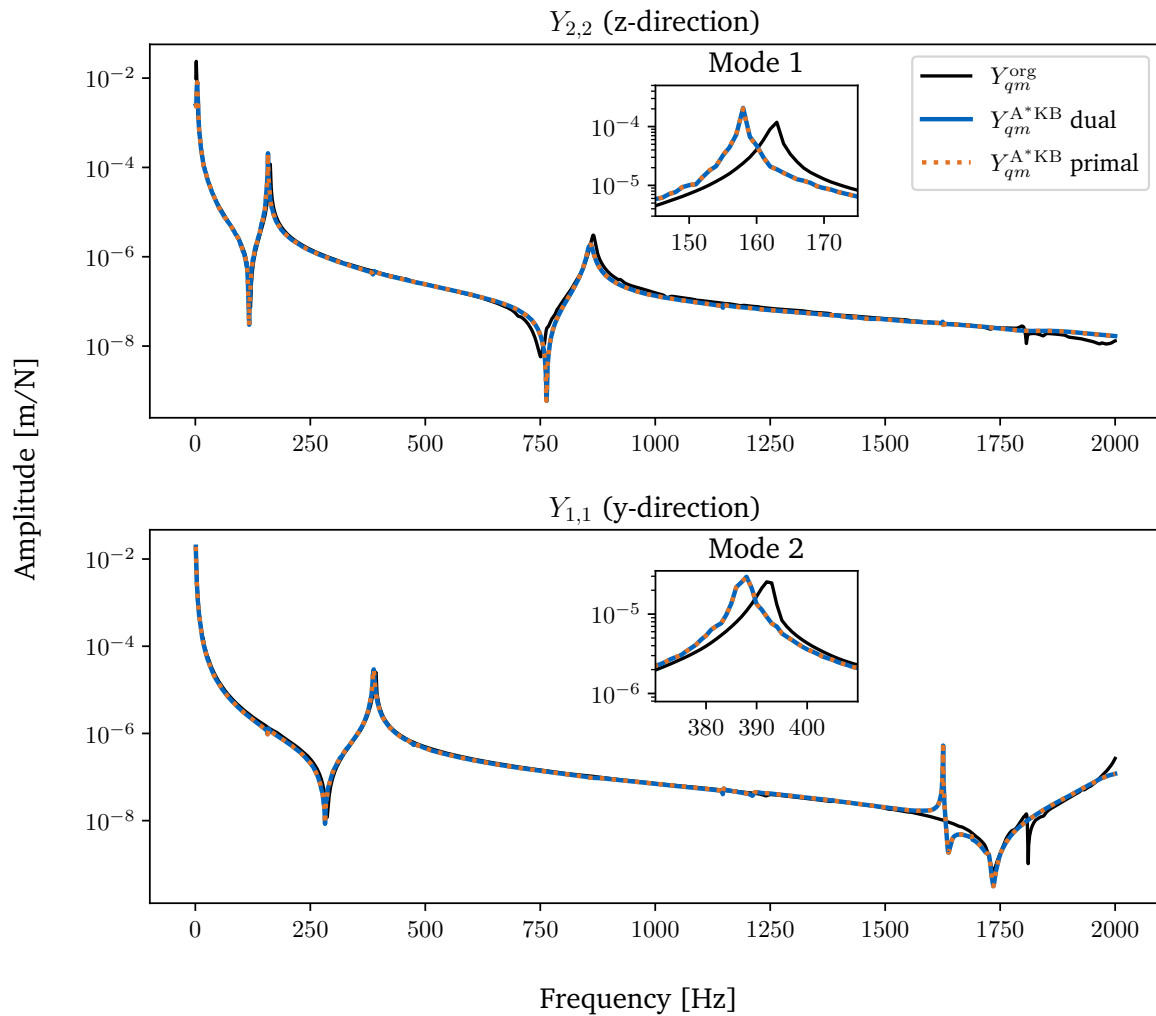


**Figure 4.25:** Verification of dual coupling with primal coupling

substructuring itself is the source of the error and it cannot be applied to this system. The different causes are discussed during the evaluation.

#### AB vs. A\*B vs. AB\*

First, the quality of the separated measurements is discussed. Factors such as the shifted mass distribution, especially by attaching the bolt to one of the parts, can affect the measurements. Therefore, it is necessary to take a look at the coupling of A and B while ignoring the joint. Coupling A and B with the bolt attached to one of the two parts (A\*B or AB\*) as well as coupling the parts without the bolt attached to a part (AB) are compared. The coupling without joint corresponds to coupling with infinitely high stiffness at the interface. The goal is to find out if there are already modeling errors in the early processing of part A and B that may cause the failure of the coupling process. In addition, it is to verify that the coupling of a part with bolt and one without is valid.

Figure 4.26 shows that coupling part A and B without bolt (AB) shifts the entire receptance towards higher frequencies, whereas for mode 1, the shift is very small. Coupling A\*B or AB\* leads to a slight increase of the stiffness of mode 2 with respect to the reference. This corresponds to expected behavior for increased joint stiffness (here: infinite joint stiffness). However, when coupling A\*B or AB\*, the eigenfrequency of mode 1 is lower

than the original eigenfrequency. This suggests that there is already an inaccuracy in the measurements or modeling errors caused by the VPT of A and B. In addition, contrary to expectations, it makes a big difference if the bolt is attached to A or B. A better coupling result with respect to the proximity to the reference measurements may not be possible. Nevertheless, using  $A^*$  and B for the coupling seems to be a good basis and will be used in the following.

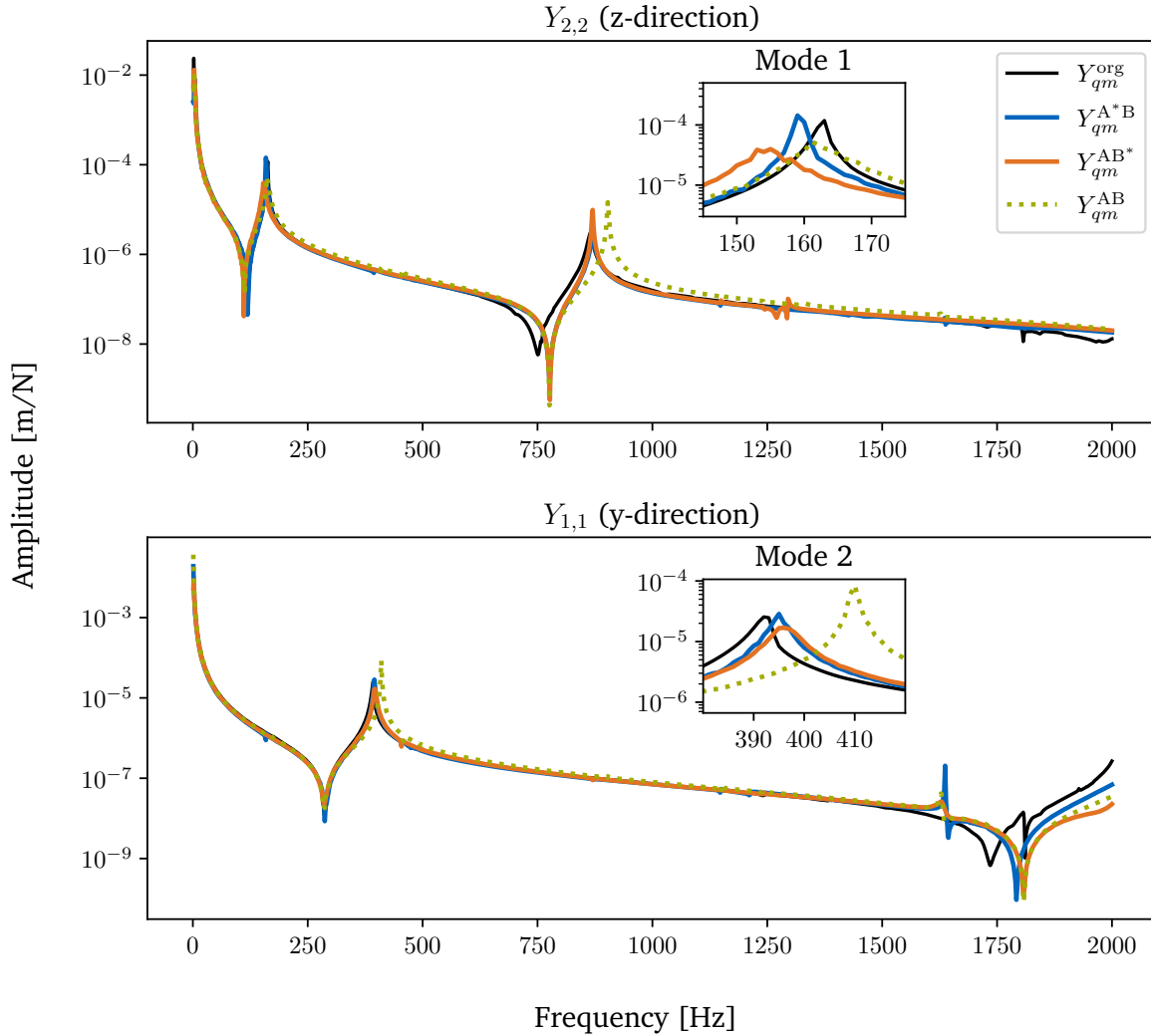


**Figure 4.26:** Comparison of coupling with AB,  $A^*B$ , and  $AB^*$

It is noticeable that coupling without joint already leads to very good results. This indicates that the joint is much stiffer than parts A and B. In other words, the dynamics of the assembled system are dominated by the dynamics of part A and B and the joint's dynamics only have a small impact. This will be discussed in more detail later on.

### J vs. K

Another factor that influences the quality of the coupling results is the estimation of the parameter  $K$  for the joint itself. First, it is to evaluate that using a constant and diagonal  $K$  is a valid approximation for the joint. Therefore,  $Y_{qm}^{A^*KB}$  is compared to  $Y_{qm}^{A^*JB}$  and  $Y_{qm}^{A^*J_dB}$  in Figure 4.27. For the coupling of  $Y_{qm}^{A^*JB}$ , the entire  $6 \times 6$  dynamic stiffness matrix of the joint  $Z_{qm}^J$  (off-diagonal matrix of  $Z_{qm}^{AJB}$ ) is used.  $Y_{qm}^{A^*J_dB}$  is coupled only using the diagonal part of  $Z_{qm}^J$  and

zeroing the off-diagonal entries.  $Y_{qm}^{A^*KB}$  corresponds to the coupling with the parameterized and diagonal  $K$ . It can be seen that the parameterization is a good approximation for the joint and even irregularities that occur when coupling with  $Z_{qm}^J$  or its diagonal can be filtered out.

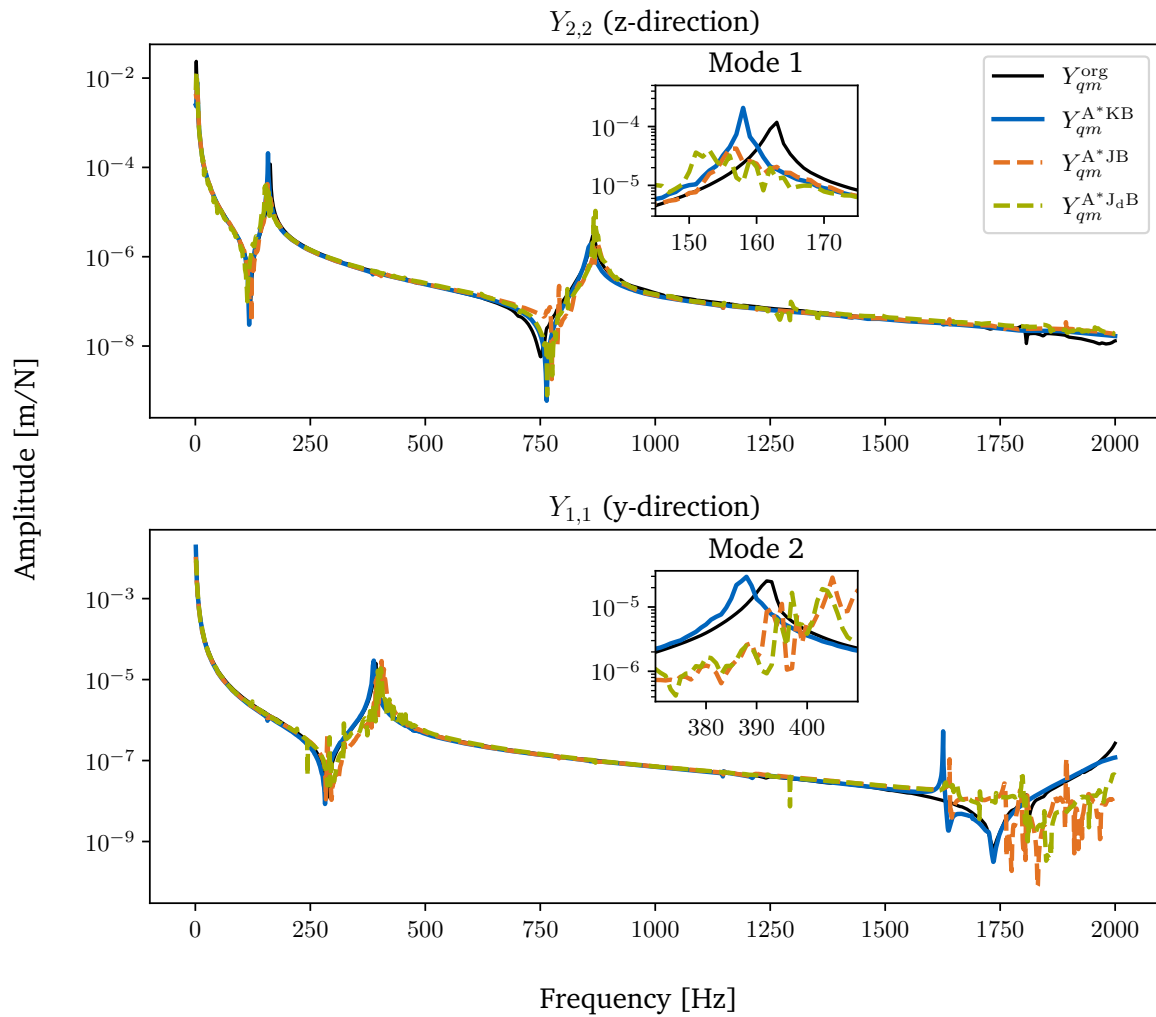


**Figure 4.27:** Comparison of coupling with the parameterized stiffness to coupling with original/diagonal joint

### K vs. 10K vs. 0.1K

In order to assess if or to what extent the identified stiffness values are correct, the coupling is conducted with the stiffness multiplied by 0.1 and 10. It is to evaluate which coupled result best matches the original measured receptance, whereas a good match means that the frequency of the coupled modes meets the original frequency.

As shown in Figure 4.28, the stiffness multiplied by 0.1 significantly shifts the receptance curve to lower frequencies and impairs the result. Multiplying the stiffness  $K$  by 10, however, has only a minor impact on the coupled results. This requires a more detailed consideration.

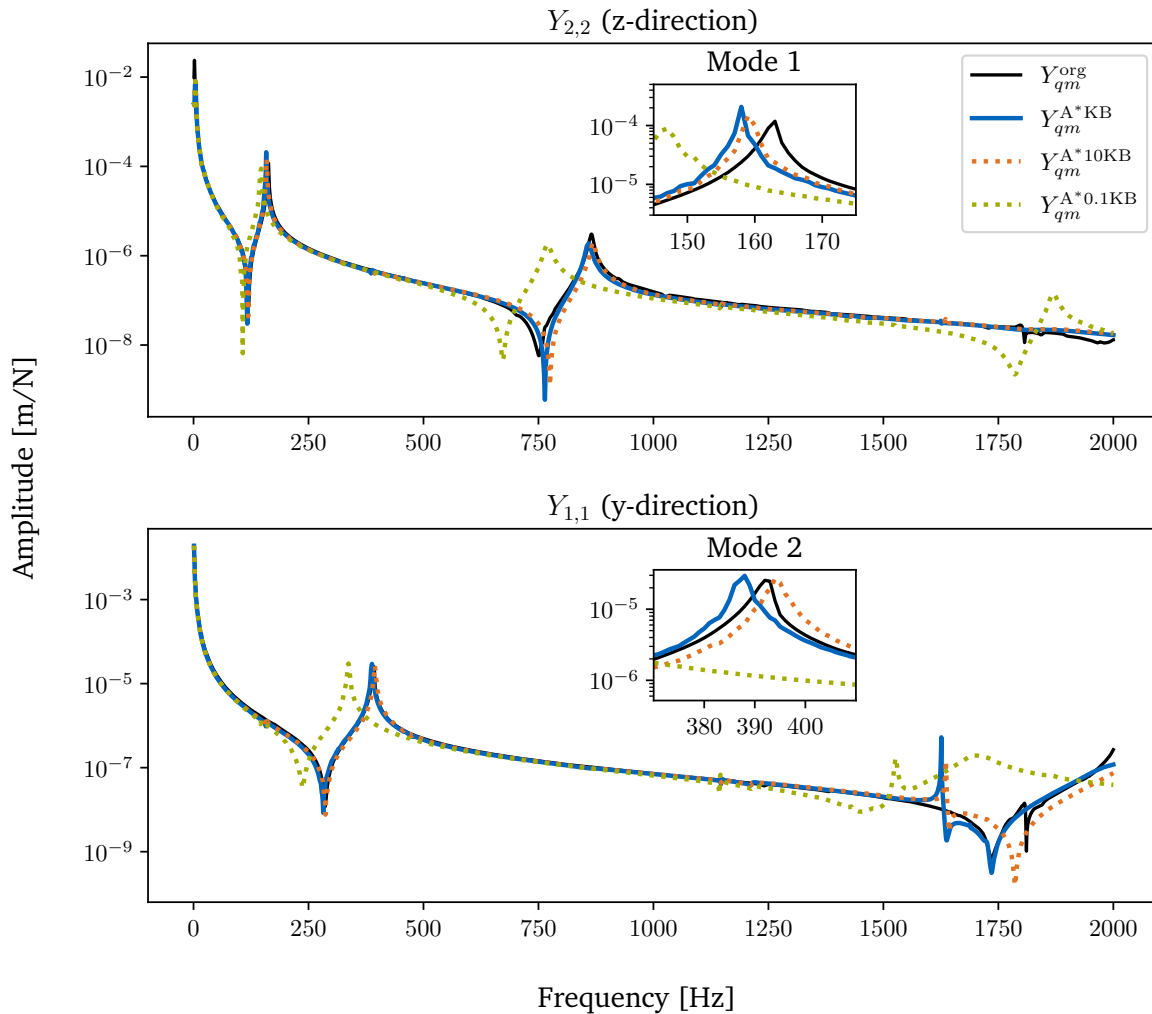


**Figure 4.28:** Comparison of coupling with  $K$ ,  $10K$ , and  $0.1K$

First, the influence of multiplying individual values  $k_i$  of  $K$  with 10 is considered. With Figure 4.29 and Figure 4.30, it becomes clear that multiplying the translational parts of  $K$  ( $k_x$ ,  $k_y$ , and  $k_z$ ) does not change the coupling result. In contrast to that, when multiplying a rotational value  $k_{rx}$ ,  $k_{ry}$ , or  $k_{rz}$  by 10 the modes are shifted to higher frequencies. Note that for  $Y_{qm}^{A*KB} 10k_{trans}$  in Figure 4.29 all translational stiffness values ( $k_x$ ,  $k_y$ , as well as  $k_z$ ) are multiplied by 10, whereas Figure 4.30 contains 3 different curves, each of which has  $k_{rx}$ ,  $k_{ry}$ , or  $k_{rz}$  multiplied by 10. Thereby, it was verified that multiplying individual  $k_i$  in  $k_{trans}$  also has no influence on the result.

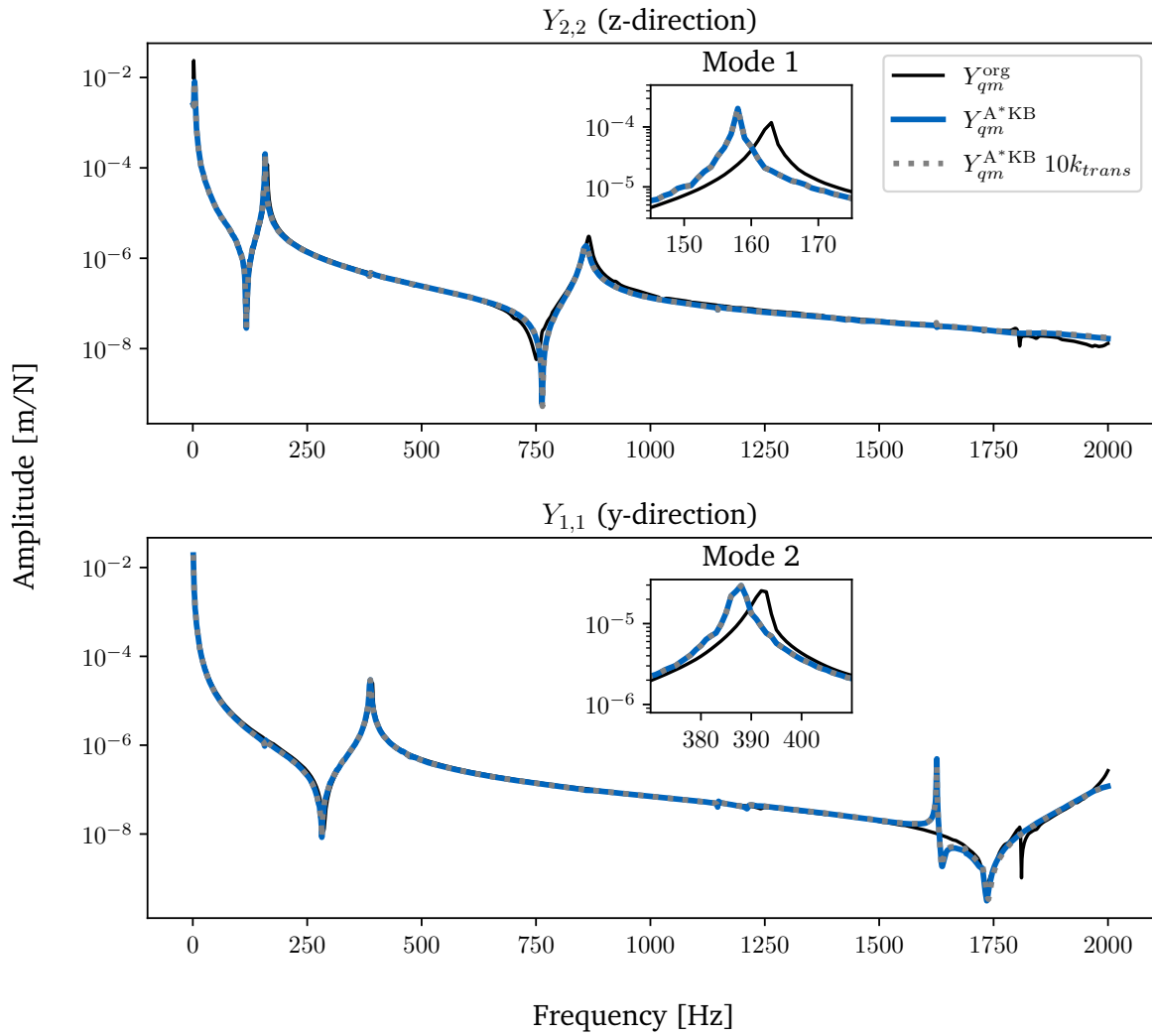


**Figure 4.29:** Comparison of coupling with  $K$  and  $10K_{trans}$

The rotational values of the stiffness  $K$  are much lower than the translational values and in the same range as the stiffness of parts A and B. Hence, changing the rotational stiffness still influences the system's dynamics. As shown in Figure 4.30, the coupling result of mode 1 changes when multiplying  $k_{ry}$  by 10. This is reasonable since mode 1 is bending in  $z$ -direction and 'around the  $y$ -axis'. Meaning that  $k_{ry}$  is the stiffness that counteracts the bending of mode 1. The coupling result of mode 2 changes when multiplying  $k_{rz}$  by 10. This is consistent to the effect for mode 1: mode 2 bends in  $y$ -direction and 'around the  $z$ -axis'. Thus,  $k_{rz}$  counteracts the bending of mode 2. For the shown FRFs, multiplying  $k_{rx}$  by 10 has no visible effect. For other FRFs in  $Y_{qm}^{A*KB}$ ,  $10k_{rx}$  has an impact on the coupling result at higher frequencies.

Considering to what extent the coupling results match the reference, the following applies for the rotational stiffness values: for mode 1, the coupling results with  $10k_{ry}$  are closer to the reference  $Y_{qm}^{org}$  than coupling with the identified  $K$ . However, for mode 3 the stiffness  $10k_{ry}$  seems to be too high and  $k_{ry}$  the better value. Also, for mode 2 no reliable statement can be made whether the coupling result is better for  $k_{rz}$  or  $10k_{rz}$ . But overall, it can be shown that the identified values for the rotational stiffness are correct (or at least in the correct range) since a variation significantly affects the reconstructed FRFs. Thus, the failure of missing the reference might have another origin. However, it is possible that the poorly observable value



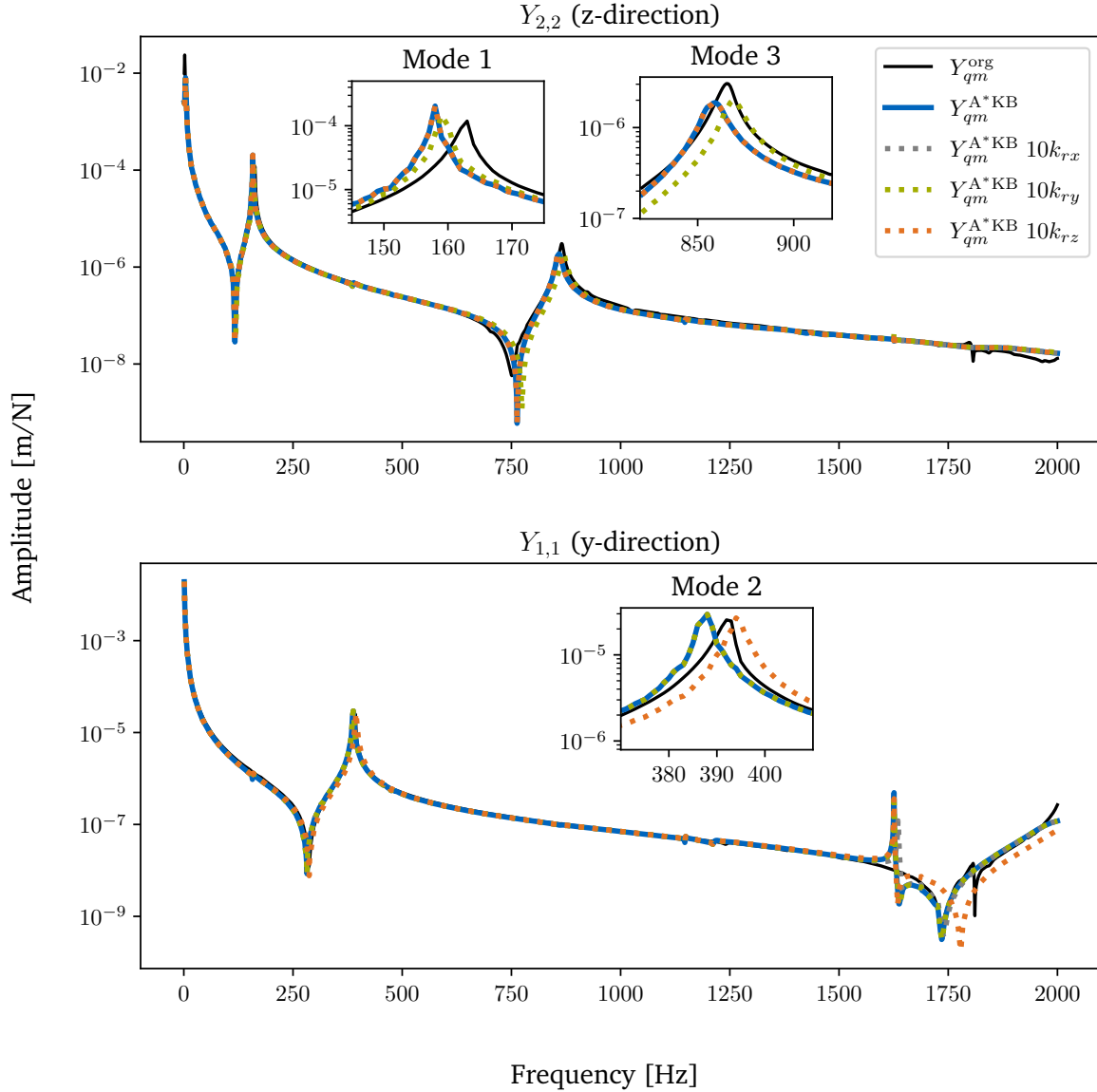


**Figure 4.30:** Comparison of coupling with  $K$  and  $K$  with  $10k_{rx}$ ,  $10k_{ry}$ , or  $10k_{rz}$

$10k_{ry}$  is underestimated. This is examined again when comparing FBS to the results with HT in section 4.4.

The fact that multiplying the translational parts by 10 does not influence the coupling results is surprising. For this, two possible explanations are found: one explanation can be that the identified translational stiffness is not the actual stiffness but rather a lower limit of the actual stiffness. The other explanation is that the reconstruction process fails and the identified stiffness is the correct one. An origin for both assumptions lies in the high stiffness of the joint with respect to the stiffness of the parts.

Figure 4.31 shows the absolute stiffness  $Z_{qm}^{org}$  of the assembled system compared to the absolute stiffness  $Z_{qm}^{AB}$  of the separately measured parts A and B. The matrix  $Z_{qm}^{AB}$  contains the stiffness of A and B in block-diagonal form. Note that the depicted entries  $Z_{qm}^{AJB}(1,1)$  and  $Z_{qm}^{AJB}(2,2)$  contain only the stiffness of part A and joint J (subsubsection 2.2.3). Since part A and B are identical, an additional consideration of part B is omitted. Next to that, a plot where the stiffness of the parts A and B is removed from the assembled system  $Z_{qm}^{AJB} - Z_{qm}^{AB}$

is shown. According to inverse substructuring, this should correspond to the stiffness of the joint. It is clear to see that removing the stiffness of part A and B makes almost no difference. This means, that the stiffness of the assembled system is mainly determined by the joint's stiffness and the contribution of the parts is negligible. The other way round, the admittance (inverse of stiffness) of the assembled system is dominated by the admittance of part A and B whereas the joint only participates poorly. This can lead to the dynamic of the joint being covered by the dynamics of A and B so that increasing the translational stiffness of the joint has no effect on the overall dynamics of the assembled system. Thus, the ID of the joint is bounded by the lower limit. Meaning that the minimum  $K$  is identified, for which the system shows the present behavior, and not the actual stiffness. When increasing the torque level this lower limit shifts to higher values, since the overall dynamics of the assembled system change.

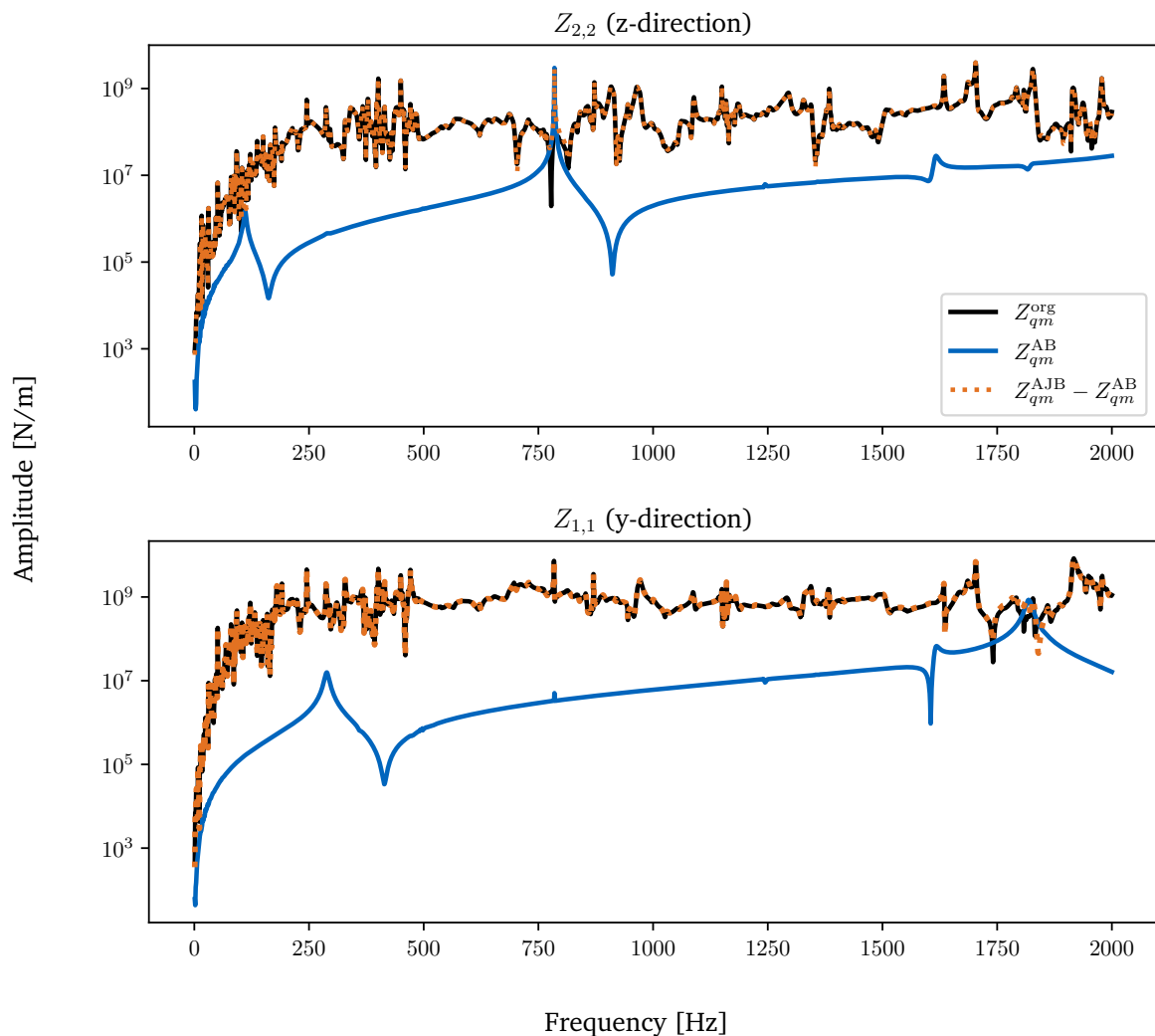


**Figure 4.31:** Comparison of  $Z_{qm}^{AJB}$  and  $Z_{qm}^{AB}$

In contrast to that, the theory that the identified  $K$  is correct is supported by the fact that clear lines for the values of  $K$  can be observed during the parameterization (at least for the values with a good observability). If the parameterization of the joint is correct, this means that the coupling reconstruction/coupling process fails. This can be caused by the assumptions of no cross coupling and a mass-less joint not being valid. As a consequence, the coupling cannot be applied properly.

The theory that the coupling process fails is also supported by the fact that the coupling is not sensitive to an increase of the stiffness at all. Figure 4.32 shows the coupled results with  $10^8 k_{trans}$ : It still leads to the same curves when neglecting the slight shift above 1600 Hz for  $Y_{1,1}$ . This shows, that the coupling process is not even sensitive to a significant increase of the translational stiffness. As a consequence, it cannot be proven that the estimated translational stiffness values are correct. At the same time, it is not clear if the reconstruction/coupling process fails.

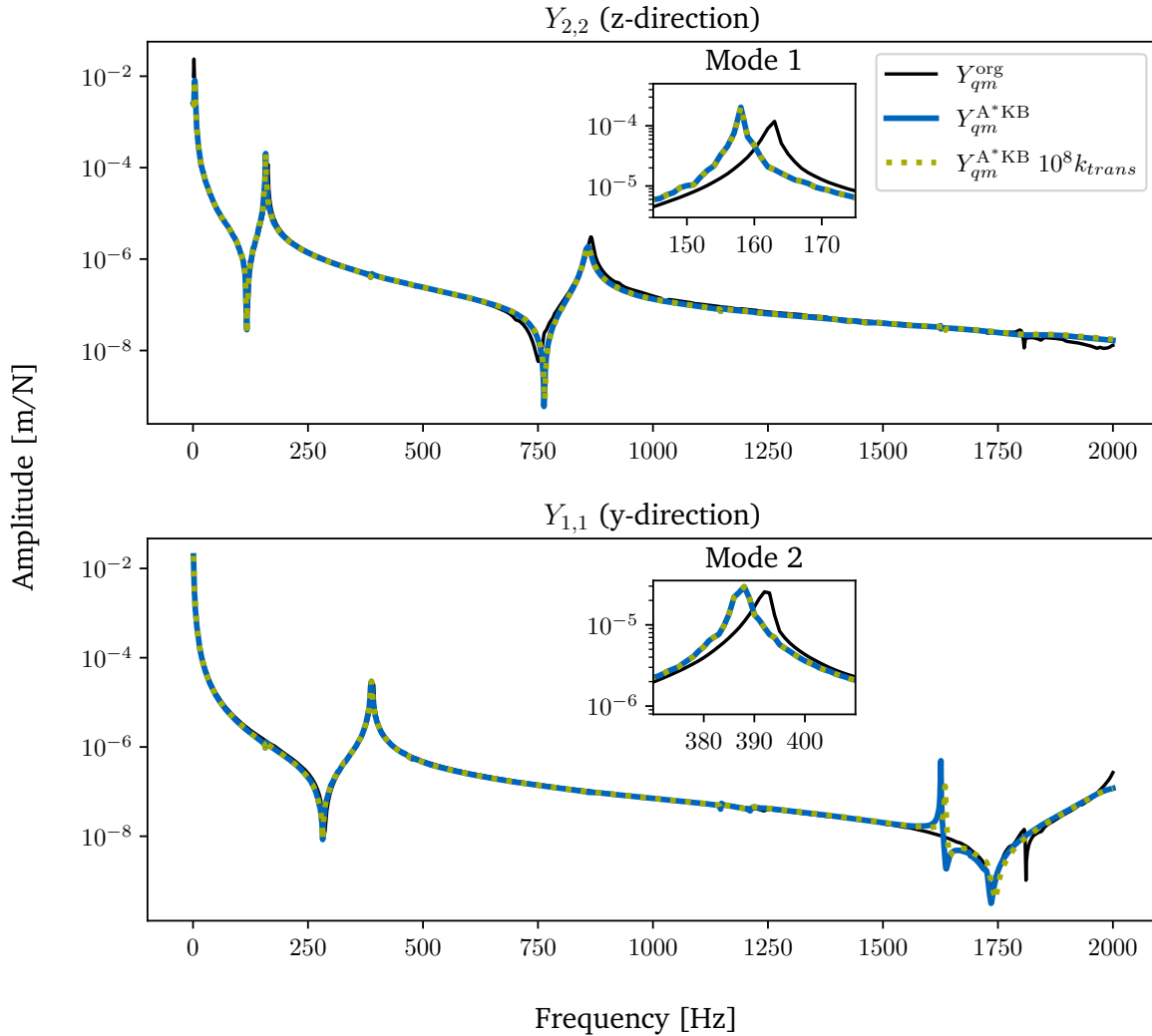


**Figure 4.32:** Comparison of coupling with  $K$  and  $10^8 K_{trans}$

#### 4.4 Comparison of Non-Linear and Linear Joint Identification

For the comparison of the linear and non-linear joint ID, the entire campaign 2 is considered. This includes one linear and one non-linear test run for all torque levels. The results of the joint parameterization are shown in Figure 4.33. It is noticeable that the values of  $K$  increase consistently when increasing the torque level except  $k_{ry}$  for 50 N m. This drop of the value is probably caused by an incorrect parameterization due to the bad observability of  $k_{ry}$  and not because the rotational stiffness around the  $y$ -axis actually drops.

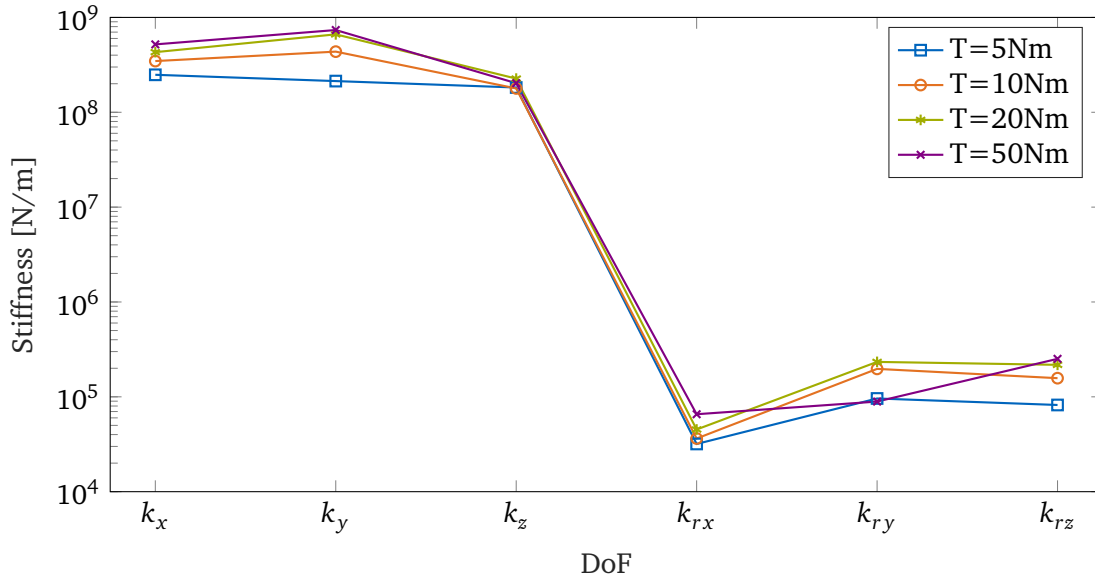


**Figure 4.33:** Parameterized  $K$  of 'C2-50 N m-LIN'

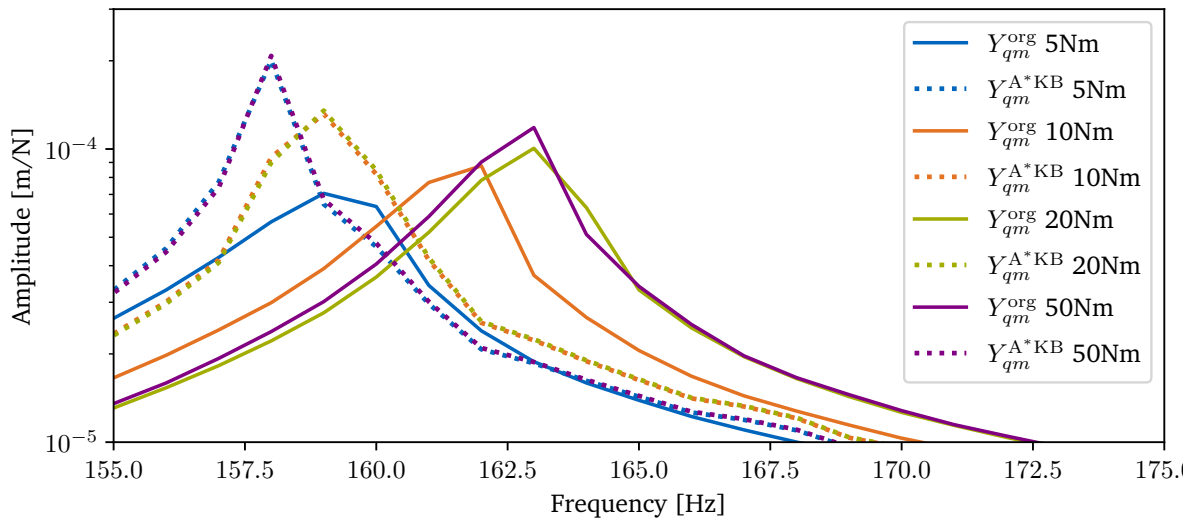
In the following, the results of HT are compared to the original FRFs before comparing the results of FBS to the ones of HT.

The backbone curves in Figure 4.34b show an increase in the frequency from 5 N m to 20 N m. This can also be seen for the original FRFs in Figure 4.34a, since the mode's frequency shifts to the right. The mode with a torque level of 5 N m of the original FRFs contains the greatest distortion caused by non-linearities. The higher the torque level the more linear the mode shape becomes. This can also be observed for HT: the higher the torque level, the lower the slope of the backbone curves. For the damping the occurrences in Figure 4.34a and 4.34b also match: the amplitude dependent damping originating from HT is largest for 5 N m, which is reflected by the amplitude of this FRF being the lowest compared to the FRFs of the remaining torque levels.

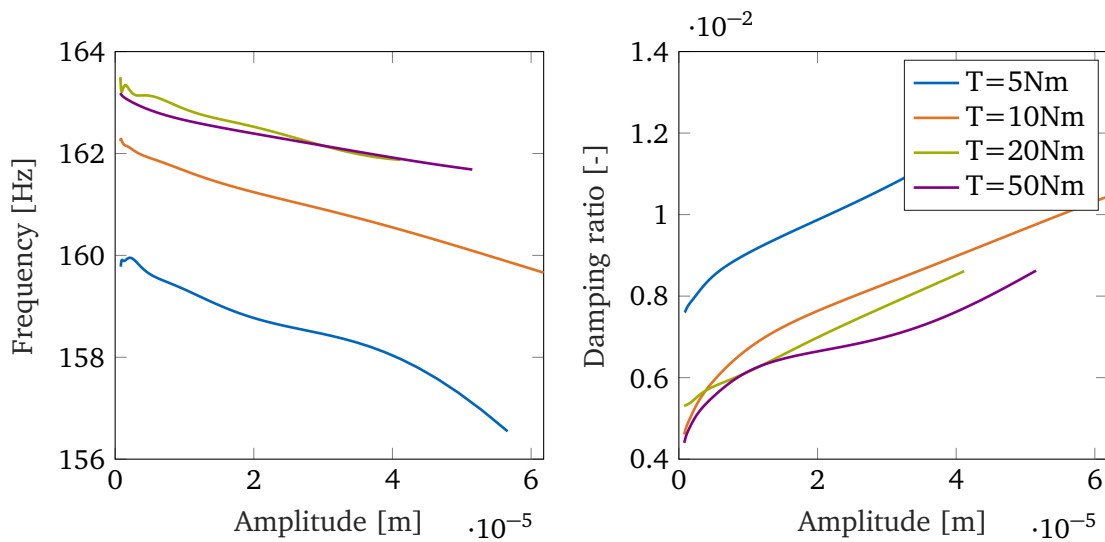
Considering the resulting FRFs  $Y_{qm}^{A*KB}$  of the coupling in Figure 4.34a, the trend of an increasing frequency can be observed between 5 N m and 10 N m. However, there is no clear difference between  $Y_{qm}^{A*KB}$  of 10 N m and  $Y_{qm}^{A*KB}$  of 20 N m. This shows that the coupling process is not sensitive enough to the slightly different values of  $K_{10Nm}$  and  $K_{20Nm}$ . In addition to that, the coupled FRF with a torque level of 50 N m almost complies with the one of 5 N m. The cause for the FRF of 50 N m being so far to the left becomes clear when considering the values of the stiffness in Figure 4.33 again: the value  $k_{ry}$  for 5 N m and 50 N m is almost the same. However, the analysis in section 4.3 showed that the coupling of mode 1 is sensitive to changes of  $k_{ry}$ . Therefore, it can be assumed that the shift in  $Y_{qm}^{A*KB}$  of 50 N m is caused by the low value of  $k_{ry}$ . Figure 4.35 confirms this assumption: before coupling,  $k_{ry}$  is multiplied by 10. Thus, the value is above  $k_{ry}$  for 20 N m and the corresponding FRF is shifted to the right.

The neglected damping during the coupling can be seen by the fact that the increase of the amplitude with increasing torque level does not appear. On the contrary, the amplitude for 5 N m is the largest of the coupled FRFs (or as large as the amplitude for 50 N m) but the lowest one of the original FRFs.

On the whole, it can be said that the coupling process of mode 1 fails at least for a torque level of 50 N m. The coupling strongly depends on the estimation of  $k_{ry}$ , however, the value is poorly observable. To achieve a better coupling result for mode 1, a new test setup has to be created, for which  $k_{ry}$  is well observable.



(a) Coupling results for mode 1 for different torque levels



(b) Backbone and damping curves for mode 2 for different torque levels

Figure 4.34: Comparison of FBS and HT for mode 1

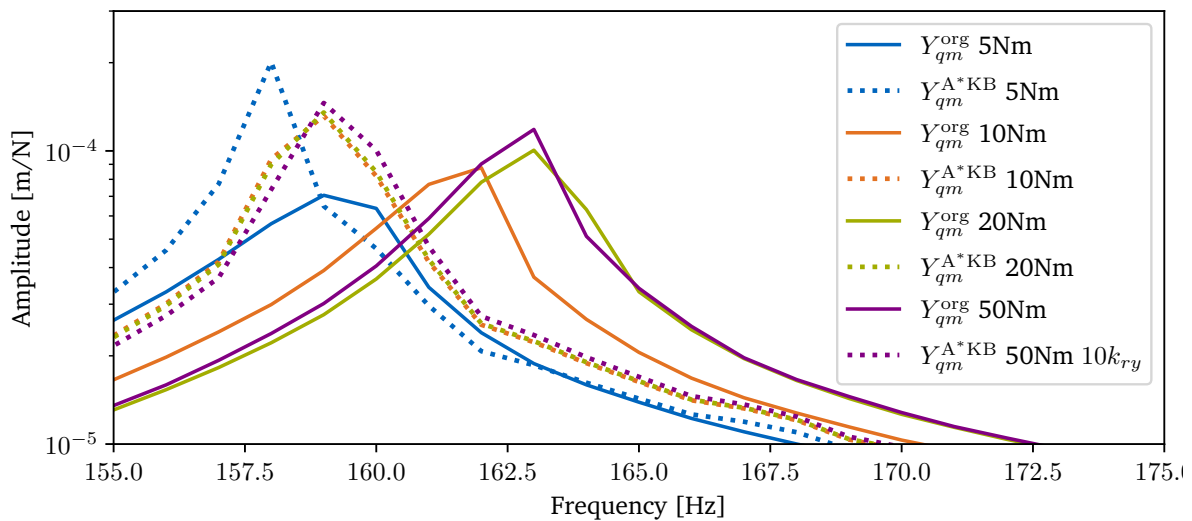


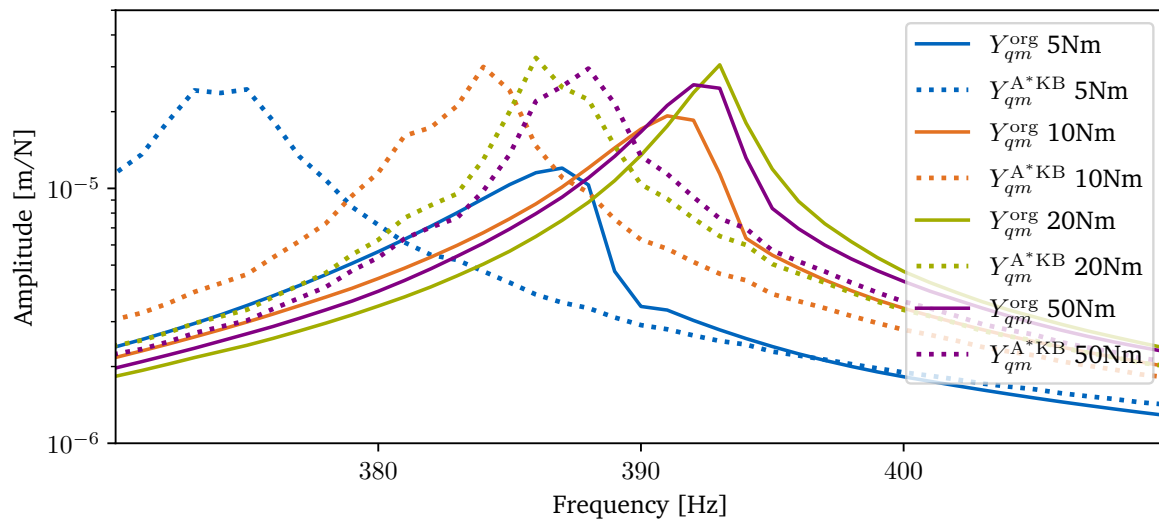
Figure 4.35: Coupling results of mode 1 with  $10k_{ry}$  for different torque levels

Further, the results of linear and non-linear joint ID are compared for mode 2 in Figure 4.36. The coupling results for mode 2 seem to be more accurate than for mode 1 (Figure 4.36a). The general shift of the frequency when increasing the torque level can be recreated. Again, the difference in amplitude between the curves cannot be reconstructed since damping is neglected.

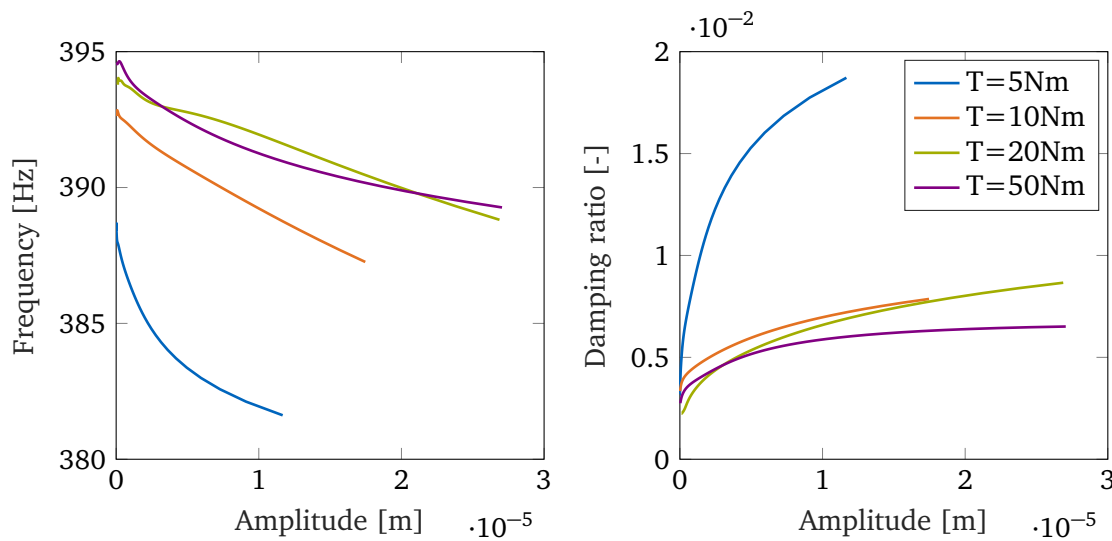
Taking the distance that lies between the peaks of  $Y_{qm}^{A*KB}$  and the respective  $Y_{qm}^{org}$  into account, it can be seen that the largest distance is between the curves of 5 N m. In other words, the error made during the coupling is the highest for 5 N m, since the coupled frequency of mode 2 is far away from the original eigenfrequency. One factor that causes this high shift is the fact that for this torque level, the highest drop of the frequency by approximately 7 Hz can be observed in the respective backbone curve (Figure 4.36b). Thus, the measurements for 5 N m contain the most non-linearities. This can also be seen from the fact that the distortion of  $Y_{qm}^{org}$  is the strongest. During the coupling process, these non-linearities are averaged and the stiffness is calculated based on the average of the non-linearities. In this case, the error that is made when averaging the non-linearities is up to 7 Hz. However, the shift of the frequency between coupled and original FRFs is more than 10 Hz. Meaning that other factors as discussed previously also cause the coupling to fail.

For 20 N m or 50 N m the difference in frequency between  $Y_{qm}^{A*KB}$  and  $Y_{qm}^{org}$  is less. Also, the drop of the backbone curves is lower and thus, the error made by averaging the non-linearities is lower. The linearization made during the FBS is clearly reflected in the mode shape: The modes of  $Y_{qm}^{org}$  contain a distortion caused by non-linearities, whereas the modes of  $Y_{qm}^{A*KB}$  are characterized by a very linear shape.

To conclude, the coupling of mode 2 manages to reconstruct the increase of the stiffness in the parameterization as well as in the coupling result. However, the error that is made through FBS is still high and partly caused by averaging non-linearities.



(a) Coupling results for mode 2 for different torque levels

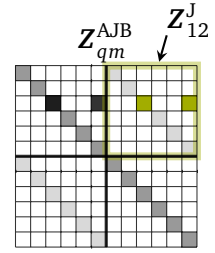


(b) Backbone and damping curves for mode 2 for different torque levels

Figure 4.36: Comparison of FBS and HT for mode 2

#### 4.4.1 Review of the Inverse Substructuring Assumptions

For the linear joint ID, it is assumed that the prerequisites of no cross coupling and a mass-less joint for inverse substructuring are fulfilled. However, it is to verify to what extent these conditions apply to the used test system. This can be achieved by comparing the stiffness of the assembled system minus the stiffness of the parts  $Z_{qm}^{AJB} - Z_{qm}^{AB}$  to the joint  $Z_{12}^J$ . If they match, inverse substructuring is valid. More precisely, it is to check if or to what extent the orange curve in Figure 4.37 matches the green curve. Note that  $Z_{12}^J$  is the off-diagonal  $6 \times 6$  matrix of  $Z_{qm}^{AJB}$  and thus, the joint's stiffness according to inverse substructuring.  $Z_{qm}^{AB}$  contains the stiffnesses of the separate measured parts A and B in block-diagonal form. Again, the depicted stiffness curves contain only the stiffness of part A and joint J and an additional consideration of part B is omitted. The shown curves are the absolute values of the stiffnesses.



The figure shows that removing A and B from the stiffness of the assembled system makes almost no difference. Again, this means that the stiffness of the parts is negligible for the majority of the frequency range. For both, the diagonal curve  $Z_{2,2}$  in the upper as well as the off-diagonal curve  $Z_{2,5}$  in the lower plot, the orange and the green curve show slight differences. This suggests that there is cross coupling in the system or a mass of the joint. In addition, the fact that the stiffness of the joint  $Z_{12}^J$  is on the same level as  $Z_{qm}^{AJB}$  indicates that strong cross coupling is present. An error due to presence of a joint mass is less likely, since the mass of the bolt itself is taken into account (A\*). However, it is still possible that a disparate mass distribution causes errors in the coupling.

Next to the presence of cross coupling or a joint mass, it can be that the measurements of the disassembled parts provoke an error. Meaning that the measurements of the separated parts differ from the measured behavior in the assembled system. On the one hand, when measuring the parts separately, the non-linear effect of the interface is missing and the beams behave very linear. Furthermore, it is noticeable that the amplitude increases at the frequency of 785 Hz when removing  $Z_{qm}^{AB}$  from  $Z_{qm}^{AJB}$  (orange curve is higher than the black curve). This is caused by the stiffness of A being negative at 785 Hz and the subtraction thus becomes an addition. Here, the deviation of the orange curve from the green curve is particularly clear. The green curve approaches the stiffness curve of the assembled system (black) which includes the dynamics of A.

To sum up, the fact that the green and the orange curve do not match perfectly can have three different origins: the presence of cross coupling, a joint mass, or erroneous measurements of the parts. In other words, it is not clear whether the small difference that can be seen in the plots of the coupling is caused by an erroneous reconstruction later on. Thus, a reliable statement cannot be made about whether the degree to which the green and orange curves match is sufficient. A proposal for an alternative approach in order to verify if inverse substructuring is valid is given in chapter 5.



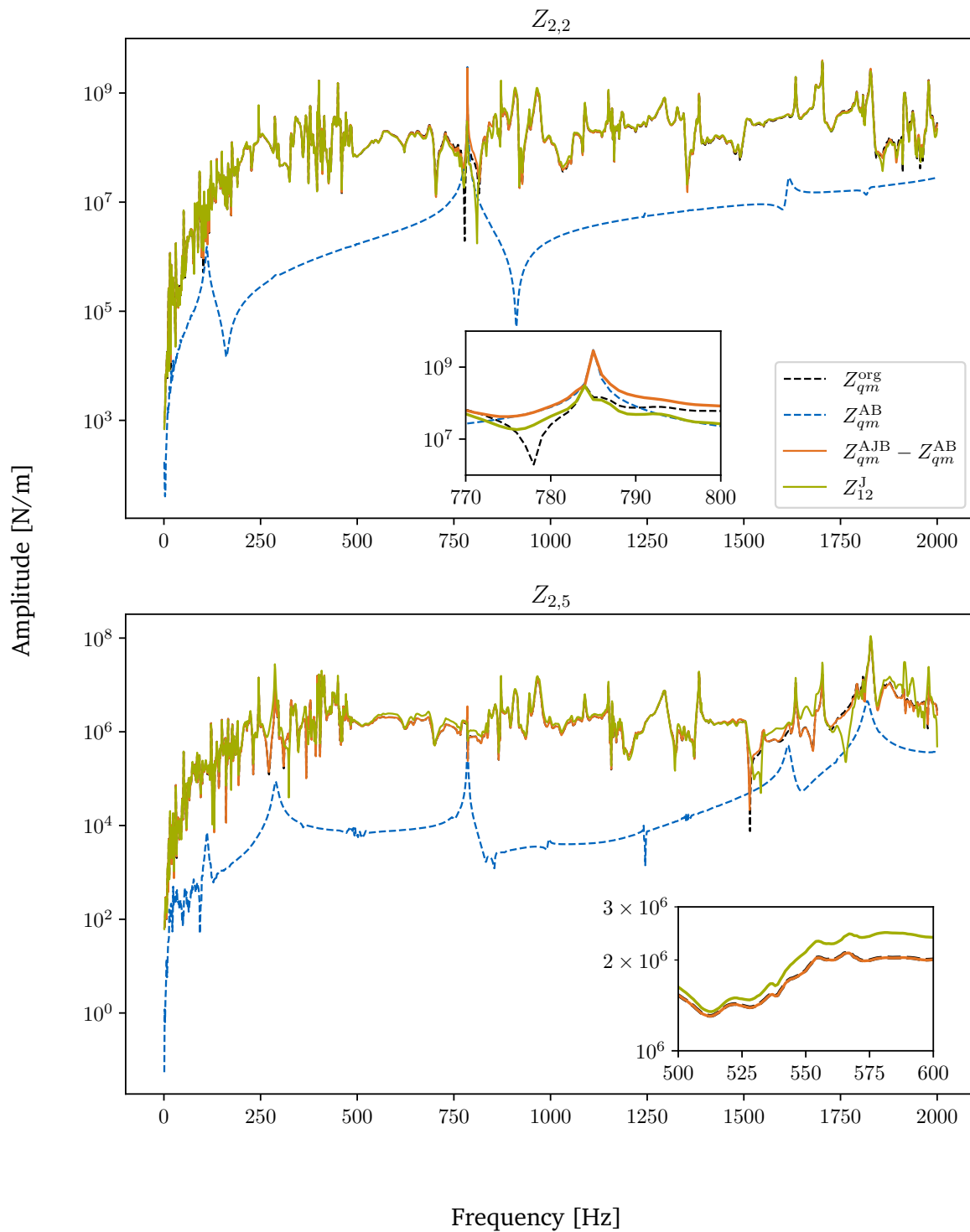
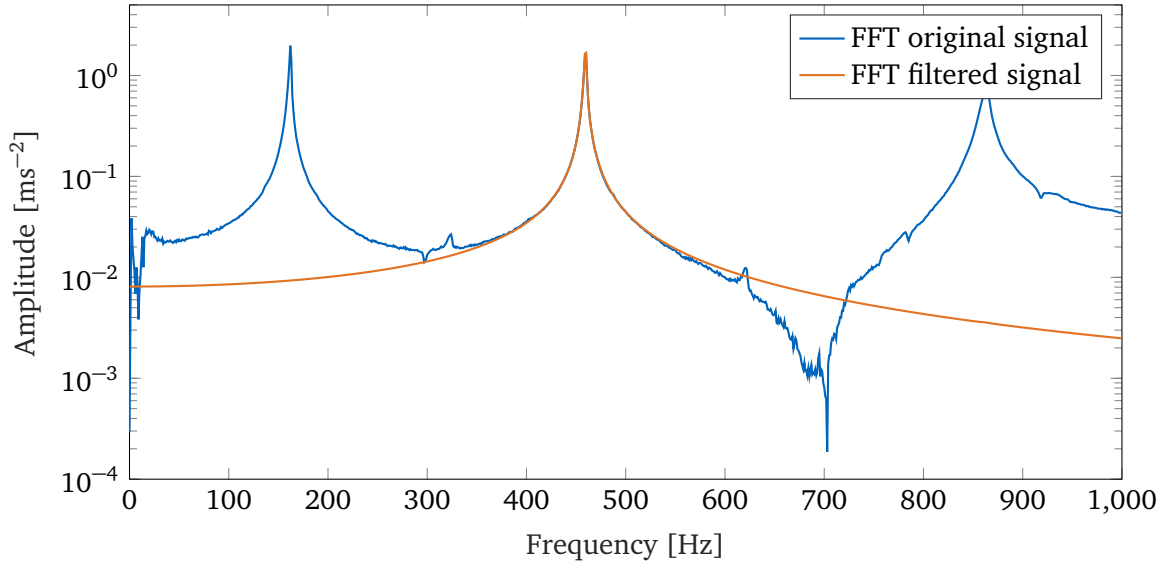


Figure 4.37: Evaluation of inverse substructuring conditions

## 4.5 Application of Zeroing and Back-Extrapolation

For the evaluation of the implemented ZEFFT and BE algorithm, a time signal of the tests for HT is used. First, the validity of the algorithm is proven with a mode that shows no obvious non-linearities. An impact in  $z$ -direction with a force of 100N is considered (torque level  $50\text{Nm}^{-1}$ ). The mode (third bending mode,  $z$ -direction) with an eigenfrequency of 460Hz seems to behave linear. Therefore, the back-extrapolated signal should be nearly identical to the original signal. Subsequently, the results of the algorithm for a mode that shows high non-linearities are presented. Figure 4.38 shows the FFT of the original and the band pass filtered signal.



**Figure 4.38:** FFT of original and band pass filtered signal of third bending mode (nearly linear)

After band pass filtering the signal, the ZEFFTs are calculated and plotted. Thus, it can be determined which zeroing time  $t_z$  will be used as basis for the BE. Attention must be drawn to  $t_z$  being high enough so that the non-linearities have disappeared. At the same time,  $t_z$  must not be too high and the signal has not decayed. Figure 4.39 depicts several ZEFFTs for the regarded mode with  $t_z \in [0\text{s}, 0.7\text{s}]$ . Since the mode shows no obvious non-linearities,  $t_z$  can be chosen very small ( $t_z < 0.1\text{s}$ ). For demonstration purposes a zeroing time of  $t_z = 0.4\text{s}$  is chosen. There, a clear signal with a usable ZEFFT is still present. Note that  $t_z$  is not exactly 0.4s since the algorithm depicts zero crossings of the signal for zeroing time points. In addition, the number of ZEFFTs is limited with an input variable and distributed over a given interval. If necessary, the number of ZEFFTs can be increased to gain a zeroing time closer to the desired time.

In Figure 4.40 the filtered and zeroed (FZ) time signal is shown. The irregularities at the end are a side effect of the filter. In order to properly curve fit the signal for the modal ID, it is truncated from  $t_z$  to 3s and shifted to 0s.

The modal ID is applied according to the description in subsection 3.3.1: after identifying the eigenfrequency  $\omega_0$  with an in-house development for modal ID in the frequency domain,  $\zeta_0$  and  $R_z$  are fitted to the truncated time signal (Figure 4.41). In this case the time interval of the fitted signal is  $[0\text{s}, 2.6\text{s}]$  (end time is  $3\text{s} - t_z$ ). For a better visibility, the fitting is only plotted up to 1s in Figure 4.41. The orange curve is the detected envelope  $u(t)$  using `envelope()`, whereas the dotted black curve is the result of fitting Equation 3.8 depending

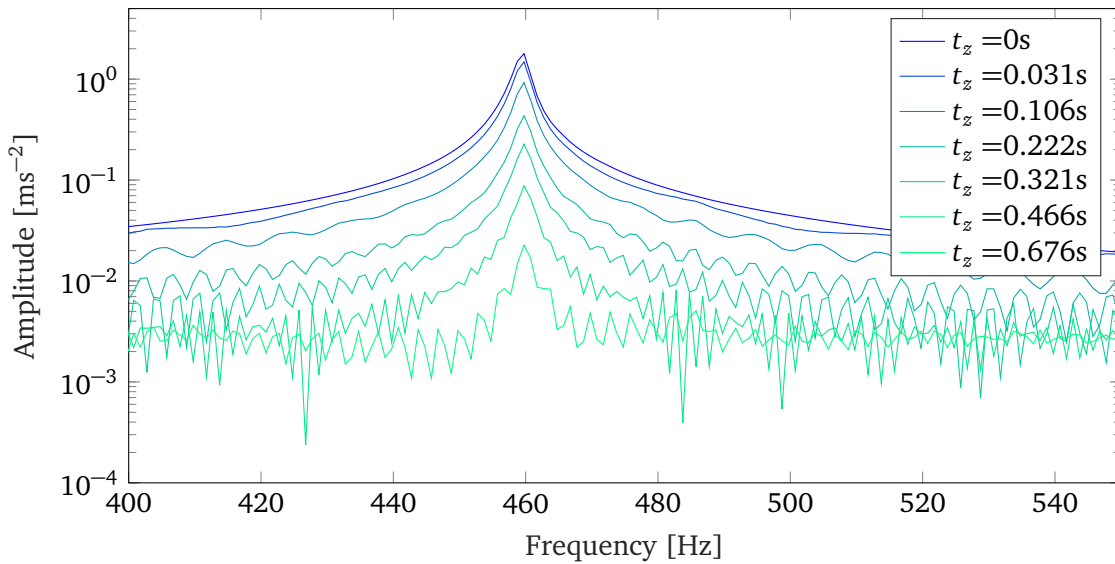


Figure 4.39: ZEFFTs with  $t_z \in [0\text{ s}, 0.7\text{ s}]$  of third bending mode

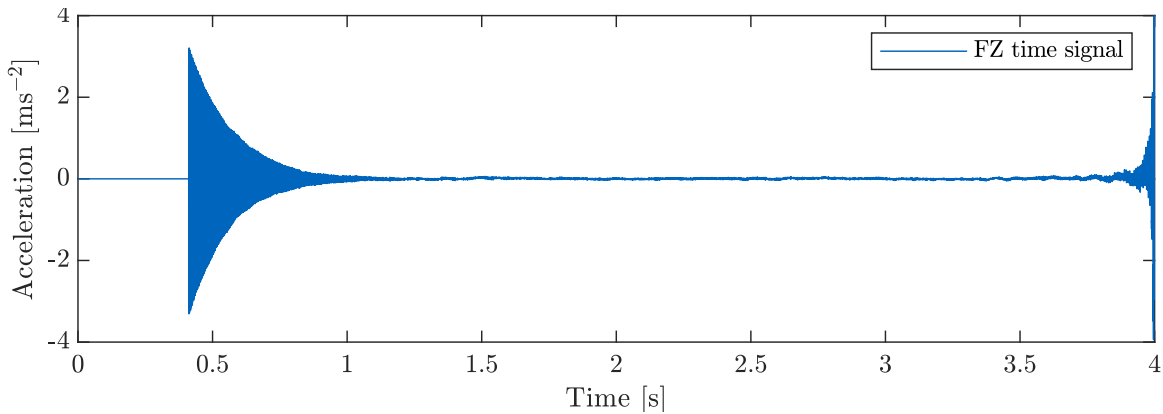


Figure 4.40: filtered and zeroed time signal of third bending mode

on  $\zeta_0$  and  $R_z$  to the detected envelope  $u(t)$ . The envelope of the back-extrapolated signal with the residue  $R_0$  compared to the original band pass filtered signal is illustrated in Figure 4.42. It is clear to see, that the back-extrapolated and the original envelope almost match. This proves that the BE process is valid, since the original signal shows linear behavior for the regarded mode. Thus, the original and the recreated signal without non-linearity are supposed to match.

Figure 4.43 summarizes the results in the frequency domain. After zeroing the filtered signal, the amplitude of the according FFT is lower than the original one. The orange curve pertains to the result of the modal ID before BE. Applying the BE results in a curve almost equivalent to the original signal. Again, this is reasonable, since the mode is nearly linear and thus, only very small non-linearities are filtered out. As can be seen in the zoomed cutout, the amplitude of the BE curve is slightly lower and the eigenfrequency slightly higher than for the original signal. This also proves the validity of the procedure, since it corresponds to the expected behavior.

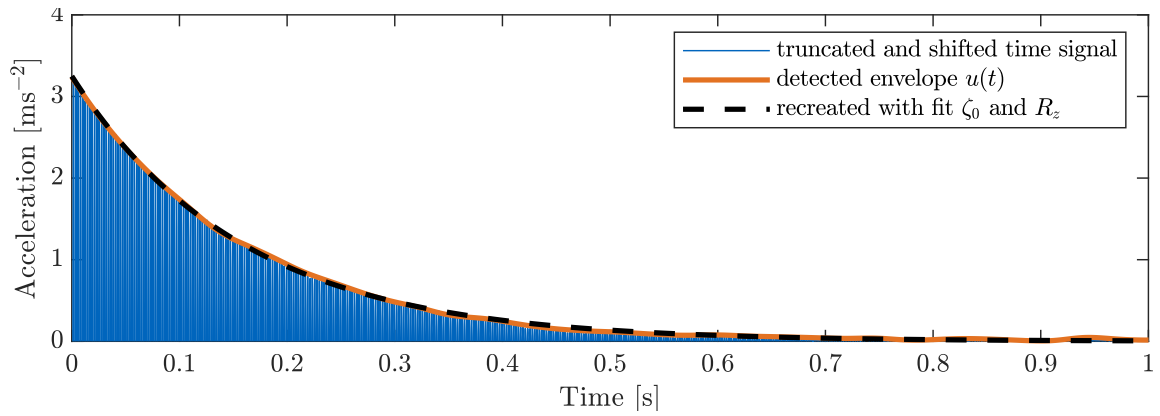


Figure 4.41: Detected and recreated envelope

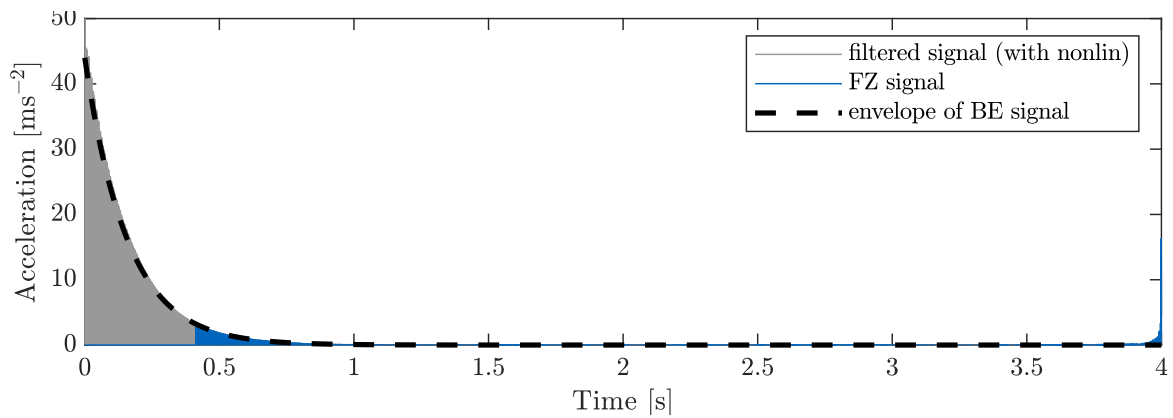


Figure 4.42: Back-extrapolated time signal

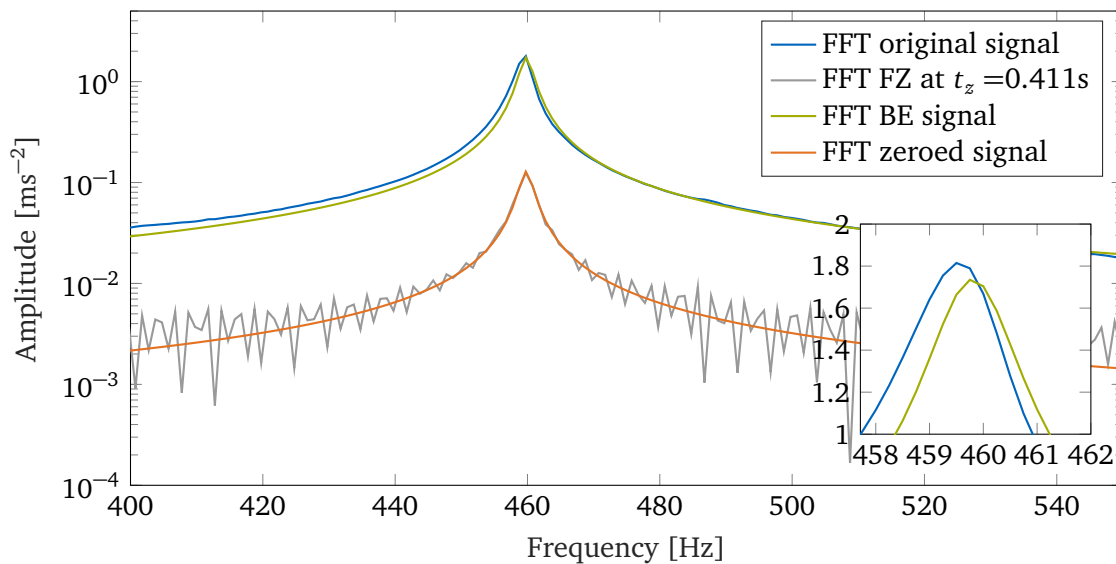
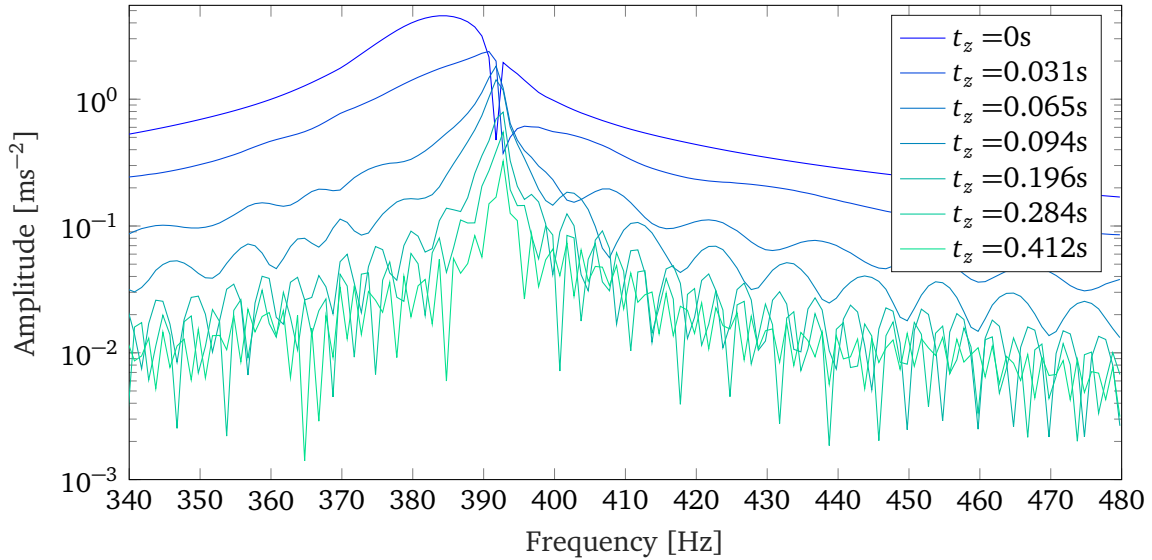


Figure 4.43: Results of modal ID and BE for linear mode

In addition to the linear mode, the results of ZEFFT and BE are shown for a mode with high non-linearities. An impact of the tests for HT in  $y$ -direction with a force of 500 N is considered (torque level 50 N m). The mode (mode 2,  $z$ -direction) with an eigenfrequency

around 385 Hz shows high non-linearities. Hence, the BE signal is expected to have a lower amplitude and higher eigenfrequency than the original signal.

With the aid of Figure 4.44 the zeroing time is set to  $t_z = 0.3$  s. At this point the non-linearities seem to have decayed and at the same time the left signal is sufficient for a reasonable result.



**Figure 4.44:** ZEFFTs with  $t_z \in [0\text{s}, 0.5\text{s}]$  of mode 2 (non-linear)

In Figure 4.43 the results for the ZEFFT and BE of the non-linear mode are summarized. Again, after zeroing the signal, the amplitude of the according FFT is lower than the original one. The orange curve pertains to the result of the modal ID before BE. In this case, the BE curve has a much lower amplitude than the original one and an increased eigenfrequency and thus, clearly shows the removed non-linearities. The higher the filtered out non-linearities, the bigger is the difference in amplitude and eigenfrequency.

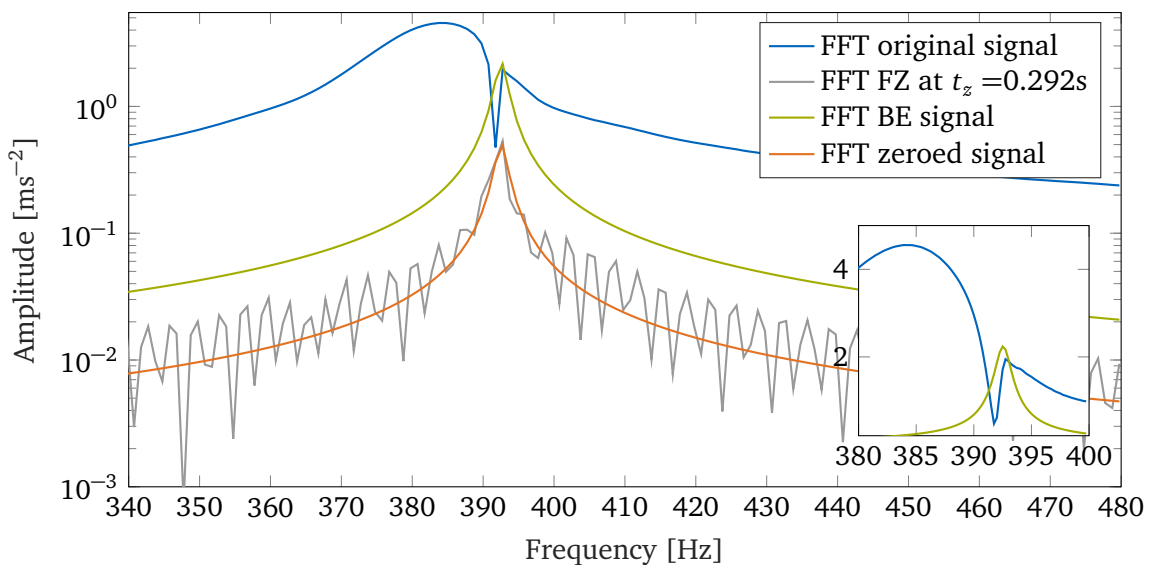
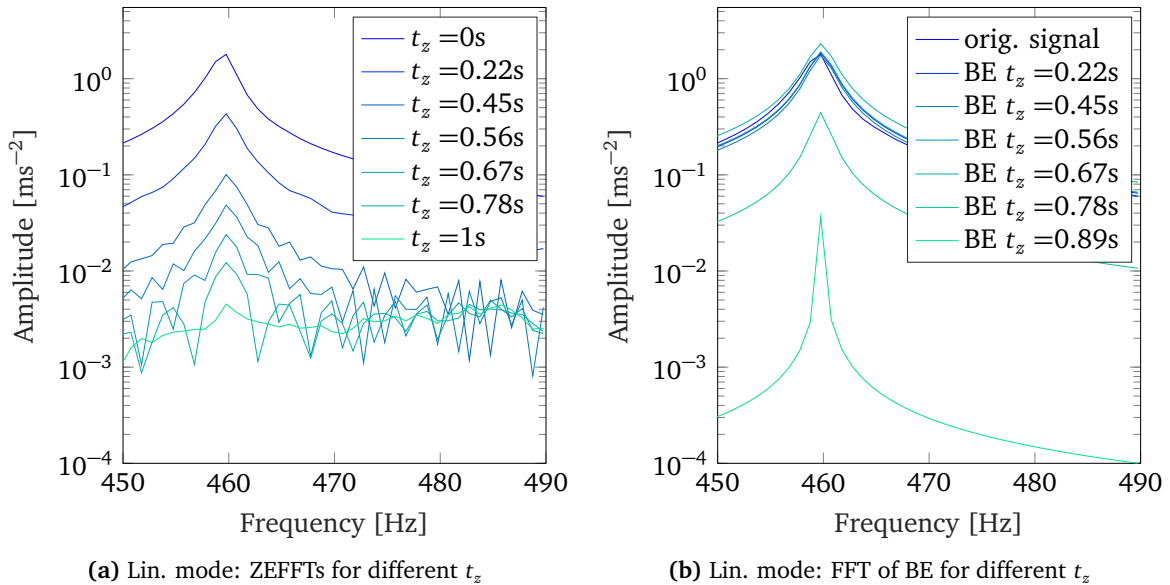


**Figure 4.45:** Results of modal ID and BE for non-linear mode

### 4.5.1 Sensitivity and Limitations

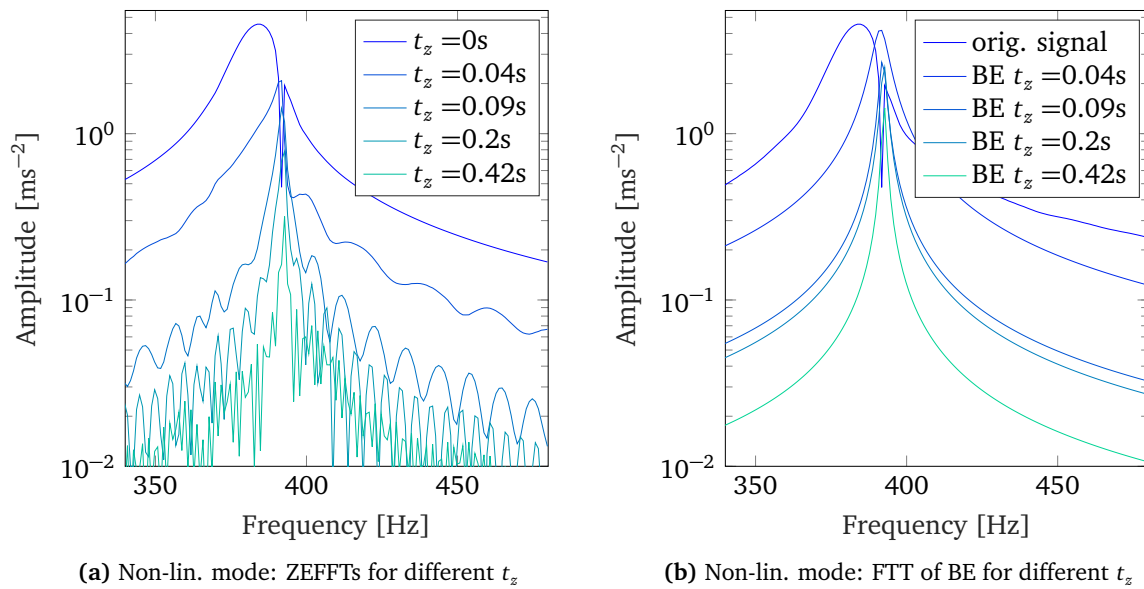
As already mentioned, the BE is very sensitive to the correctness of identified modal parameters. Regardless of the used modal ID tool, the modal parameters can only be estimated in a proper manner if the zeroing time  $t_z$  is depicted carefully. The modal ID will be inaccurate if  $t_z$  is too high and the signal is decayed as well as if  $t_z$  is selected too early and non-linearities are still present.

Figure 4.46b shows the effect of a late zeroing time. For a  $t_z$  higher than 0.67s the correct recreation of the signal is not possible anymore and a loss in amplitude for the BE signal can be detected. This however can be avoided by considering the ZEFFTs in Figure 4.46a before applying the BE and choosing  $t_z$  with a ZEFFT that is not too noisy. However, when considering the ZEFFTs it might appear that  $t_z = 0.67$ s seems to form a good basis for BE. But the BE signal for this zeroing time is slightly overestimated. This again shows the sensitivity of the entire process regarding the zeroing time. Therefore, it is to put effort in choosing the zeroing time and validate the selection.



**Figure 4.46:** Linear mode: sensitivity of the BE to zeroing time

The effect of choosing  $t_z$  too early is shown in Figure 4.47b. For  $t_z = 0.04$ s the non-linearities are still present in the signal. This leads to an overestimation of the BE signal since the non-linear effects are assumed to be part of the linear signal. This again can be avoided by taking a closer look to the ZEFFTs before determining the zeroing time. E.g., the absence of non-linearities is usually characterized by a constant eigenfrequency when increasing the zeroing time (peak does not shift to higher frequencies). In addition, the reconstructed signal has already lost amplitude for  $t_z = 0.4$ s. Meaning that the time window for a good reconstruction of the signal is small. In order to be sure that the zeroing time is well chosen and leads to a good BE signal, it is recommended to compare FFTs of BE signals in addition to the comparison of ZEFFTs. E.g., as can be seen in Figure 4.47b,  $t_z = 0.09$ s and  $t_z = 0.2$ s lead to a very similar BE signal, meaning that  $t_z \in [0.1 \text{ s}, 0.2 \text{ s}]$  might be a good choice.



**Figure 4.47:** Non-linear mode: sensitivity of the BE to zeroing time





## Chapter 5

### Conclusion and Outlook

To sum up, during this thesis, a linear and non-linear joint ID was applied to a beam-like structure. The linear approach FBS includes the isolation and parameterization of the joint and its coupling with separate measurements. The joint parameterization itself proved as reliable with consistent results for multiple repetitions. In contrast to that, the sensibility to a change of the torque level heavily depends on the observability of the parameterized value. The coupling process showed a high sensitivity toward the rotational values of  $K$ , whereas no sensitivity to increasing the translational values appears.

It was possible to compare the coupled results to the results of the HT. The comparison to HT as well as the comparison of the coupling results itself showed that the result of the coupling strongly depends on the correctness of the joint parameterization. Therefore, it is especially important to ensure that all joint parameters are observable with the chosen measurement setup.

However, the two main questions why the coupling process is not able to meet the reference and why the coupling results do not change when increasing the translational stiffness remain. For the problem of not matching the reference measurements, several reasons are hypothesized: first, the assumption of a rigid interface during the VPT might not be valid (especially due to the fact that the most flexibility appears on the modes being investigated, which activate the joint area). Furthermore, it was not possible to prove that the identified values for the stiffness are correct. On the contrary, it has been shown that a stiffness value not being observable can lead to an incorrect parameterization with serious consequences. In addition, the linearization of the problem causes inaccuracies that are unavoidable. When measuring the parts separately, the non-linear effect of the joint is not present. Hence, the dynamic behavior differs from the behavior in the assembled state. Besides that, attaching the bolt to one of the parts might cause a different mass distribution from the one in the assembled structure. Finally, the influence of the conditions of inverse substructuring cannot be neglected. The assumption that there is no cross coupling and that the joint is mass-less is not necessarily fulfilled. Of course, a mixture of some or all the reasons can appear.

For the fact that increasing the translational stiffness does not affect the coupling results, the two possible explanations are found: One explanation is that the stiffness identified is only a lower limit due to observability issues in the measured assembled dynamics (invalid decoupling). The second possibility is that the reconstruction is inaccurate based on the assumption of no cross coupling (invalid parameterization and re-construction).

It is to further investigate which of the options applies. A suggestion is to parameterize the entire joint instead of just its diagonal. Thus, the condition of no cross coupling is not necessary. However, the matrix  $\Gamma$  (Equation 3.4) can no longer be used for the LM-FBS coupling. Instead, a virtual mass can be added to the coupling as described in [10]. Alternatively, primal coupling can be conducted.

The coupling process with a parameterization of the entire joint could be sensitive to the changes in  $K$  and prove that the identified  $K$  is correct (assuming that the diagonal identified values coincide with the values identified in this thesis). If that is the case, then the inverse substructuring assumptions are not valid and the reconstruction with the diagonal joint fails. At the same time, it proves that the joint parameters can be isolated through the decoupling process.

In contrast, it may turn out, that the ID of the  $K$  is indeed only a lower border and the actual stiffness of the translational parts is higher. This means that the measurements fail in storing the right information and the decoupling approach cannot be applied. In this case, the inverse substructuring conditions do not apply to the entire FBS process.

Overall, the used structure is not appropriate for the application of FBS since the dynamic of the parts is dominating the stiffness. This thesis clearly showed the limitations of FBS and especially of inverse substructuring. In general, applying FBS to systems with much higher stiffness at the interface and at the same time very flexible parts is difficult. Checking the results regarding their correctness and accuracy became an important and necessary task. In the end, it was not possible to rely on the results of inverse substructuring and it is to put additional effort in the validation of the outcomes.

The goal to apply the FBS technique to zeroed and back-extrapolated data could not be implemented, since the bad passivity made a reliable modal ID impossible. Nevertheless, the foundation of the ZEFFT and BE was laid. It is now to develop an appropriate tool for the modal ID as well as for the determination of the zeroing time  $t_z$ . The following presents an idea for the implementation of the tool: The basis are the time signals for each input and output combination. It is to create a user interface that shows the ZEFFTs of a selected input and output combination. It is now to select a suited ZEFFT (or zeroing time  $t_z$ ) for each present mode in the regarded signal. Meaning that the selection of the zeroing time as well as the determination of the frequency ranges for the modal ID can be conducted at the same time. This is realized by selecting the ZEFFT through clicking on the peak (mode's eigenfrequency). For each mode, the modal analysis of the associated ZEFFT can be performed together with the BE. The total BE signal is formed from the different back-extrapolated single mode signals of the modes. This has to be repeated for each input and output combination. Alternatively, it is possible to conduct a modal analysis of all modes together and a mode superposition for the BE.

## Bibliography

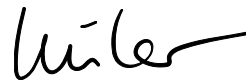
- [1] Allen, M. S. and Mayes, R. L. “Estimating the degree of nonlinearity in transient responses with zeroed early-time fast Fourier transforms”. In: *Mechanical Systems and Signal Processing* 24.7 (Oct. 2010), pp. 2049–2064. DOI: 10.1016/j.ymsp.2010.02.012.
- [2] Bograd, S., Reuss, P., Schmidt, A., Gaul, L., and Mayer, M. “Modeling the dynamics of mechanical joints”. In: *Mechanical Systems and Signal Processing* 25.8 (Nov. 2011), pp. 2801–2826. DOI: 10.1016/j.ymsp.2011.01.010.
- [3] Bregar, T., El Mahmoudi, A., Kodrič, M., Ocepek, D., Trainotti, F., Pogačar, M., Gödeli, M., Čepon, G., Boltežar, M., and Rixen, D. “pyFBS: A Python package for Frequency Based Substructuring”. In: *Journal of Open Source Software* 7 (Jan. 2022), p. 3399. DOI: 10.21105/joss.03399.
- [4] Chen, W., Jana, D., Singh, A., Jin, M., Cenedese, M., Kosova, G., Brake, M. R., Schwingshackl, C. W., Nagarajaiah, S., Moore, K. J., and Noël, J.-P. “Measurement and identification of the nonlinear dynamics of a jointed structure using full-field data, Part I: Measurement of nonlinear dynamics”. In: *Mechanical Systems and Signal Processing* 166 (Mar. 2022), p. 108401. DOI: 10.1016/j.ymsp.2021.108401.
- [5] Feldman, M. “Non-linear system vibration analysis using Hilbert transform–I. Free vibration analysis method 'Freevib'”. In: *Mechanical Systems and Signal Processing* 8.2 (Mar. 1994), pp. 119–127. DOI: 10.1006/mssp.1994.1011.
- [6] Goyder, H. “Reverse Filtering Decay Time Histories for Non-Linear Vibration Identification”. In: *TriboMechDynamics*. 2019.
- [7] Haeussler, M., Klaassen, S., and Rixen, D. “Experimental twelve degree of freedom rubber isolator models for use in substructuring assemblies”. In: *Journal of Sound and Vibration* 474 (May 2020), p. 115253. DOI: 10.1016/j.jsv.2020.115253.
- [8] Jin, M., Kosova, G., Cenedese, M., Chen, W., Singh, A., Jana, D., Brake, M. R., Schwingshackl, C. W., Nagarajaiah, S., Moore, K. J., and Noël, J.-P. “Measurement and identification of the nonlinear dynamics of a jointed structure using full-field data, Part II: Nonlinear system identification”. In: *Mechanical Systems and Signal Processing* 166 (Mar. 2022), p. 108402. DOI: 10.1016/j.ymsp.2021.108402.
- [9] Klerk, D. de, Rixen, D. J., and Voormeeren, S. N. “General Framework for Dynamic Substructuring: History, Review and Classification of Techniques”. In: *AIAA Journal* 46.5 (May 2008), pp. 1169–1181. DOI: 10.2514/1.33274.
- [10] Mahmoudi, A. E., Rixen, D. J., and Meyer, C. H. “Comparison of Different Approaches to Include Connection Elements into Frequency-Based Substructuring”. In: *Experimental Techniques* 44.4 (Mar. 2020), pp. 425–433. DOI: 10.1007/s40799-020-00360-1.
- [11] Meggitt, J. and Moorhouse, A. “In-situ sub-structure decoupling of resiliently coupled assemblies”. In: *Mechanical Systems and Signal Processing* 117 (Feb. 2019), pp. 723–737. DOI: 10.1016/j.ymsp.2018.07.045.

- [12] Pai, P. F. and Palazotto, A. N. “HHT-based nonlinear signal processing method for parametric and non-parametric identification of dynamical systems”. In: *International Journal of Mechanical Sciences* 50.12 (Dec. 2008), pp. 1619–1635. DOI: 10.1016/j.ijmecsci.2008.10.001.
- [13] Seijs, M. van der, Bosch, D. van den, Rixen, D., and Klerk, D. de. “An improved methodology for the virtual point transformation of measured frequency response functions in dynamic substructuring”. In: Institute of Structural Analysis and Antiseismic Research School of Civil Engineering National Technical University of Athens (NTUA) Greece, 2014. DOI: 10.7712/120113.4816.c1539.
- [14] Sracic, M. W., Allen, M. S., and Sumali, H. “Identifying the Modal Properties of Non-linear Structures Using Measured Free Response Time Histories from a Scanning Laser Doppler Vibrometer”. In: *Topics in Nonlinear Dynamics, Volume 3*. Springer New York, 2012, pp. 269–286. DOI: 10.1007/978-1-4614-2416-1\_22.
- [15] Sumali, H. and Kellogg, R. A. “Calculating Damping from Ring-Down Using Hilbert Transform and Curve Fitting”. In: 2011.
- [16] Tol, Ş. and Özgüven, H. N. “Dynamic characterization of bolted joints using FRF decoupling and optimization”. In: *Mechanical Systems and Signal Processing* 54-55 (Mar. 2015), pp. 124–138. DOI: 10.1016/j.ymssp.2014.08.005.
- [17] Trainotti, F., Klaassen, S., Bregar, t., and Rixen, D. “A Singular Value Based Filtering Strategy for Noise Reduction on Measured Response Data”. In: *Extended Abstract, IMAC 2022* (2022).
- [18] Van Der Seijs, M. “Experimental Dynamic Substructuring”. PhD thesis. 2016. DOI: 10.4233/UUID:28B31294-8D53-49EB-B108-284B63EDF670.

## Disclaimer

I hereby declare that this thesis is entirely the result of my own work except where otherwise indicated. I have only used the resources given in the list of references.

Garching, May 19, 2022

A handwritten signature in black ink, appearing to read 'W. L.', written above a horizontal line.

(Signature)